Check for updates

Recent advances of bifunctional catalysts for zinc air batteries with stability considerations: from selecting materials to reconstruction

Wanqi Tang,[ab] Jiarong Mai,[a] Lili Liu, [ID] *[a] Nengfei Yu, [ID] *[a] Lijun Fu, [ID] [a] Yuhui Chen, [ID] [a] Yankai Liu,[c] Yuping Wu [ID] *[acd] and Teunis van Ree[e]

With the growing depletion of traditional fossil energy resources and ongoing enhanced awareness of environmental protection, research on electrochemical energy storage techniques like zinc–air batteries is receiving close attention. A significant amount of work on bifunctional catalysts is devoted to improving OER and ORR reaction performance to pave the way for the commercialization of new batteries. Although most traditional energy storage systems perform very well, their durability in practical applications is receiving less attention, with issues such as carbon corrosion, reconstruction during the OER process, and degradation, which can seriously impact long-term use. To be able to design bifunctional materials in a bottom-up approach, a summary of different kinds of carbon materials and transition metal-based materials will be of assistance in selecting a suitable and highly active catalyst from the extensive existing non-precious materials database. Also, the modulation of current carbon materials, aimed at increasing defects and vacancies in carbon and electron distribution in metal–N–C is introduced to attain improved ORR performance of porous materials with fast mass and air transfer. Finally, the reconstruction of catalysts is introduced. The review concludes with comprehensive recommendations for obtaining high-performance and highly-durable catalysts.

Dr Yuping Wu, FRSC, Chair Professor of Southeast University. He got his PhD degree from Institute of Chemistry, CAS, in 1997. In 2003, he was promoted to full professor in Fudan University, China. In 2015 he moved to Nanjing Tech University and shifted to Southeast University in 2021. He has published over 430 papers in peer-reviewed journals with H-index > 96, was awarded the World's Most Influential Minds (2015) by Thomson Reuters, and Albert Nelson Marquis Lifetime Achievement Award (2019), and one of Highly Cited Researchers over the World. He undertook pioneering research work on cutting-edge aqueous batteries, and gel-type and nonporous separators for lithium batteries with high safety, lithium sulfur batteries of high energy density, and hybrid capacitors.

1. Introduction

The increasing frequency of energy shortages and the deleterious effects of carbon-based fuels, such as environmental pollution and related green-house effects are factors driving the acceleration in the development of secondary energy sources that are mobile, portable, with high-efficiency energy conversion and, most importantly, clean to produce and use. To realize the low-carbon goal and greatly decrease carbon dioxide emissions, cleaner energy sources must be developed. Solar and wind energy and a variety of storage systems such as fuel cells, batteries, and supercapacitors for electricity production and powering of electronic devices have become important issues recently.[1] The development of new and clean energy storage techniques is gaining momentum and drives policy-making; hence, highly efficient, safe, functional and easily-commercialized devices are needed to meet the demands of utilization and environmental protection.[2]

Li-ion batteries are increasingly getting involved in our life. In spite of great progress, there still is a great need for higher

[a]State Key Laboratory of Materials-oriented Chemical Engineering, Institute of Advanced Materials (IAM), School of Energy Science and Engineering, Nanjing Tech University, Nanjing 211816, P. R. China. E-mail: liulili@njtech.edu.cn; yunf@njtech.edu.cn; wuyp@fudan.edu.cn

[b]College of Chemical Engineering, Nanjing Tech University, Nanjing 210009, China

[c]Hunan Bolt Power New Energy Co., Ltd, Dianjiangjun Industrial Park, Louxing District, Loudi 417000, Hunan, China

[d]School of Energy and Environment, Southeast University, Nanjing 210096, China

[e]Department of Chemistry, University of Venda, Thohoyandou 0950, South Africa

energy and power density since in some working situations the lithium-ion battery cannot satisfy this need. While some researchers are cautious about the future of this technology, metal–air batteries are growing in importance as possible next-generation devices answering demands for higher performance.[3] For example, long-distance traveling of electric vehicles up to 700 km may be hard to achieve with traditional batteries.[4] Zinc (Zn), magnesium (Mg), and aluminium (Al)–air batteries are receiving increasing attention, exhibiting safe, low cost and abundant materials. Besides these, Li–air batteries (LABs) show the highest theoretical energy density, rivalling the gasoline engine (13 000 W h kg^{-1}), but incomplete cycling and safety issues are hindering wide usage.[4,5] Therefore, zinc–air batteries are an appropriate choice for both achieving capacity and safety (compared to, *e.g.*, Na).[6] In the following paragraphs, articles published recently focusing on the catalyst for zinc–air batteries will be discussed.

Unlike metal-ion batteries and supercapacitors, secondary metal–air batteries involve two reversible reactions on the air cathode surface, *viz.* the oxygen evolution reaction (OER) and oxygen reduction reaction (ORR), corresponding to the charge and discharge processes, respectively. The developing voltage gap between catalyst and metal has the potential to meet the demands for both high current density and stable discharge voltage.[7] However, this technology usually is associated with problems with dendrite formation and efficiency loss in the electrolyte, especially in the alkaline electrolyte, hindering the long-term use of metal–air batteries.[3,8]

Secondary metal–air batteries are highly sensitive to the concentrations of reactants and rate of electron transfer, which on a macroscopic scale correspond to current density and stability. The reaction rate is limited by the concentrations of the reactants and the electron transfer rate. During operation, the low transfer rate and the unstable electrode–electrolyte interfaces limit long-term use, which should be considered when balancing the requirements for real working conditions.[9] Therefore, for commercial application of metal–air batteries, research is not only aimed at improving catalyst ability but also focusing on synthesis of new electrode materials that support long-term electrode stability with morphology control or other techniques.[10,11]

Among the applications of metal–air batteries, the user-friendly zinc–air battery (ZAB) system is attractive as a substitute for Li-ion-based batteries. Zinc–air batteries and Li–air batteries are regarded as promising and viable energy systems with advanced technology that will improve upon the existing engineering process and theoretical performance limits of Li batteries.[12] A typical ZAB usually consists of a zinc anode, electrolyte, separator, and bifunctional air cathode. During charging and discharging, cycling between Zn-ion and Zn metal, the Zn metal interacts with the electrolyte.[13] Zn–air batteries can also be characterized as all-solid or aqueous according to the electrolyte phase. The OER and ORR reactions at the air electrode match the generation and consumption of O_2 mainly from the oxygen dissolved in the electrolyte and outside air (in theory). For the ORR reaction during discharge, atmospheric O_2 diffuses through the air cathode, which usually

consists of three compressed layers (gas diffusion layer, current collector, and electrocatalyst), simultaneously accepting electrons from the cathode to form hydroxide ions in an alkaline enviroment.[14] In the OER process, Zn is deposited from the electrolyte, while the air cathode generates O_2 bubbles. This causes a mechanical breakdown of the catalyst by the airflow and massive corrosion of carbon or catalyst when the charging voltage reaches ~2.0 V. Some researchers separate the OER and ORR reactions by adding two different catalysts that work when charging and discharging, respectively.

As three-phase reactions, the OER and ORR reactions are strongly catalyzed by state-of-the-art precious metals such as Pd, Pt, Ir, or Au from the point of view of activity and durability. High prices and lack of resources are regarded as barriers to the large-scale application of noble metals.[15] Although remarkably, 95% of fuel cells are applying Pt as an efficient catalyst,[16] transition metals still have the potential for substituting the noble metals. In recent years, more and more researchers have attempted to improve the properties of catalysts based on transition metals such as Ni, Co, Fe, and Mn exhibiting bifunctional catalytic ability for the OER and ORR reactions. Carbon-based materials like graphene and N-doped carbon nanotubes (CNTs) and non-metal-doped oxides such as spinel and perovskites have been introduced to improve the performance of ZABs. Many metal-based materials deposited on highly conductive nanosheets like MXenes,[17] porphyrin-based metal–organic frameworks,[18] and MOF/PCP-based materials,[19] like non-thermal plasma,[20] are also used to modify the performance of ZABs.[21]

Many reviews have focused on mechanism analysis and new ZAB systems to give advice on how to rationally select catalysts.[22] Some are proposing new techniques of catalyst optimization for better electrochemical performance, like interfacial engineering[23] and advanced architecture design.[24] In this discussion we categorize modification into three types: (1) higher conductivity (like carbon materials), (2) catalytic ability (lower
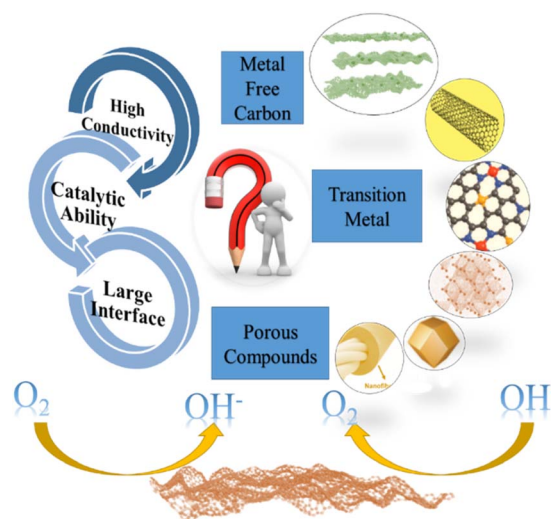

Fig. 1 Schematic illustration of key processes catalyzed by bifunctional materials.

adsorption energy with hetero-doping), and (3) larger reactive area (structure and geometrical optimization). The attempts made to meet the goals of achieving a high-performance cell with longer stability, are shown schematically in Fig. 1.
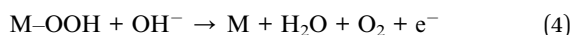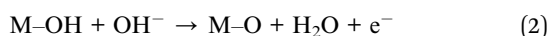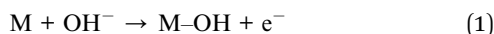
2. OER and ORR reactions on air cathode of ZABs

The zinc–air battery was first studied in 1878, and a few years later a gas diffusion electrode with a porous carbon layer on a nickel current collector was investigated, also called the Walker Wilkins battery.[25] Currently, some commercialized zinc–air cells can be found in many systems like remote communications, seismic telemetry, and navigator signalling.

But this primary battery cannot be used on a large scale because it cannot be recharged. Zinc–air batteries have been studied intensively from 1975 to 2000, and as Li-ion battery technology matured, many international companies, such as EOS, Fluid Energy, and ZincNyx have joined the field with excellent research work.[25] However, even though the commercial foundation of ZABs has been laid at the lab level – showing potential for extended use and good performance in applications where Li-ion batteries are less useful – their commercial use is still hampered by the limited performance at high current density and over the long term. Therefore, researchers are focusing on extended aqueous/flexible/combined ZABs with high performance and safer configuration than Li-based batteries, as more and more demand arises for advanced wearable electronics and super-thin devices.

The metal redox reaction takes place at the zinc foil, which is an excellent metal source just below Li in terms of power density per mass, and should support the capacity of the battery and sustain the voltage for a long time. However, because zinc suffers from many problems,[26–29] the low efficiency of this metal electrode limits its use. As a result, electrolytes, separators, and also cell configurations are studied to remove these barriers. In this review, we focus on the air electrode, which provides a possible interface for the OER and ORR reactions.
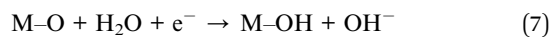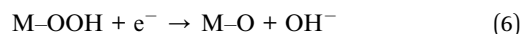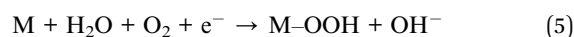
The oxygen evolution reaction presumably contributes to water electrolysis and has been studied by many researchers seeking to unravel the complicated pathways and mechanisms of water electrolysis. In a typical alkaline electrolyte, the intermediates playing important roles in these mechanisms arise as follows:

$$M + OH^- \rightarrow M\text{–}OH + e^- \tag{1}$$

$$M\text{–}OH + OH^- \rightarrow M\text{–}O + H_2O + e^- \tag{2}$$

$$M\text{–}O + OH^- \rightarrow M\text{–}OOH + e^- \tag{3}$$

$$M\text{–}OOH + OH^- \rightarrow M + H_2O + O_2 + e^- \tag{4}$$

M–OH, M–O, and M–OOH represent the intermediates formed at the active site for reaction, and M–O corresponds to the reactive metal–O bonds. While these single-electron half-reactions take place during oxygen evolution, the interface is

unstable due to two mechanisms – lattice oxidation mechanism (LOM), where lattice oxygen participates in the reaction, and adsorbate evolution mechanism (AEM), where the lattice oxygen is not involved. By deeply studying these two mechanisms, the degrading mechanisms of different catalysts for the OER are now better understood. Also, the stability of ZABs using metal as a catalyst is strongly influenced by the OER performance in an alkaline or flexible battery. Hence, the development of efficient and robust OER catalysts is urgently needed to meet the demand for rechargeable ZABs.[30]

For the reverse mechanism, two major reaction pathways are widely accepted. One is a direct four-step single-electron pathway producing hydroxide, representing a highly efficient way for reduction of O_2 in ZABs; while the other is an indirect two-electron pathway that produces peroxide. Over recent years several active sites have been proposed by some researchers when highly conductive carbon or N-doped carbon-based materials are introduced;[31] however, most intermediate half-reactions can be represented as follows:

$$M + H_2O + O_2 + e^- \rightarrow M\text{–}OOH + OH^- \tag{5}$$

$$M\text{–}OOH + e^- \rightarrow M\text{–}O + OH^- \tag{6}$$

$$M\text{–}O + H_2O + e^- \rightarrow M\text{–}OH + OH^- \tag{7}$$

$$M\text{–}OH + e^- \rightarrow M + OH^- \tag{8}$$

As formulated, oxygen is absorbed by the metal in the presence of water, and one electron contributes to formation of M–OOH while another electron is transferred to form M–O. After this transfer, M–O gains an electron and a proton to form M–OH, and a final electron transfer reduces this product back to the initial M with formation of a hydroxide ion.[32] In this half-reaction series, the rates of generation and transformation of the intermediates play a vital role in the reaction kinetics. To obtain high reaction rates and capacity, the binding energy between surface-active sites and intermediates should be optimized.

For the OER reaction, Ru, RuO_2, Ir, and IrO_2 are known as benchmark catalysts for the long-term oxygen evolution process in alkaline or acidic electrolyte.[33] The corrosion resistance during reaction leads to higher stability than that of other metal-based oxides.[34] More and more research is dedicated to highly-stable resources in both catalytic performance and crystal structure to unravel the mechanism of the OER reaction on precious metals.[35–38]

For the discharge process, which is an ORR reaction on an air cathode, Pt is considered to be the material that best balances activity and stability, and is regarded as the ideal material for a 4-electron transfer reaction. This precious metal is usually mixed with carbon, exhibiting high ORR performance in both acidic and alkaline electrolytes.[39]

To estimate more objectively the ORR performance at laboratory level, a rotating disk electrode (RDE) with a three-electrode system is normally used, removing diffusion influence to some extent.[40] As the ORR process is actually co-affected

by surface reactions and mass transfer, the half-wave potential ($E_{1/2}$) – the potential needed to reach half of the limiting current density, obtained from the LSV curve – is a widely accepted indicator (although it may not be comprehensive) for evaluating this ORR performance, which may differ little as diffusion ability changes.[41,42]

Recently, due to high electrolysis demands, as in PEMFCs, the Pt/C electrode has been modified to increase the operation time by avoiding carbon corrosion, Pt dissolution, active site leaching, Ostwald ripening, and agglomeration of nano-particles.[43] Alloys, nanostructured material, and loading on other carbon-based materials are approaches used to enhance the coordination process and stabilize the crystal structure for the ORR reaction.

Before considering the substitution of these precious metals with more abundant metals and carbonaceous materials to find suitable catalytic materials, it is crucial to understand the mechanism of the ORR process. Numerous early reports have mentioned that the first electron transfer steps are the rate-determining steps (RDS) for the ORR, which means the O_2 adsorption process is the limiting process. However, recently it has been pointed out that the intermediate steps are regarded as RDS processes, which means that the adsorption and desorption of M–O, M–OH, and M–OOH determine the reaction rate. Norskov *et al.* introduced a method to calculate the free energy of all intermediates using density functional theory (DFT) calculations, based on the potential of the electrode to determine the adsorption energy. The results show that electron transfer is impossible when oxygen is adsorbed strongly on the Pt(111) face,[44,45] but by lowering the activation energy needed, the reaction would proceed. Volcano plots were used to calculate the adsorption energy for removal of O and OH species, showing that Pt and Pd provide the best potential for effective catalytic performance.

D-band theory was also introduced by Nørskov for further understanding of the intermediates and reaction rate. The adsorption energy of ORR intermediates on the active site of the catalyst directly affects the reaction activity. Nørskov *et al.* used DFT to study the adsorption energy of oxygen intermediates at an early stage. There exists a unique scaling relationship between the free energies of the oxygen intermediates. Briefly, the d-band theory enables comparison of the oxygen–metal bond on one transition metal surface, and the strength of coupling of 2p states of oxygen and d states of metal. Therefore, a fast reaction should result in an upward shift of the catalyst's Fermi level of the strength or energy of bonds, leading to less filling, and a suitable bond can be formed. For a precious metal such as Pt, the Fermi level can also be modulated by alloying, surface modulation, and varying the structure of the catalyst.[46,47]

As the active site of metal cations influences the multi-valence characteristics of the working performance of transition metals, the modification of a bifunctional catalyst for the previous two reactions is mostly based on optimization of the geometry and structure for (1) more active reaction sites (reaction rate), (2) doping, tailoring crystal structure and metal-bonds for higher catalytic performance (better onset potential), and (3) combination and added carbon base for higher conductivity (more electron transfer). Carbon-based materials and transition metals-based materials are common catalysts widely used in energy storage devices.

However, the evaluation of a catalyst is based on its electrochemical performance, which is influenced by primary modifications like doping and surface decoration. As the OER and ORR reactions are interfacial reactions that may change crystal structure with the higher voltage and high-alkaline environment in ZABs, rational catalyst design and selection should also consider reconstruction of functional interfaces with highly stable structures. Studies on materials and the reconstruction process help build an understanding of the relationship between stability and performance.

3. Metal-free carbon material

Before being applied in ZABs, carbon materials with their high conductivity have long been considered as highly active support or base for many materials.[48,49] Over the last two decades, most carbon materials have been modulated and applied to fuel cells after treatment avoiding their hydrophilicity, but they are seldom used in alkaline electrolysis or zinc–air batteries, because of their extensive corrosion during the OER reaction[32,50]

Due to the stability problems of the OER reaction experienced with precious metals like Pt and Pd, carbon materials such as CNTs and graphene are considered rational substitutes and ideal ORR reaction catalysts with low extraction and processing costs.[51,52] High-dispersion structures with large active areas and fast reactant transfer channels enlarge the interface for higher activity, while simultaneously the low resistance facilitates electron transfer. Heteroatom doping of carbon materials has been widely recognized as an efficient method that can significantly improve ORR activity compared to pristine carbon materials.[53–55]

More recently, the preparation of metal-free materials has concentrated on the synthesis methodology for achieving highly strained regions in sp^2 networks; functional and activated nanostructures (O atoms for example); heteroatom doping (N, B alternating electron and active sites); and active sites at defects, vacancy pentagons/heptagons, and edges.[54,56] In this section, we concentrate on the origin of 4-electron transfer in metal-free materials, and their high stability in ZABs.

3.1 N-doped graphenes and CNTs

By modification of carbon nanomaterials using various innovative strategies, including surface functionalization,[57–59] geometric structuring,[60–62] and heteroatom doping,[63–65] the OER and ORR reactions can be improved by rational heteroatom doping with B, N, Si, P, and S. N-doped carbonaceous materials are widely used in zinc–air batteries without any added metal.[66,67] However, the performance of N-doped graphene[68] and N-doped CNTs is strongly affected by their source and processing.

In a typical graphene synthesis process, as shown in Fig. 2a, melamine and L-cysteine are mixed in a mass ratio of 4 : 1 to form a homogeneous precursor that is heated at 600 °C to form
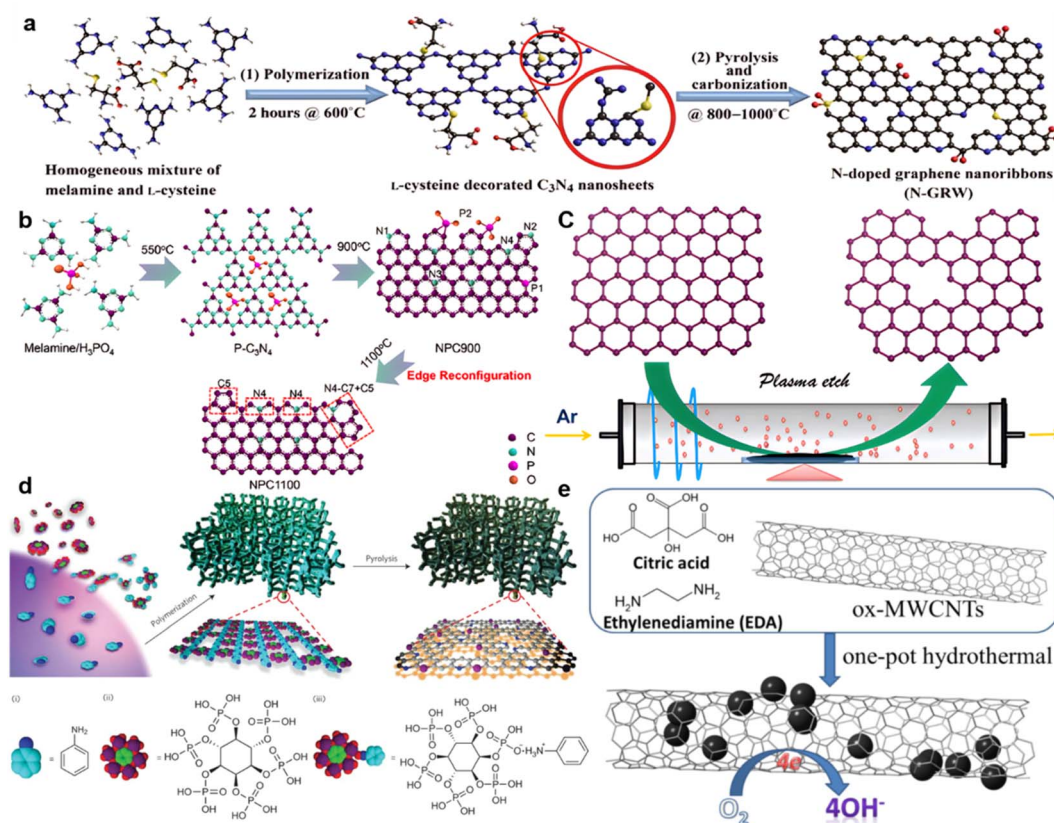
Fig. 2 Graphenes and CNTs doped by N. Configuration refinement assisted by (a) S and N, (reproduced from ref. 69 with permission from AAAS, CC BY-NC) (b) P, (reproduced from ref. 73 with permission from Nature) (c) Ar plasma, (reproduced from ref. 74 with permission from the Royal Society of Chemistry). (d) PANi, (reproduced from ref. 78 with permission Copyright ©2015, Nature) and (e) CQDs. (Reproduced from ref. 95 with permission Copyright © 2019 Elsevier).

C_3N_4 nanosheets doped with L-cysteine. Then, carbonization and pyrolysis at 800–1000 °C transform the previously formed nanosheets into a 3D interconnected carbon network, with the –C–S–C– bond playing an important role during carbonization. The result is an N-doped graphene named N-GRW that has good OER and ORR characteristics, with a half-wave potential of 0.84 V (vs. RHE) and 0.92 V (vs. RHE) onset potential, and 360 mV overpotential for the OER process. RRDE measurements confirmed a low yield (below 5%) of H_2O_2 and a high electron transfer number reaching 3.95. This high performance is ascribed to the graphitic N and pyridinic N in the graphene.[69] The Mott–Schottky effect accelerates electron transfer on the catalyst, which is either p-type or n-type. As shown by X-ray absorption near edge structure (XANES) spectroscopy of researched intermediates, the quaternary N with n-type doping, rather than the p-type doping by pyridinic N, is responsible for the ORR. Furthermore, the fast adsorption of OOH* and O* intermediates on carbon atoms next to the pyridinic N is responsible for the OER reaction (Fig. 2a). As discussed above, from another angle, doping quaternary N atoms in graphene provides electrons to the π-conjugated system (n-type doping), leading to increased nucleophile strength for the adjacent carbon rings C^{d-} to enhance O_2 adsorption (because O_2 has high densities of O lone pair electrons O^{d+}), and hence accelerating the ORR.[70,71]

Also, the defects and edges in the graphene are regarded as active sites for OER and ORR reactions.[72] Edge-rich graphene usually exhibits high ORR reactivity. Zigzags in the graphene exhibit different performances before and after N doping. The edge effect also can be enhanced by P doping by the reconfiguration effect, when N_4 bonds can be oriented by heating P–C bonds. Consequently, electron transfer numbers over the same potential range are improved from 3.48–3.57 for samples treated at 900 °C, to 3.75–3.94 for samples reconstituted at 1100 °C.[73] As shown in Fig. 2b, S and P doping in the precursor (mostly not found in the final product) can also enhance the coupling effect at the edges and inside the graphene structure. After treatment at 1100 °C (the high temperature removing S and P), the final carbon materials are rich in holes and edges on the graphene structure at S and P vacancies. With an Ar plasma (Fig. 2c), the graphite oxide formed by thermal expansion has a voluminous, fluffy structure and the few-layer carbon nanotubes and graphite obtained were also enhanced with more edges, despite the absence of dopants.[74] As a result, in 0.1 M KOH, the plasma-treated edge-rich material (P-G) exhibited a potential of 0.912 V (vs. RHE), which is more positive than that of pristine G (0.806 V), with an electron-transfer number of 3.85.

Polymers are widely used as precursors for N-doped materials.[75,76] Unlike most of the other synthetic polymers,

conducting polymers possess robust conjugated structures that are excellent candidates to produce carbon-based materials, due to their ample carbonization and architecture-maintaining capacity.[77] As shown in Fig. 2d, a N,P-doped carbon foam with a large surface area of ~1663 m^2 g^{-1} that was formed after treatment at 1000 °C of a PANi hydrogel co-doped with nitrogen and phosphorus, exhibited a positive onset potential of 0.94 V *versus* the reversible hydrogen electrode (RHE) and a half-wave potential of 0.85 V *versus* RHE in 0.1 M KOH.[78] Precursors like PANI-PPy nanofiber,[79] PANI with MWCNTs,[80] CMP on a SiO$_2$ template,[81] crosslinked fluoropolymers,[82] and rationally controlled asymmetric sidechain conjugated polymers,[83] combined with fast processing such as polymer dehalogenation,[84] exemplify synthesis processes for high-active-area carbon materials.[85]

Besides graphene materials, carbon nanotubes are also a suitable form of carbon with good electron transfer and channels for quick mass transfer.[86] Similarly, high nitrogen doping content modifies the charge distribution in the carbon rings, leading to increased C 1s binding energy and inhibition of carbon corrosion during the OER. Thus, N-doped CNTs should exhibit efficient OER and ORR reactions.[87] The advantages of this material include improved mass transfer of reagents/products, enhanced electronic conductivity, and higher resistance to corrosion.[30,88]

Several reviews have described the characteristics of active sites obtained by new strategies and N doping on CNTs and graphene nanoribbons (GNRs), and also other materials like carbon nanofibers,[89] carbon nanoribbons derived from MWCNTs,[79,90] and N-doped hybrids.[72,91] Some new methods have been introduced that link the N doping effects on carbon
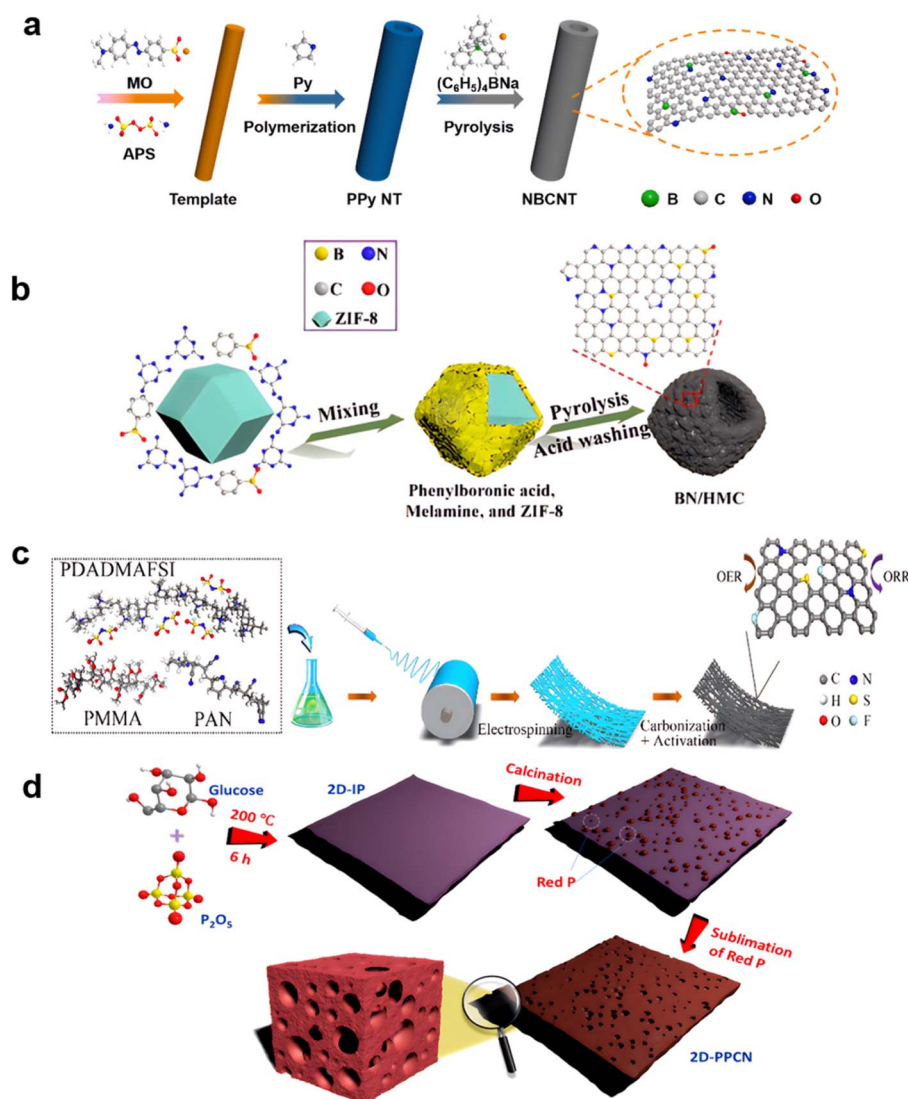
Fig. 3 Methods for introducing S and P into carbon materials: (a) (C$_6$H$_5$)$_4$NB on polymers, (reproduced from ref. 100 with permission. Copyright © 2021 Elsevier) (b) NaBH$_4$ on ZIF-8, (reproduced from ref. 102 with permission. Copyright © 2021, American Chemical Society) (c) electrospun with PDADMAFSI, (reproduced from ref. 105 with permission. Copyright © 2021 Elsevier) (d) red P. (reproduced from ref. 107 with permission. Copyright © 2018, American Chemical Society).

materials. Several fluorescent carbonaceous nanomaterials such as graphene quantum dots (GQDs), polymer dots (PDs), and nanodiamond QDs have been reported.[92–94] Nitrogen-doped CQDs (N-doped CQDs)[95] have been introduced to enhance the ORR activity, as shown in Fig. 2e, and highly N-doped CQDs are located on ox-MWCNTs, similar to N,P co-doped CQDs, with electron transfer numbers reaching 3.8, proving a highly catalytically active surface. Synthesis of COF/COP/MOF precursors,[96] carbon materials derived from ionic liquid precursors, and solvothermal/hydrothermal synthesis has contributed to a better understanding of carbon materials.[97]

3.2 Heterodoping of N-doped carbon materials

Doping of carbon materials is not limited to N-doping to enhance ORR reactions; B, P, and S are regarded as ideal heteroatoms to improve the N-doping effects for achieving higher yielding ORR reactions.[98] The ORR and OER activities of CNTs can be boosted considerably by an effective oxygen-induced surface electron density modulation strategy.[99]

For co-doping with N and B,[100] the introduction of boron by adding a boron source before or during pyrolysis of the carbon material is generally done, as shown in Fig. 3a. Introducing oxidation or reduction processes on pretreated carbon material to form stable bonds, is also commonly done. For example, after the oxidation of graphene with $H_2SO_4/KMnO_4$ and reduction with $NH_3–BH_3$, the graphene edge sites contained more heteroatomic dopants, and the catalyst ORR activity was enhanced. However, harsh oxidation also increased the number of permanent defects in the catalyst, reducing the number of electron pathways.[101] Using the zeolitic imidazolate framework (ZIF) ZIF-8 as a template for $NaBH_4$ reduction, the boron is introduced into a box-like carbon structure, as shown in Fig. 3b.[102] Apart from traditional pyrolysis, a CVD process could also be introduced in this process, with B located on the graphene[103] or CNTs[104] to obtain optimized three-coordinate structures. These exhibit sp^2-like hybridization to form B–C bonds, contributing to the higher electronegativity of carbon with respect to boron.

More complicated doping with three or more non-metal elements doped on carbon nanofibers was used to functionalize good bifunctional materials in zinc–air or lithium–air batteries.[105,106] As shown in Fig. 3c, N, F, and S co-doped nanosheets have been produced by electro-spinning polyacrylonitrile (PAN)/polymerized ionic liquid (PIL) nanofibers, resulting in a positive half-wave potential (0.91 V) for the ORR and a low overpotential (380 mV at 10 mA cm^{-2}). N, F, and S tri-doping also improved electrochemical properties, especially the OER reaction.[105] When phosphorus was added before calcination, large-sized two-dimensional phosphorus-doped carbon nanosheets (2D-PPCN) with tunable porosity were synthesized by combining P_2O_5 with a common saccharide as a template. The efficient production resulted in a 20–35 nm-thick 2D morphology, considerable heteroatom P doping, and excellent tunable porosity. 2D-PPCN-2/6 had a half-wave potential ($E_{1/2}$) of 0.85 V and an overpotential of 365 mV after iR correction,[107] at a current density of 10 mA cm^{-2} (Fig. 3d).

3.3 Synthesis of porous carbon materials

The evaporation method generated 3D highly porous heteroatom-doped ultrathin carbon nanosheet networks during pyrolysis. Based on the low evaporation temperature of Zn, the precursor of ZIF-8 obtained by solid grinding and water mixing exhibited two kinds of porous structures that are widely used in carbon materials.[108] Also, as shown in Fig. 4a, N-doped ultrathin carbon nanosheets with ultrahigh specific surface area (1793 m^2 g^{-1}) were obtained by carbonizing a uniform mixture of citric acid and NH_4Cl at 1000 °C. This product was rich in inside edge defects and exhibited low overpotential and robust stability for the ORR, OER, and HER.[109] Hard-template-like silicon bases are used to generate hollow structures.[110,111]

As shown in Fig. 4b, mesoporous silica nanospheres were formed by self-assembly of silicate oligomers obtained by hydrolysis of TEOS and CTAB micelles, because the hydrolysis and condensation rate of TEOS was faster than the polymerization rate of 3-aminophenol/formaldehyde in the presence of ammonia. As a result, N-doped carbon nanocages (N-CCs) with a porous self-supported architecture and high specific surface area were synthesized.[112]

Electrospinning and hydrogels[113] are also improved techniques for designing porous structures from precursors, starting with highly dispersed nanocarbon fibers, unlike synthesis

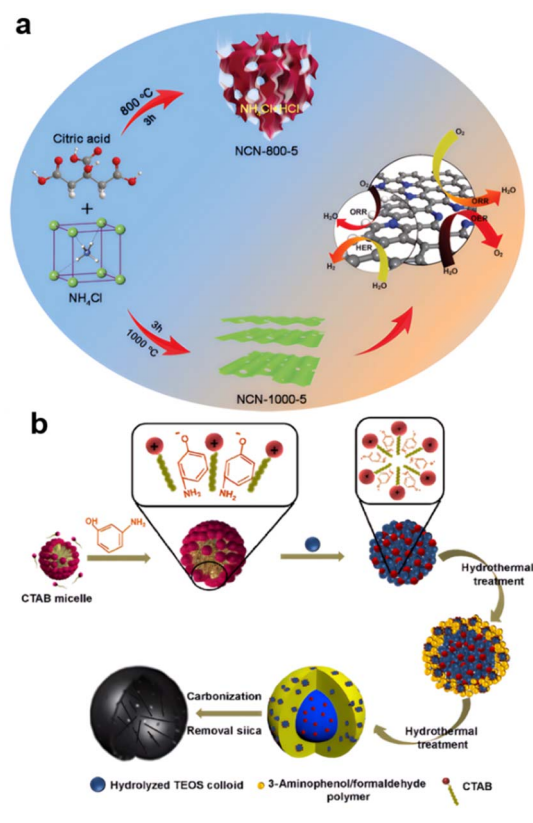Fig. 4 Templates and evaporation method generating porous (a) NH_4Cl (reproduced from ref. 109 with permission. Copyright © 2021 Elsevier) (b) silicon and CTAB assisted (reproduced from ref. 112 with permission. Copyright © 2020, Nature).
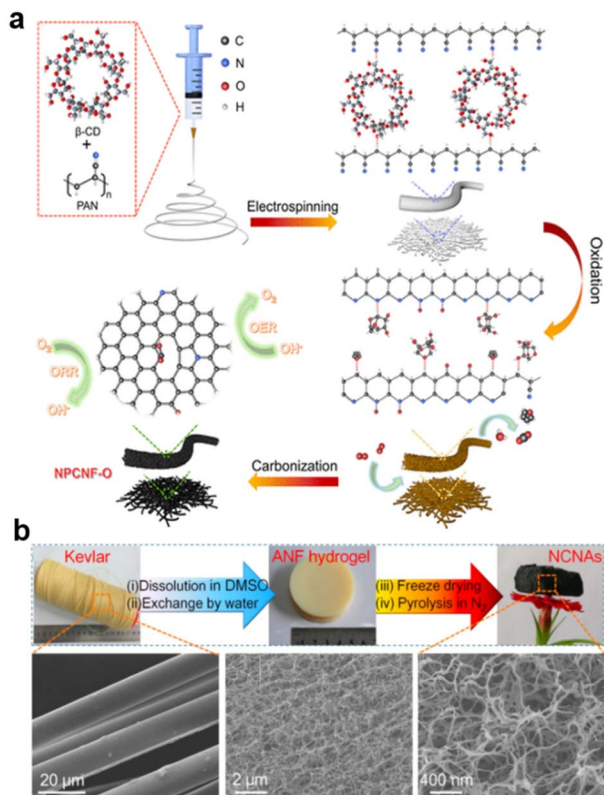
Fig. 5 Obtaining highly porous carbon materials by (a) Electrospinning (reproduced from ref. 91 with permission. Copyright © 2022, American Chemical Society) and (b) hydrogel (reproduced from ref. 119 with permission. Copyright © 2018 Elsevier).

from hard templates. Electrospun nanomaterials with outstanding chemical stability and structural diversity are promising electrocatalysts for the ORR[114–116] As shown in Fig. 5a, inside NPCNF-O, β-cyclodextrin acts as a pore inducer and oxygen regulator. Benefitting from the large specific surface area and synergistic effect of N, O co-doping, the NPCNF-O catalyst exhibits superior ORR ($E_{1/2}$ = 0.85 V $vs.$ reversible hydrogen electrode (RHE)) and OER ($E_{j=10}$ = 1.556 V $vs.$ RHE) activities with excellent stability.[91]

Besides being used as electrolyte,[117,118] nanofiber aerogels derived from commercial aramid have been prepared using a facile and cost-effective process based on solvent exchange followed by freeze-drying and pyrolysis under a N_2 atmosphere. Derived from porous aramid nanofiber (ANF) hydrogel, as illustrated in Fig. 5b, the as-prepared catalyst exhibits high electrocatalytic activity in the oxygen reduction reaction with a half-wave potential estimated to be 0.91 V ($vs.$ RHE) in 0.1 M KOH.[119]

3.4 Stability of carbon materials

Carbonaceous materials play an important role in zinc–air batteries; however, the effects of conductive carbon materials on the cycling stability of ZABs are usually overlooked.[120]

As shown in Table 1, metal-free carbon materials exhibit similar stability in the alkaline electrolyte at least at 10 mA cm^{-2}

for the ORR reaction, which is close to that of benchmark materials like Pt/C for ORR and Ir/C for the OER process. Most doped carbon materials are known to have long-term stability in the ORR reaction, but there is insufficient data for the OER process. Results differ case-by-case, due to the high-potential carbon corrosion in a highly alkaline environment while charging and discharging at a stable current density or voltage step.

The carbon corrosion in both alkaline and acid electrolytes provides a high barrier for application in water electrolysis,[121] PEMFCs,[122] and zinc–air batteries. The equilibrium potential of carbon is 0.207 V $vs.$ the reversible hydrogen electrode (RHE), making it thermodynamically unstable at potentials higher than the required 1.23 V $vs.$ RHE necessary for the oxygen evolution reaction (OER).[123] Real-time monitoring of electrochemical carbon corrosion in alkaline media has been recorded, as shown in Fig. 6a and b.[124] An obvious peak proving the relationship between charging-oxidation and CO generation can be observed.[125] Oxidative attack of ORR intermediates, demethylation, protonation/neutralization, and micropore flooding are the most commonly observed degradation mechanisms.[126]

We display the results for some metal-free carbon materials in Table 1. The stability measured of the rotating-disk electrode (RDE) in a weakly alkaline solution may not imply the same stability in a highly corrosive environment in ZABs. Interestingly, carbon materials with a higher intrinsic OER activity show lower durability and this has been tentatively attributed to the formation of active (*e.g.*, radical) OER intermediates, leading to chemical degradation of carbon materials.[122,127]

As shown in Table 1, several authors have studied the ORR stability by means of chronopotentiometry. The accelerated durability test (ADT) recorded the linear scan voltammetry (LSV) change over up to 30 hours or 10 000 cycles, finding up to 10% long-term degradation of the ORR reaction. This is still far away from cycling for 300 hours, of which 150 hours are discharging, not to mention the OER process. N,P-doped carbon materials, enabling high performance in the OER reaction, and also increasing OER stability, are ideal for long durability. Nitrogen atoms in the carbon materials are redistributed after the reaction.[149] To be more specific, highly graphitized platelet-type carbon nanofibers (pCNFs) are tolerant to electrochemical corrosion under oxygen evolution reaction (OER) conditions in a concentrated KOH electrolyte.[150] More reports reveal the use of metals to improve OER performance, for example using nickel nanoparticles on rGO[151] or Ni$_x$B coating to decrease the corrosion during OER testing in an alkaline environment.[152] This may be attributed to the transition metal working as reaction active sites.

4. Transition metal-based materials

Besides the precious metal and carbon materials with good OER and ORR performance, mentioned in the preceding paragraphs, transition metals have shown higher stability than other materials.[153] Many recent publications have described the lower corrosiveness leading to enhanced conductivity and high

Table 1   OER and ORR stability measurement in alkaline electrolyte of metal–free carbon materials

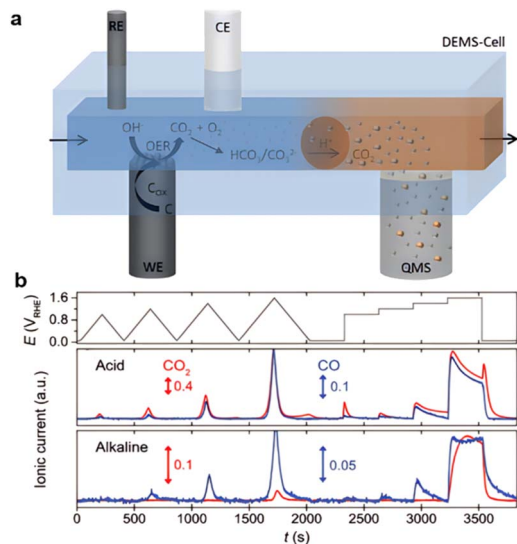| Catalyst	Electrode	Electrolyte	OER stability			ORR stability			Ref.
			Time	Potential drop	Potential (or current density)	Time	Potential drop	Potential (or current density)	
N-GRW	900 rpm	1 M KOH	24 h	9%	360 mV	12 h	10%	@0.7 V	69
ZnS/C-1100		0.1 M KOH				10 h	5.5%	@0.789 V	128
NCNAS	1600 rpm					12 h	10%		119
N,P–HCNF-8	900 rpm	0.1 M KOH				20 h	9%	@0.7 V	129
NPCNF-O	1600 rpm	0.1 M KOH		Slight change			Slight change		91
DAPHPNC-1020		0.1 M KOH	24 h	10.9%		24 h	14.9%		130
NPCNSS-1000						7500 s	17.6%	@0.8 V (vs. RHE)	131
MESO/MICRO-POPD	1600 rpm	0.1 M KOH				10 000 cycle	10 mV (half-wave)	10 mV s^{-1}	132
NOC-1000-1		0.1 M KOH				24 h	13.37%	@0.5 V	133
N-GDY-900		1 M KOH	5000 cycle	9%	100 mV s^{-1}				134
D/G-HASP			10 h	0.1% (overpotential)	10 mA cm^{-2}	10 000 cycle	17 mV (half-wave)		135
PEMAC@CNTS-90		1 M KOH				30 000 s	7%	5 mA cm^{-2}	136
ZG-NC-1000		0.1 M KOH				30 000 s	7.7%	@0.7 V	137
NFS-CNF-0.5-1000	1600 rpm	0.1 M KOH	30000 s	23%	@1.6 V (vs. RHE)	60 000 s	8%	@0.5 V (vs. RHE)	105
NPSC-DNA-2	1600 rpm	1 M KOH				10 h	15%		138
NBCNT-10	1600 rpm	0.1 M KOH				12 h	7.4%	@0.2 V (vs. RHE)	100
N-S-G-2		0.1 M KOH				10 000 cycle	9 mV (half-wave)	ADT (0.6–1.0 V vs. RHE, 100 mV s^{-1})	100
CNDA900	400 rpm	0.1 M KOH				4 h	12.06%	@0.40 V (vs. RHE)	139
CNT@NSCF	400 rpm	0.1 M KOH	2000 cycles	Small drop	OER LSV	20 000 s	5.65%		140
BP-100		0.1 M KOH				20 000 s	9.7%	@−0.25 V	141
A-N,S-G		1 M KOH	10 h	Steady	@10 mA cm^{-2}				142
CNS		0.1 M KOH				15 000 s	~14%		143
BNF-LCFS		0.1 KOH	2000 cycle	3 mV	@10 mA cm^{-2}	40 000 s	15%	@0.665 V (vs. RHE)	144
GNP-900	1600 rpm	1 M KOH	5000 cycle	13 mV	@10 mA cm^{-2}	5000 cycle	15.4 mV (half-wave)		106
PCN-CFP		0.1 M KOH	30 h	6.6%	@1.63 V	30 h	2.2%	@0.40 V	145
G-C$_3$N$_4$NS–CNT		0.1 M KOH	10 h	13.3%	@1.54 V				146
NGM		0.1 M KOH				8 h	1.5%	@0.60 V	59
NCF	1600 rpm	0.1 M KOH				24 h	11.1%	@0.7 V	147
HPC(MV-C-PN)		0.1 M KOH				10 h	No drop		148

Fig. 6 Observation of high corrosion of carbon during oxidization: (a) DEDMs system, (reproduced from ref. 124 with permission. Copyright © 2020 Wiley-VCH) (b) ionic peak of CO. (Reproduced from ref. 125 with permission from the Royal Society of Chemistry).

stability attained by rational modification of transition-metal-based materials used in aqueous alkaline electrolytes. The bi-functional oxygen reaction rates compare favorably to those of the precious metal benchmark catalysts, and the transition metal-based materials are therefore often the first choice as functional zinc–air electrode materials to substitute precious metals. Most of the reported catalysts are metal oxides, but other compounds such as nitrides and sulfides have also been shown to exhibit bi-functional activity.[154]

4.1 Transition metal oxides

The performance of transition metal oxides in the OER in the alkaline electrolyte is usually excellent and stable, promising better long-term use than carbon-based materials; however, the ORR performance of transition-metal-based materials is not as good as that of noble metals like Pt/C. The ORR reaction mechanisms on the metal oxides are different. The surface cations of transition metal oxides coordinate with the oxygen of H_2O and at the same time, the hydrogen atoms of H_2O are distributed on the catalyst surface. The protonation of surface oxygen ligands is charge-compensated by the reduction of metal cations such as Mn^{4+}, Co^{3+}, and Fe^{3+}. The M–OH intermediates also react further in end-on and side-on reactions.[42] The transition metal oxides apparently are also involved in strong metal-to-oxygen covalent interactions, established by the overlapping of the π-orbitals of O_2 and d_{z-2} orbitals of the transition metal.[155] In 2011, the Shao-Horn group calculated the volcano activities of the ORR caused by moderate e_g sigma-orbital filling with intermediate-strength bonding.[156] Surface lattice oxygen was oxidized while the oxygen adsorbate was reduced, highlighting the crucial role of functional transition metal redox in ORR as described by Mueller et al.[157]

Thus, multivalent transition metals like Ni, Co, Fe, and Mn are regarded as the metals of choice for higher OER and ORR activity. Commercialization efforts concentrate on the improvement of transition metal oxides, especially of the manganese oxides (MnO_2, Mn_2O_3, Mn_3O_4, etc.) that are known to be amongst the most investigated and utilized single metal oxide oxygen catalysts due to their affordability and environmental benignity.[158] The higher oxidation state of Mn leads to a favorable OER reaction rate, but due to the decreased activity in the ORR and lower 4-electron transfer rate, the manganese oxides do not perform as well as the noble metals.[159]

Hence, for application in zinc–air batteries, the improvement of MnO_2 starts with improving the ORR activity. Crystal structure modifications introducing more oxygen vacancies, with no foreign additives, were introduced into manganese oxide crystals by simple heat treatment under an air and Ar atmosphere, with Mn_3O_4 and MnOOH forming the lattice. Forming oxygen-nonstoichiometric oxides by heating at 350–400 °C for about two hours increased the electron transfer number from 3.5 to 3.7 and improved the stability. The formation energy of OOH* on β-MnO_2 (110) decreased from 3.09 eV to 0.96 and 0.55 eV by introducing one or two O_{2c} vacancies, respectively (Fig. 7a).[160] Secondly, it is also necessary to increase the conductivity. By linking the Mn to NCNTs, the MnO_2–NCNT had 220 mV overpotential in 0.1 M KOH for the OER process and higher electron transfer ability, with lower ohmic loss compared to MnO_2 and almost 50% lower catalyst resistance.[161] Similarly, materials combining metal and carbon like the MnO_2–NCNT linked material obtained by the synproportionation of manganese(II) nitrate with potassium permanganate (s-MnO_x/$MWCNT_{ox}$) or from the incipient moisture impregnated manganese(II) nitrate (i-MnO_x/$MWCNT_{ox}$) perform better in the OER. Modifications that partially achieve higher oxidation states like Mn^{4+} without changing the reductive carbon base enhance the catalyst's performance in the OER reaction.[162]

More active sites can also be obtained by morphology control of MnO_2. As shown in Fig. 7b, nanocrystals and nanoplatelets of
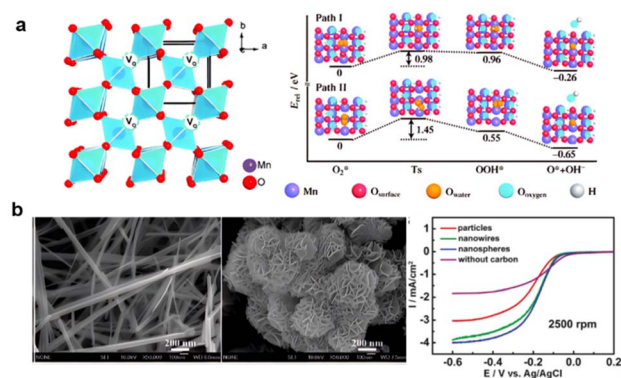

Fig. 7 (a) Oxygen induced MnO_2 (reproduced from ref. 160 with permission. Copyright © 2013 Wiley-VCH) (b) morphology control of MnO_2 and ORR performance (reproduced rom ref. 163 with permission. Copyright © 2010, American Chemical Society).

α-MnO$_2$ can increase the electron transfer number to 3.8, which is only 3.6 for other nanoparticles. To further increase conductivity for O$_2$ adsorption, HO$_2^-$ chemical-transforming on active sites and ionic and electron transport, MnO$_2$-NWs@Ni-NPs are also recommended.[163,164] More complicated methods such as N–C doping in polymer-derived Mn–Fe–N–C SACs further increase Mn-based material activities,[165] while CeO$_2$ could help stabilize Mn valency.[166,167] Notably, MnO$_2$ is one of the few materials that can be employed in various fields of EESSs: alkaline batteries, supercapacitors, aqueous rechargeable lithium-ion batteries, and metal–air batteries. Yet, the technology still entails bottlenecks and is not yet ready for commercialization.[168]

Similarly, modifications of other oxide catalysts like MnO$_2$ are categorized by the crystal structure and the original phase. Strategies to enhance the electrocatalytic performance of manganese oxides include doping with cations, coating with metals, and integrating conductive nanostructures.[92,159,169–171]

4.1.1 Spinels. Single-metal oxides consist of only one metal, and are relatively easier to obtain, but doping with more metals into the crystal lattice could enhance the activity of these oxides. As mentioned before, the transfer of intermediates is regarded as a limitation, as the ORR reaction rate is not as good as that with N-doped materials in ZABs. The modulation of metal oxides deals mainly with the optimization of the reaction rate of intermediate transformations (adsorption, transforming, desorption) by rational change of the chemical state in oxides.

Spinels and perovskites are typical structures of transition metal materials with highly stable and active edge and active site structures. Spinel oxides with a typical formula of AB$_2$O$_4$ (A = Li, Mn, Zn, Cd, Co, Cu, Ni, Mg, Fe, Ca, Ge, Ba, *etc.*; B = Al, Cr, Mn, Fe, Co, Ni, Ga, In, Mo, *etc.*) have attracted much interest for application in electrocatalysis and other energy-related processes.[172] In an AB$_2$O$_4$ spinel, A occupies the tetrahedral centers, whereas B occupies the octahedrally coordinated centers, which can be described as A$_{Td}$(B$_2$)$_{Oh}$O$_4$ with the two sites influencing the catalytic performance *via* different mechanisms.

Cations at octahedral and tetrahedral sites in spinel oxides are believed to have different functions toward oxygen electrocatalysis. For example, when a tetrahedral Co in Co$_3$O$_4$ was replaced by Zn, the resulting ZnCo$_2$O$_4$ had OER activity similar to that of Co$_3$O$_4$.[154,173] Besides increasing activity from CoAl$_2$O$_4$ to ZnCo$_2$O$_4$ to Co$_3$O$_4$, heating the CoAl$_2$O$_4$ increased the Co octahedral occupancy, resulting in better OER performance. On the other hand, the tetrahedral cations do not contribute significantly to the OER, based on the e$_g$ orbital theory.[174] As shown in Fig. 8a and b, Xu's and Shao-Horn's groups consolidated the role of electron orbital filling in metal oxide catalysis, and by analyzing Mn$_x$Co$_{3-x}$O$_4$ (x = 2, 2.5, 3), Li$_x$Mn$_2$O$_4$ (x = 0.7, 1), XCo$_2$O$_4$ (X = Co, Ni, Zn), and XFe$_2$O$_4$ (X = Mn, Co, Ni), found that the e$_g$ occupancy of the octahedral cation site plays an important role in metal oxide catalysis, where a descriptor study on the ORR/OER of spinel oxides was presented by the volcano
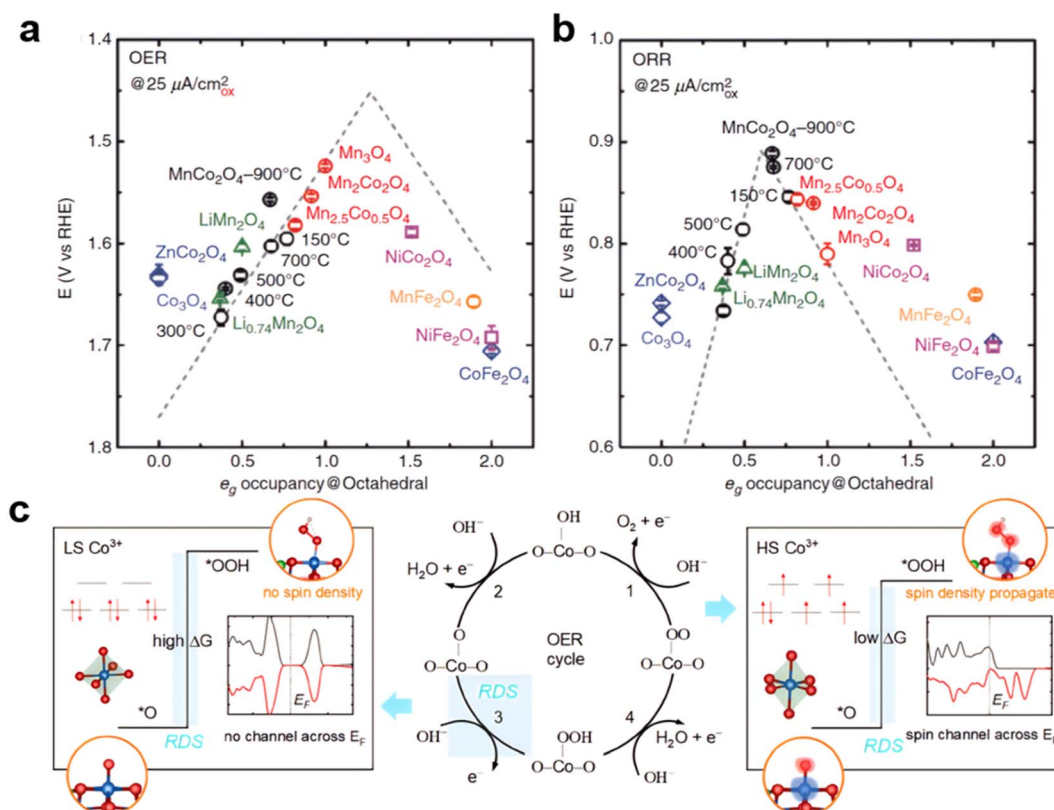

Fig. 8 (a) and (b) Volcano relationship between e$_g$ filling and OER/ORR performance. (reproduced from ref. 175 with permission. Copyright © 2017 Wiley-VCH). (c) High and low spin of Co and OER RDS. (Reproduced from ref. 178 with permission. Copyright © 2021 Wiley-VCH).

shape e_g filling. The volcano profiles result from the e_g electron-governed rate-limiting steps and binding strength of reaction intermediates.[175] The edge-sharing $[Mn–O_6]$ and $[Co–O_6]$ octahedra in the spinel lattice allow the Mn–O–Co super exchange interaction *via* the edge oxygen, and thus the e_g occupancy of active Mn can be regulated by varying the Mn/Co ratio[176] or Mn/Fe ratio.[177] Besides cation doping, the spin states of the Co sites also play an important role in the OER reaction. In spinel zinc–cobalt oxide (not considered as a superior catalyst for the electrochemical oxygen evolution reaction), in the $t_{2g}^6 e_g^0$ configuration, the existence of low-spin (LS) state cobalt cations hinders the OER activity and gives rise to a purely localized electronic structure, exhibiting poor binding affinity for the key reaction intermediate and lowering the OER activity. High-spin (HS) state cobalt cations in thermally controlled spinel $ZnCo_2O_4$ have been found to propagate a spin channel that promotes spin-selected charge transport across the Fermi level during the OER (not working for Co_3O_4) and generates more favorable orbitals for the adsorption of intermediates *OOH[178] (Fig. 8c).

Thus, for a potentially bifunctional material, cation doping, anion doping, and introducing vacancies are typical ways to influence the crystal structure, which increases the intrinsic activity of the metal lattice in the spinels.[7,179] In recent years, spinel catalysts have also been created using new approaches such as solid-, solution-,and vapor-phase methods.[180]

Cation doping is a widely used method for improving the performance of spinels. In addition to single-metal oxides, the rational substitution of a functional metal could efficiently change the physical property of spinels and the activity at interfaces.

In this regard, the incorporation of Ni,[82,181,182] Zn,[183,184] and Mn[185] in cobalt-based spinel oxides has been demonstrated to boost the ORR and OER performance. Wu *et al.* substituted half of the $[Co^{3+}]_{Oh}$ in Co_3O_4 by Fe^{3+}, which turned the normal spinel into an inverse spinel structure. The coexistence of Co^{3+} and Fe^{3+} in the crystal led to a dissimilarity effect and polarization of octahedral cations, which regulates the adsorption energy of oxygen species and the bond length of adsorbed O_2, resulting in superior ORR activity.[186] A three-dimensional ordered mesoporous Co_3O_4 decorated with Mg has been synthesized using PS beads as a hard template and the synthesized $Mg_xCo_{3-x}O_4$ (3DOM $Mg_xCo_{3-x}O_4$) displayed a great improvement of the ORR. Substituting Mg^{2+} in the tetrahedral sites led to more Co^{3+} occupying octahedral sites and a considerable decrease in the energy level of the d band center (ε_d).[187]

Instead of bimetal doping, ternary doping of the functional cations in $Co_{0.5}Ni_{0.5}Mn_2O_4$ is also possible.[188] The metal can also be changed by a magnetic field. For example, $FeCo_2O_4$ nanofiber was annealed in a magnetic field of 2500 Oe, producing a right-shifted half-wave potential of 20 mV for the ORR and a left-shifted overpotential of 60 mV at 10 mV cm^{-2} for the OER as compared with its non-treated counterpart. Calculations showed that the improvement is caused by the shift close to the Fermi level of the d-band centers (ε_d) of Co-3d and Fe-3d in the tetrahedral and octahedral sites of the $FeCo_2O_4$-M nanofibers.[189]

Anion doping is also a useful strategy to improve the electrocatalytic activity of metal oxides, and the substitution of O by N, P, S, and Se has been investigated a great deal. Anion doping can lead to increased electronic conductivity.[190,191] Derived from a Co-PBA derived Co_3O_4 nanobox, treated with Na_2S at 120 °C for 36 hours, the Co_3O_4/CoS microbox heterostructure, as shown in Fig. 9a, exhibited a great increase in stability with 98.9% retention of current density after 50 hours CA measurement at 0.4 V in 0.1 M KOH and improved ORR performance with electron transfer number rising from 3.37 to 3.99 as a result of S doping. At the same time, the OER performance of these materials is also increased as evidenced by EIS spectra recorded at a constant potential of 1.65 V (*vs.* RHE) by a decrease in charge transfer resistance from 290.4 (Co_3O_4) ohms to 30.8 ohms (Co_3O_4/CoS).[192] The P–O group in a P-doped Co_3O_4 has been studied using an on-chip micro-device. The coupled P–O groups effectively promote the metal–oxygen covalence of newly-formed oxides, accelerating electron transfer between the active metallic center and oxygen adsorbates, thus leading to enhanced electrocatalytic activity.[193] On MnO_2 nanorods, coating Mn^{2+} and Co^{2+} by TA treatment produced $MnS_2O_x/MnCo_2S_4$. The low OER activity of MnO_2 was greatly increased, getting closer to the fast-charging needs of the zinc–air battery.[194] (Fig. 9b).

Increasing the vacancies in spinels with good ORR activity such as Co_3O_4 tends to improve the OER.[195,196] New methods that are widely used are plasma treatment with multi-function: surface atom doping or reconstructing, introducing vacancies or defects, partially reducing or oxidizing surfaces, and increasing the porosity or roughness.[197] It has been shown that vacancies can be generated by heating in a vacuum. As shown in Fig. 9c, the vacuum-calcination strategy was utilized to convert $Co(OH)_2$ into oxygen-defective amorphous-crystalline CoO (namely ODAC-CoO) nanosheets with dramatically enhanced ORR and OER electrocatalytic activities.[198] This method can be widely used in LDH-derived materials for high porosity and more vacancies. For low and high states of transition metals, Wang *et al.* used quasi-operando X-ray photoelectron spectroscopy (XPS) and operando X-ray absorption fine structure (XAFS) on the Co_3O_4 for the OER reaction to confirm that with ample vacancies, the Co^{2+} to Co^{3+} process could pre-oxidize the metal to generate Co–OOH· sites for the OER, facilitating the deprotonation process at a lower potential.[199] Also, the crystal can be further enhanced by Ar plasma doping and P doping. OER performance was improved in 1 M KOH with higher Co^{3+} content, showing better ability than direct Ar-plasma treated Co_3O_4, obtaining more vacancies and higher conductivity, suggesting that the favored catalytic ability of P-Co_3O_4 is dominated by the Co^{2+} (T_d) site. (Fig. 9d).[200]

Besides the influence on the crystal, morphology control also has a great influence on mass transport and accessibility of active sites. As the metal oxides have a low number of active sites exposed to electrolytes, gas, and ions, the performance, especially the ORR performance is sensitive to the morphology. As a simple example, different morphologies of $NiCo_2O_4$ were compared and synthesized with a SiO_2 template, a P-123
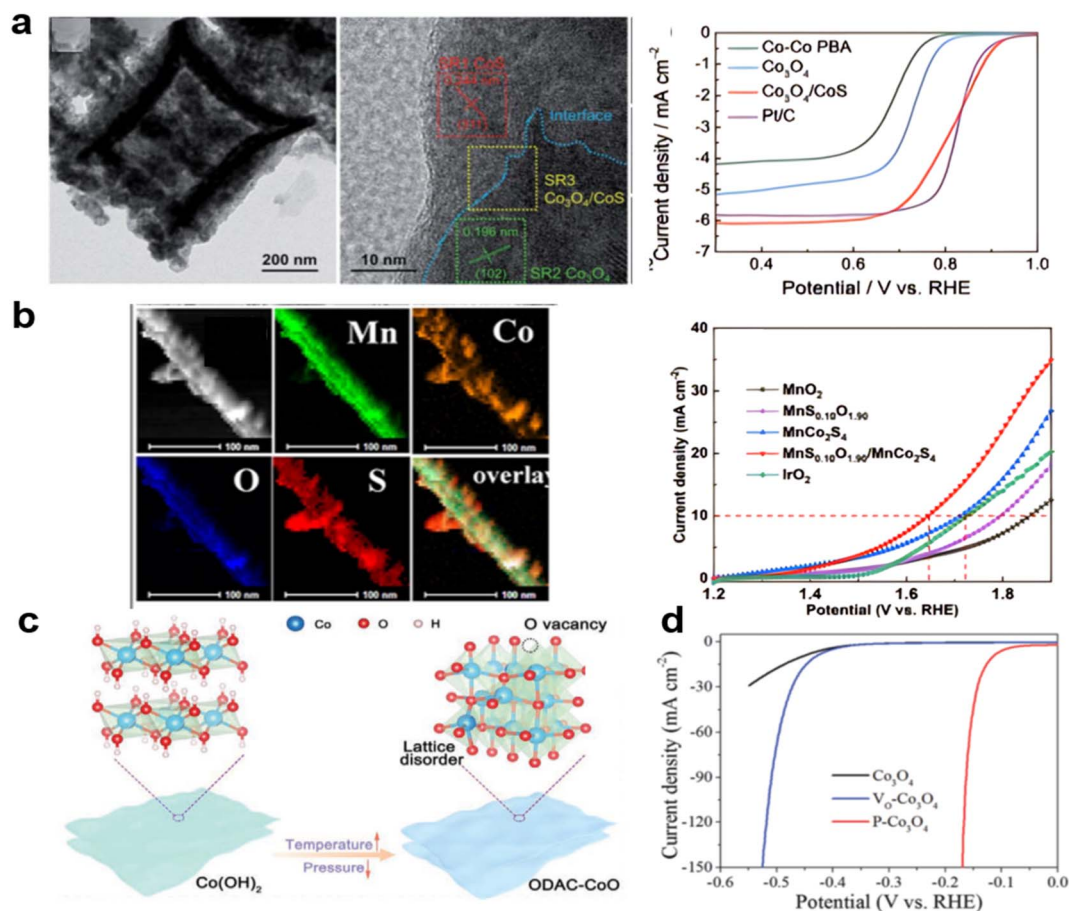
Fig. 9 Heterodoped spinels for high performance: (a) S on Co_3O_4 derived from PBA, (reproduced from ref. 192 with permission from the Royal Society of Chemistry) (b) S on $MnCo_2O_4$ needles, (reproduced from ref. 194 with permission. Copyright © 2021 Elsevier) (c) O vacancies introduced by vacuum heating, (reproduced from ref. 198 with permission. Copyright ©2021 Wiley-VCH) (d) P by plasma treatment (reproduced from ref. 200 with permission from the Royal Society of Chemistry).
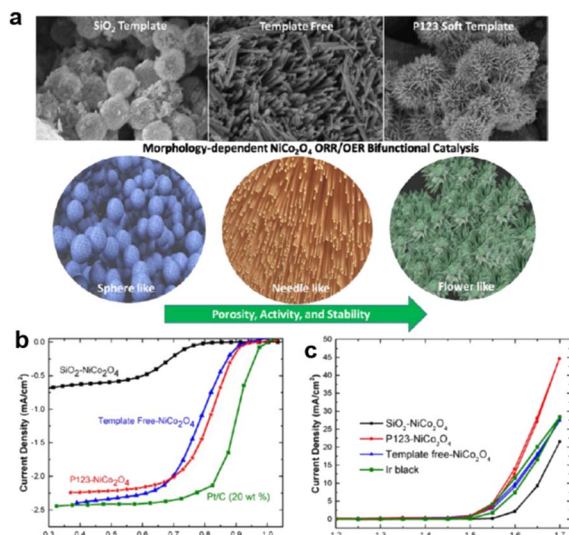

Fig. 10 (a) Morphology and (b) OER and (c) ORR performance of $NiCo_2O_4$ formed by SiO_2 templated, P123 templated, and template free synthesis.[201] (Reproduced from ref. 201 with permission. Copyright © 2017, American Chemical Society).

template, and template-free. The Co and Ni valences here exhibited widely different values.[201]

As shown in Fig. 10, the different added non-carbon catalysts for the ORR reaction produced different morphologies, with the P-123-derived sample exhibiting a unique nanoneedle structure significantly affecting both OER and ORR.[201]

A Fe-containing MOF, $Fe_4(Fe(CN)_6)_3$ (Prussian Blue, PB) cubes-derived material used to form the porous hollow spinel AFe_2O_4 (A = Zn, Ni, Co) has been proposed as a good precursor for spinels as energy storage material. Using the self-sacrificial template strategy described in the article, high energy-conversion active materials can be obtained without influencing the box structure.[202] Similarly, doping with hierarchical hollow nanoplates (NPs) composed of ultrathin Co_3O_4 nanosheets doped with 13 different metal atoms, using a Lewis acid etching and metal species coordination process, has been reported. As shown in Fig. 11a, the nitrates of the foreign metals are adsorbed on the previous ZIF configuration and together transformed to a spinel in the calcination process.[203] The weakly acidic solution can result in a gentler etching process, cation exchange, before subsequent thermal oxidation processes similar to tannic acid (TA)[204] or controlled solutions. Also, on

a self-supported system on carbon cloth, as shown in Fig. 11b, a N-confined Co_3O_4 can be synthesized with nanorod morphology, with N doping and special box structures derived from ZIF-67.[205]

In 2016, the Cui group used the Prussian Blue analogue $Mn_3[Co(CN)_6]_2 \cdot nH_2O$ and gelatin-coated Ketjen black decomposed at 400 °C to form nitrogen-doped carbon material and porous spinel oxides as template (Fig. 11c). The resulting cell displayed the stability of these MOF-derived oxides and the importance of higher transfer ability[206] in 6 M KOH rather than 0.1 M KOH with 10 times lower transferability at ambient O_2 concentrations in 6 M KOH rather than 0.1 M KOH where the environment RDE test is usually done.[207]

4.1.2 Perovskites. Similar to spinel, functional perovskites show low conductivity and low ORR performance; however, their stability and OER reaction rate in alkaline media are very good.[156] Due to the structural flexibility of perovskites, most

research has concentrated on the crystal lattice catalytic properties. Surface vacancies play a vital role in the ORR reaction. Moreover, side-on and end-on oxygen vacancies can also be introduced in the reduction process by bidentate adsorption, as shown by earlier studies of $LaNiO_3$ (ref. 208) where the O–O bond is elongated when oxygen interacts with the oxygen vacancy site and the B-site element.[160] The perovskite $Ba_{0.5}Sr_{0.5}Co_{0.8}Fe_{0.2}O_{3-d}$ (BSCF5582) showed that oxygen vacancies indeed participate in the ORR reaction by increasing the electron transfer number and reducing the formation of peroxide species.[209,210]

High reduction performance has been achieved using some new methods. By surface reduction with 5% Li, the $La_{0.6}Sr_{0.4}Co_{0.2}Fe_{0.8}O_{3-\delta}$ (LSCF) ORR performance was greatly enhanced, with the half-wave potential increasing from 0.62 V for pristine material to 0.72 V versus RHE. The conductivity of the lithium-reduced LSCF nanopowders increased greatly, with the electron
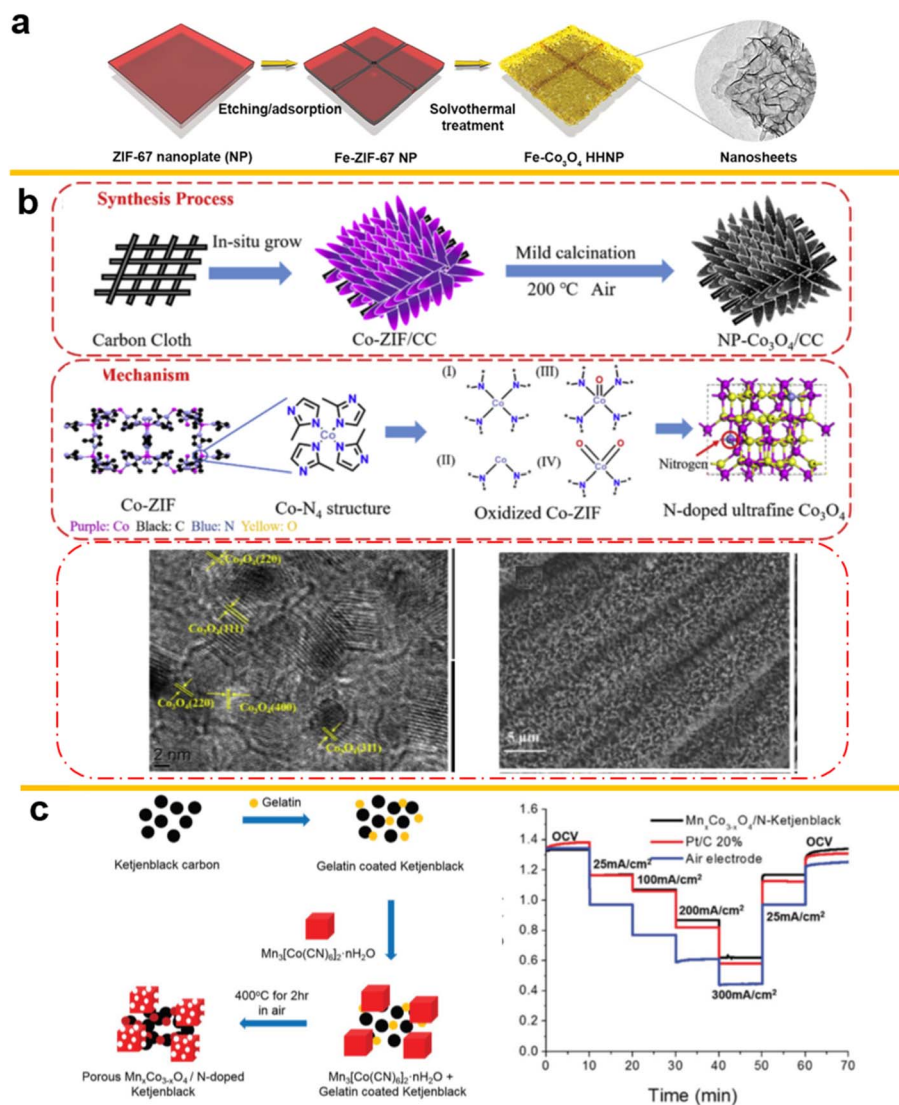

Fig. 11 (a) Metal on Co_3O_4 derived from ZIF-67, (reproduced from ref. 203 with permission Copyright © 2020 from Songlin Zhang et al., published by Wiley) (b) N-doped Co_3O_4 on Carbon Cloth, (reproduced from ref. 205 with permission Copyright © 2020 Elsevier) (c) $Mn_xCo_{3-x}O_4$ derived from Prussian blue with high stability in ZABs. (Reproduced from ref. 206 with permission. Copyright © 2016 Wiley-VCH.)
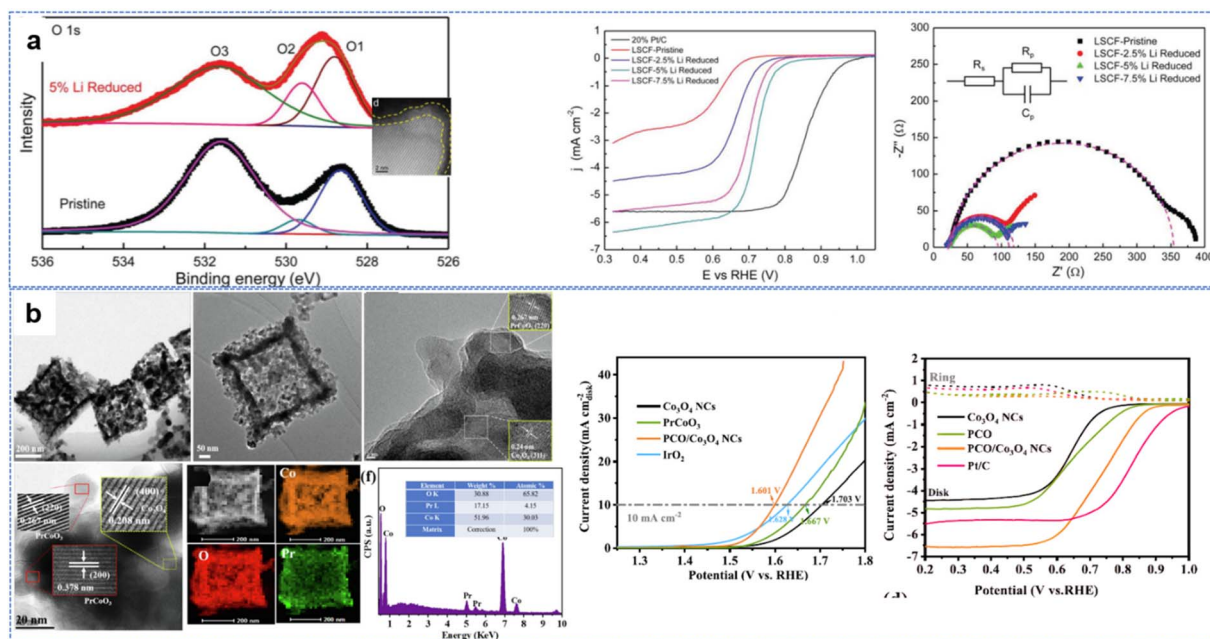
Fig. 12 Perovskites used for OER and ORR reactions: (a) Li reduced LSCF, (reproduced from ref. 211 with permission Copyright © 2018 Wiley-VCH) (b) P doped PCO/Co_3O_4 heterojunction from ZIF-67. (Reproduced from ref. 214 with permission Copyright © 2022 Elsevier).

transfer number increasing from 3.71 with the pristine material to 3.91. Improved oxygen vacancies at the surface play an important role in OER and ORR reactions (Fig. 12a).[211] Potassium-substituted $LaMnO_3$, in an alkaline environment, performs excellently, with improved kinetics and activity of the ORR (half-wave potential of 0.78 V), OER (potential at the current density of 10 mA cm^{-2} is 1.66 V) and battery performance (no visible sign of degradation even after 1000 charge–discharge cycles).[212]

The yolk–shell structure of the perovskite $LaCo_{1-x}Fe_xO_3$ showing improved ORR performance and possessing an amorphous CoOOH layer during the reaction has proved the vital role of the new interface for reaction sites.[213] As shown in Fig. 12b, when composite perovskite/spinel heterojunction $PrCoO_3$/Co_3O_4 nanocages obtained by Pr^{3+} adsorption on ZIF-67 boxes were calcined in air, edge-sharing interfaces (where activities are high) of spinel and perovskite with rich oxygen vacancies.[214] This PCO/Co_3O_4 NC catalyst had a low overpotential of 371 mV in 0.1 M KOH at 10 mA cm^{-2} for the OER and a remarkable decrease of the half-wave potential to 0.72 V for the ORR. Similar perovskite and spinel heterojunctions greatly increased the OER performance of spinels and the ORR performance of perovskites[215,216] Dual phases of Co_3O_4 and $LaCoO_3$ are also similar to this heterojunction with the electron transfer number (n) for Co_3O_4@$LaCoO_3$ estimated to be 4.0.[216] S and P doping[217] help increase conductivity, enhancing the bifunctional performance.

4.1.3 Other oxide compounds. Besides spinels and perovskites, oxide composites with S and P-doped oxides can also achieve increased activity and conductivity. A shared edge NiO/$NiCo_2O_4$ that was hydrothermally processed with a 10 mA cm^{-2} current density at an overpotential of 264 mV outperformed the

noble catalyst RuO_2. It was shown that the highly active Ni^{3+} species generated by the oxidation of the nanometer scale NiO surface are responsible for the enhanced OER.[218] Nickel cobalt sulfide[219,220] and NiFe hydrogen sulfide[221] with excellent OER performance are also proposed as having good potential for water electrolysis and zinc–air batteries.[222,223]

Also, increased conductivity is obtained by combining two oxides, such as Co_xSe_y nanosheets on $ZnCo_2O_4$ sub-micro/nanospheres with high ORR performance and inside doping like NiCoSe Se-doped spinel.[190] Oxides modified with S and P to form CoB,[224] plasma-treated NiS,[225] CoS nanorods,[226] CoS@C,[227] Co_8S_9 (ref. 228) and Co_2P,[229] scalable COP from MOF,[230] NiCoP,[231] and CoO/CoP[232] *etc.* are also widely used in zinc–air batteries.

4.2 Metal–N–C (transition metals)

Compared to low conductivity and high peroxide selectivity, loading metal materials in the carbon network layer is a more rational design for high activity, resulting in a more complete reaction and higher speed of electron transfer in the ORR, exposing more metal active sites to the alkaline electrolyte. By mixing carbonaceous materials and metal precursors, the metal atoms that are regarded as highly active sites for both OER and ORR are receiving electrons and ions, featuring a low loading of the amount of metal on the carbon substrate. This can be mitigated by introducing heteroatoms into the carbon network, especially nitrogen atoms, which provide an additional electron in the valence shell for higher binding energy.[233] For example, with heterojunctions like Ni_3N/Co_2N, a unique flower-like nickel-cobalt layered double hydroxide (N–NiCo-LDH), redistributes electrons at the Ni_3N/Co_2N heterojunction interface

favoring the energy barrier for OERs and thus, improve the electrocatalytic activity.[234]

The electron transfer number of the ORR reaction is an important index for estimating the extent of the ORR reaction. According to the low selectivity for formation of H_2O_2, which is an undesired product of the ORR reaction, materials like metal–N/C rationally control the adsorption and desorption of intermediates in superficial structures on the metal–carbon surfaces without losing activity.[235] For different metal–N materials, a study taking advantage of the well-defined structure of the tetramethoxyphenylporphyrin (TMP P) unit, showed that the 2-electron transfer ORR reaction at the M–N_4 site (M = Mn, Fe, Co, Ni, Cu) is most efficient for Fe while Co had the lowest activity.[236]

The use of M–N/C catalysts as NPMCs started in the 1960s with the discovery of the ORR activity of cobalt phthalocyanine under alkaline conditions.[237] In recent years, in addition to macrocycles, a series of low-cost nitrogen precursors such as polyacrylonitrile (PAN), polypyrrole (PPy), polyaniline (PANI), ethylenediamine (EN), and cyanamide (CA) were utilized in the preparation of M–N/C catalysts by doping carbon supports with these metal-coordinating polymers.[238]

In this section, we discuss the common metal–N–C materials for zinc–air batteries with special reference to Co and Fe, as well

Fig. 13 Typical process for Co–N–C formation: (a) pyrolysis and annealing, (reproduced from ref. 242 with permission Copyright © 2022 Elsevier) (b) ZIF-67 coupling with electro spin, (reproduced from ref. 245 with permission Copyright © 2019 Wiley-VCH) (c) surfactant assisted. (Reproduced from ref. 247 with permission from the Royal Society of Chemistry).

as a special kind of single-atom catalyst, describing the activity and morphology of these kinds of material.

4.2.1 Co–N–C. Recently, metal–organic frameworks (MOFs) have emerged as potential precursors to prepare highly active M–N–C ORR electrocatalysts, due to the use of abundant metal, carbon, and nitrogen species. For example, the Co–N–C catalysts derived from Co-based ZIFs have shown excellent ORR performance because of the formation of porous structures and a large number of active sites after pyrolysis.[239] N-doped carbon nanomaterials (Co–N/PCNs) for ORR catalysis have been obtained by pyrolyzing a ZIF-8 encapsulated Co ion containing nanocomposite.[240]

With its very high performance, Co–N–C is suitable for use in a zinc–air battery with high durability and high electron transfer number.[241] CoN_3 active sites dispersed on N-doped graphitic carbon nanosheets enable Zn–air batteries with ultrahigh durability for over 6000 cycles (∼2000 h). The Zn–air battery based on CoSA/NC catalyst showed a high peak power density of 255 mW cm^{-2}[242] (Fig. 13a). The synergistic effects of Co–N moieties and Co metallic nanoparticles encapsulated in an N-doped carbon matrix enabled an overall oxygen redox activity (OER/ORR) of 0.72 V in 0.1 M KOH.[243] Gas transfer through the Co–N–C's porous structure can also be enhanced by morphology control. A two-step carbonization method has been reported for the synthesis of a Co–N doped coal tar pitch (CTP) carbon-based electrocatalyst that simultaneously had a hierarchical pore structure, a high degree of local order, and an efficient Co–N_x active structure.[244]

For a more porous structure, the electrodeposition of Co–N–C nanosheets on carbon felts (Co/Co–N–C) has been reported. Wavelet transforms extended X-ray absorption fine spectroscopy (WT-EXAFS) and X-ray photoelectron spectroscopy confirmed the formation of Co (mainly Co^0) and the Co–N–C (mainly Co^{2+} and Co^{3+}) structure. Co–Co and Co–N bonds existing in Co/Co–N–C could facilitate the ORR, whereas the Co–O bond is beneficial for the OER (Fig. 13b).[245]

Another way to achieve a highly active surface is to combine the supramolecular coordination polymers Co(II)-adenine (CoA) with polyacrylonitrile (PAN)/cellulose acetate (CA) in a controlled electrospinning process to synthesize nanofibers (CoA@NFs).[246] Surfactants also affect the synthesis process,[247] influencing the formation of precursors and forming a protective layer during pyrolysis (Fig. 13c). Furthermore, introduced zinc can regulate the electronic structures of electrocatalysts and construct bimetallic active sites (N–Co/N–Zn species), facilitating the adsorption of reaction intermediates and further enhancing electrocatalytic performance.[248]

4.2.2 Fe–N–C. Single-atom active sites comprising N coordinated with isolated Fe atoms have been demonstrated to be one of the most promising catalyst candidates.[249–252] Among them, iron phthalocyanine (FePc) has a clear Fe–N_4 coordination structure that is favorable for electron transport. It provides a typical model for studying the reaction mechanisms.[253] For Fe–N–C materials, the active sites can be attributed to single atoms and crystalline iron species and non-Fe sites accelerating the ORR process.
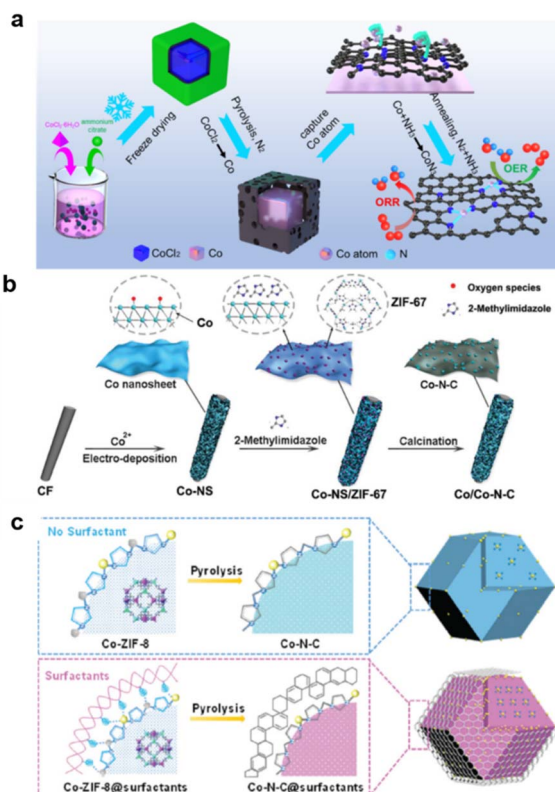
Furthermore, the synthesis methodologies can be classified as the pyrolytic strategy, deposition, and other strategies.[250] Moreover, pyrolysis always causes agglomeration, which can be reduced by electrospinning technology combined with a pyrolytic process in an NH_3 atmosphere.[254]

Typically, except for MOF-derived material,[255,256] the Fe must first coordinate with a C, N precursor with stable bonds. For example, the 11,11′-bis(dipyrido[3,2-a:2′,3′-c]phenazinyl) (bidppz) ligand was selected for the formation of a nitrogen-rich iron-coordinated coordination polymer (Fe-bidppz) that forms a self-supporting catalyst containing high concentrations of nitrogen and iron doping obtained by pyrolysis (800 °C) as shown in Fig. 14a.[238] Similarly, melamine was introduced as an added carbon source to support the growth of Fe–N/Fe sites on the nanotubes[257] and CNTs by PPy.[249] Other methods like metal co-doping could also change the Fe–N–C performance. As shown in Fig. 14b and c, by the introduction of Mn, the Fe spin in the Fe^{III} sites of metal–N–C materials is regulated more efficiently by both spin-state transition and electronic modulation, rendering excellent ORR performance and good durability of Fe, Mn/N–C in both alkaline and acidic media (half-wave potential 0.928 V in 0.1 M KOH), outperforming Pt/C.[258] The etching process of Fe^{3+} on a copper foil and then adding 2-MeIM to achieve enclosed ZIF-8, followed by pyrolysis, easily produced Cu@Fe–N–C, especially with Cu foil supported, with bimetallic active sites, large surface area, high nitrogen doping level, and conductive carbon frameworks. This material showed excellent
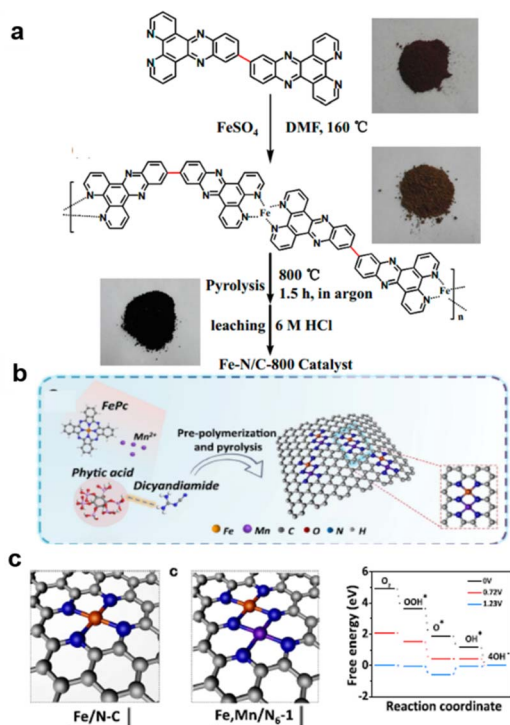

Fig. 14 Typical way for Improving Fe–N–C: (a) coupled with N polymers for higher N coupled, (reproduced from ref. 238 with permission. Copyright © 2014, American Chemical Society) (b) and (c) Mn and Fe dual metal enhancing reaction coordination. (Reproduced from ref. 258 with permission. Copyright © 2021 CC-BY).

ORR performance, with a 50 mV higher half-wave potential of 0.892 V.[259]

4.2.3 SACs. Single-atom catalysts (SACs) combine the advantages of both homogeneous and heterogeneous catalysts, which have been designed and put forward in the last century and were newly specified and developed by many groups during the last decade. In most experiments, the central metal atoms of the SACs were fixed on supports by coordination bonds with N, S, O, etc. atoms from support materials or metal–metal bonds that could change the absorption activity of reactants on metal atoms and thus influence the catalytic properties.[260,261]

A second or third carbon could be substituted by S or P to influence the electron distribution on the center metal coupled with N and C.[262] For example, in Fig. 15a,[263] with abundant tubular channels, Fe-SAs@NCTCs exhibits excellent ORR performances with high $E_{1/2}$ of 0.91 V (vs. RHE) in 0.1 M KOH by rationally controlling the active sites(SACs-CN).

Doping by black P has shown that Co–N_4–bPC (η_{ORR} = 0.31 V; η_{OER} = 0.22 V), Rh–N_4–bPC (η_{ORR} = 0.33 V; η_{OER} = 0.62 V), and Ir–N_4–bPC (η_{ORR} = 0.21 V; ηO_{ER} = 0.21 V) are promising candidates as bifunctional catalysts for both the ORR and OER and are comparable or superior to TM–N_4–graphene in terms of overpotential.[264] Boron also can be introduced into the second surrounding sites. Boron (B)-doped Co–N–C active sites confined in hierarchical porous carbon sheets (denoted as Co–N, B-CS_s) were obtained by a soft template self-assembly pyrolysis method. Significantly, the introduced B element provides an electron-deficient site that can activate electron transfer around the Co–N–C sites, strengthen the interaction with oxygenated species, and thus accelerate reaction kinetics in the $4e^-$ processed ORR and OER.[265]

Choosing the right supports for SACs is important for electrolyte infiltration and electron transfer.[266] The large specific surface area exposes a high concentration of Fe–N_4/C sites embedded in the carbon matrix. Again, as mentioned before, the Cu@Fe–N–C has a well-defined morphology of truncated rhombic dodecahedra, with excellent durability and methanol tolerance in both acidic and alkaline solutions, which makes it one of the best Pt-free catalysts reported to date for the ORR (Fig. 15b).[259]

Modulation of local atomic configurations by sulfur doping of a Fe/SNCFs-NH_3 catalyst leads to excellent ORR and enhanced OER activities. The liquid-state ZABs utilizing Fe/SNCFs-NH_3 catalyst as air cathode (Fig. 15c) deliver a high peak power density of 255.84 mW cm^{-2} and long-term cycle durability over 1000 h.[254]

Besides Fe and Co, which are common SACs and metal–N–C choices for high-ability bifunctional materials for ZABs, the metal source can be changed to Ce[267] or CuN$_3$.[268] Ultrahigh loading of Zn–N–C results in activity and stability comparable to Fe–N–C.[269] Pt-CoO has also been introduced to modulate Co SACs.[270] The Ni or Fe single atom has been demonstrated to be coordinated with four N atoms by the formation of a Ni–N_4 or Fe–N_4 planar configuration on the inner and outer walls of graphene hollow nanospheres (GHSs).[271,272] To prevent sintering, it is essential to introduce appropriate supports to optimize
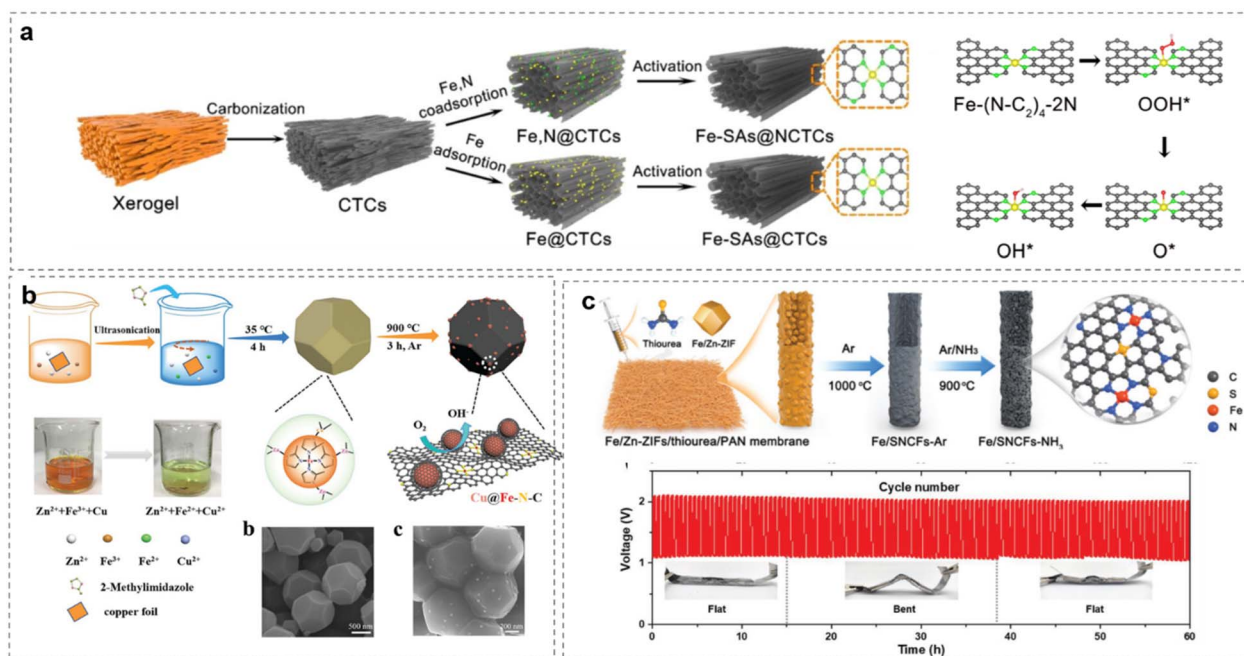
Fig. 15 Enhancing Fe-SACs by (a) N–controlling, (reproduced from ref. 263 with permission. Copyright © 2022 Elsevier) (b) Cu coupling from ZIF-8, (reproduced from ref. 259 with permission. Copyright © 2018 Wiley-VCH) (c) separating on PAN Membrane. (Reproduced from ref. 254 with permission. Copyright © 2021 Wiley-VCH).

the local coordination environment and electronic properties, as well as induce strong metal-support interactions (SMSI).[266]

4.3 Synthesis of porous hybrids

From the viewpoint of designing good bifunctional materials, the supporting materials should be porous and able to accelerate the transfer of air and matter. The inner-Helmholtz plane (IHP) and the outer-Helmholtz plane (OHP) exist in the bilayer structure at the electrode/electrolyte interface. In an alkaline medium, water will be a source of protons, and alkali metals will fill the OHP. Then, after the formation of $(O_2^{\bullet-})_{ads}$, proton transfer not only occurs in the solvation shells of O_{2ads}, and $(O_2^{\bullet-})_{ads}$ but may occur also from water molecules (adsorbed on the electrode surface). The presence of hydroxyl species facilitates the transfer of electrons from the outer sphere.[42] Hence, the kinetics of mass transfer at the catalytic layer is very important as it determines the reaction rate, especially of the ORR.

As mentioned before, the carbon-supported materials, besides inside defects and edges provided by N doping, could act as bifunctional materials, where the coupling N or C could separate and increase the metal active sites for bifunctional reaction; this has resulted in the great bifunctional activity of low-loading oxides or metal composites on the carbon material. For example, N-doped B–N[273] and MXene-like Al etched Ti_3AlC_2 (ref. 274) nanosheets with high conductivity were found to be stable in a corrosive environment and to be a potential support for loading catalyst. Coupled metallic hybrids of NiFe layered double hydroxide nanosheet/Ti_3C_2 MXene quantum dots were deposited on a nitrogen-doped graphene surface (LDH/MQD/

NG) for high-performance flexible Zn–air batteries (ZABs), as shown in Fig. 16a.[275] The electronic and chemical coupling of LDH/MQD/NG modulates the local electronic and surface structure of the active LDH to provide metallic conductivity and abundant active sites. Consequently, the ZABs have significantly improved bifunctional activity, with a power density of 113.8 mW cm^{-2} and excellent cycle stability over 150 h at 5 mA cm^{-2}, while the kinetics and electrochemical performance are improved significantly by a change in the valence states of Ni
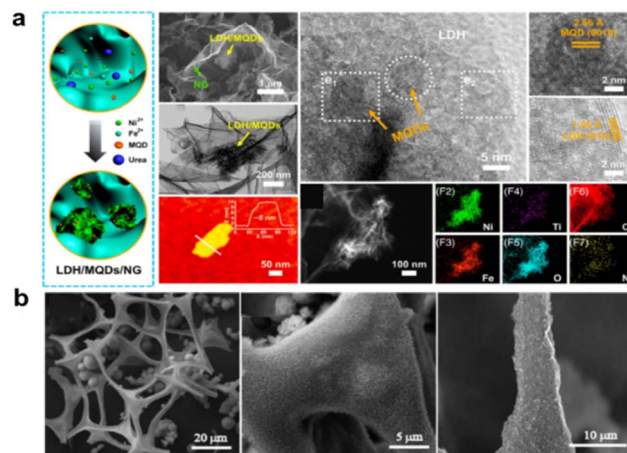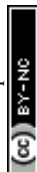

Fig. 16 Enabling high porosity: (a) LDHs on MQDs and NG (reproduced from ref. 275 with permission from X. Han *et al.* published by UESTC and John Wiley. CC BY-NC 3.0) (b) sponge CNTs and graphene.[5] (Reproduced from ref. 279 with permission from the Royal Society of Chemistry).

and Fe, M–OH vibration, flat band potential, carrier density, metallic conductivity, and Fermi energy level.[275] The graphene and CNTs are highlighted based on the widely commercialized application in other areas with a layered and separated structure for high air and mass transfer when in contact with an electrolyte.

After choosing supports, the OER active layer is loaded on a graphene-like substrate. For example, the LDH precursor of spinels like $MnCo_2O_4$,[276] $ZnCo_2O_4$,[277] or Cu–Co bimetallic oxide quantum dots[278] are loaded on CNTs or graphene. The oxides-CNTs/graphene form a hollow structure with reaction interface-conductivity channels supporting a high reaction rate. Together with carbon from bottom-up-synthesis, $NiCo_2O_4$ nanoarrays on the CNT sponge are derived from a melamine sponge to regulate the holes for air transfer between CNTs, Fig. 16b.[279]

Controlling the combination of CNTs and oxides is also challenging. After being treated with NH_3 for reduction of core–shell $CoFe_2O_4/NiFe_2O_4$ using cellulose as the precursor, the transition metal nitride/CNT hybrid $Fe_2Ni_2N/Co@NCNT$

exhibited an extremely low voltage gap with ΔE ($\Delta E = E_{j=10} - E_{1/2}$) = 0.71 V in O_2-saturated 1 M KOH solution.

Also, after 30 charges at a current density of 20 mA cm^{-2} over 1 h cycles, the *in situ*-XAFS of the air electrode showed very little difference between charging and discharging, by analyzing the Fe coordination environment, as shown in Fig. 17a and b, implying high stability of this catalyst.[280] This points to the stability of metal–N–C on typical CNTs during charging and discharging in typical ZABs.

Apart from adding the CNTs from an external source, *in situ*-grown CNTs are also widely used as efficient supports. Highly active CNTs can be obtained by treatment at 650 °C, and grown between metals. Oxidative thermal scission of the CNTs and oxidation of Co and Mn nanoparticles inside them, produced spinel Mn–Co oxide nanoparticles partially embedded in the nanotubes.[281] A novel jellyfish-like Mott–Schottky type electrocatalyst has been developed to obtain fast electron transfer and obtain fast electron transfer, and to better understand how the porous structure enhances mass transport during the ORR process. Thus, mass transport of oxygen species was improved,
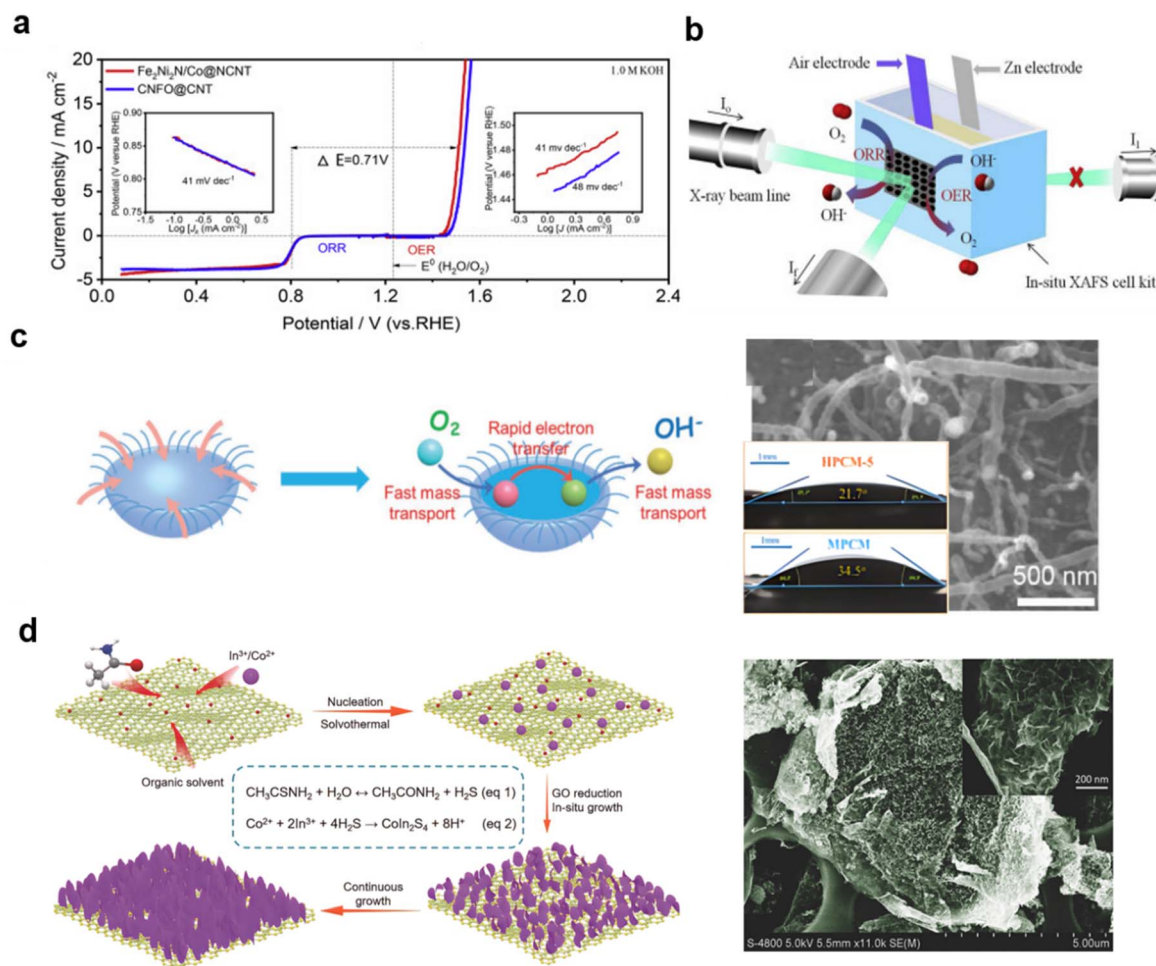

Fig. 17 Combining transition metal materials on CNTs with graphene: (a) and (b) $Fe_2Ni_2N/Co@NCNT$ with *in situ* XAFS for ZABs, (reproduced from ref. 280 with permission. Copyright © 2019 Elsevier) (c) jellyfish-like CNTs with Mott−Schottky junction, (reproduced from ref. 282 with permission Copyright © 2020 Wiley-VCH) (d) thiospinel $CoIn_2S_4$ reduced on GO. (reproduced from ref. 284 with permission. Copyright © 2018 Wiley-VCH).
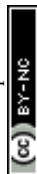
because of two effects: the electrolyte streaming effect caused by the tentacle-like carbon nanotubes; and the higher chance for effective collisions in the half-open cavity (Fig. 17c).[282]

Similarly, Co_2S on graphene can be formed also by thermolysis of a Co–thiourea complex in specially made Swagelok cells at 400 and 500 °C, resulting in pure CoS_2.[283] Also, the indium-based ternary thiospinel $CoIn_2S_4$ can be formed during the reduction of GO. As shown in Fig. 17d, the separated nanosheets help to build a large specific surface area on the GO of 102 m^2 g^{-1} and a total pore volume of 0.2 cm^3 g^{-1}.[284]

Formation of the porous structure can be assisted by using templates or special conditions. For example, a ternary nanoalloy-based oxygen electrocatalyst, $Ni_{46}Co_{40}Fe_{14}$ nanoalloy, with a size distribution of 30–60 nm, dispersed in a carbon matrix, could be formed by the sol–gel method by directly injecting benzene into a reactor at 400 °C at 2.5 MPa (supercritical reaction) followed by heat treatment at 900 °C.[285]

As shown in Fig. 18a, Fe, Co-SA/CS (single atom, carbon-supported) on nitrogen-doped hollow carbon nanospheres derived from Zn-ZIF for generating SACs and polystyrene to form spherical structures, were formed as a thin layer.[286] Carbon templates like PVDF,[169] P123,[139] and hydrogel have been reported as precursors for generating porous templates. MOF-derived samples exhibit a remaining porous structure that accelerates mass transfer.[287] Also, as shown in Fig. 18b,[288] ZIF and MPSA have been used to synthesize CoP for controlling the Co valence on graphene. In samples of Co@NC, Co_2P@NPC, Co_2P/CoP@NPC, and CoP@NPC by ratio control of ZIF and MPSA, as-synthesized Co_2P@NPC exhibited the best bifunctional ORR/OER activity among the Co_xP@NPC analogs.

Using the soft template P123 to control the Co, Co_2P/CoN particles derived from C_3N_4 were wrapped in NCNTs, controlling the growth of CNTs. (Fig. 18c).[289] By electro-spinning on a self-supported template, the catalyst can be loaded easily on carbon paper or an assembled support for application as an air cathode. The high dispersion enabled high electron and mass transfer on nanorods or nanoneedles. By combining MWCNTs, a ZIF-8-derived Co SAC is stable for 600 hours in a binder-free
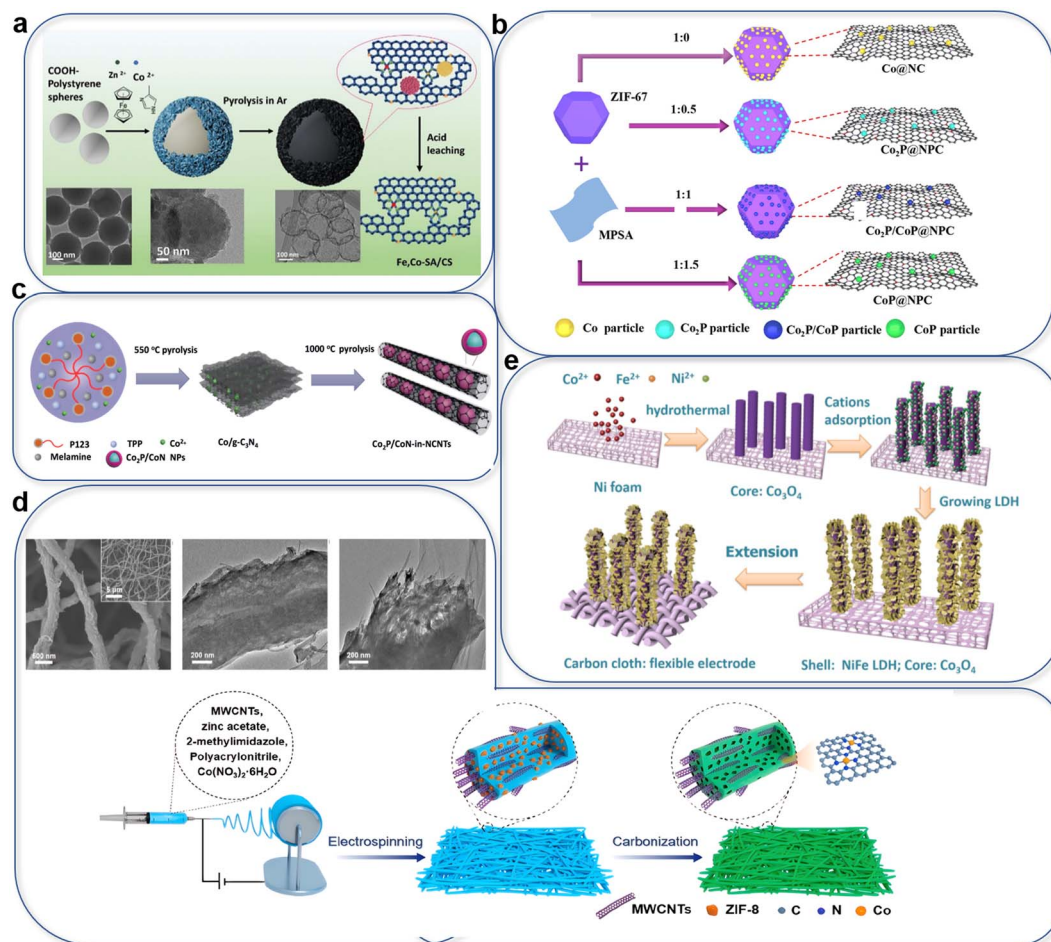

Fig. 18 Special applications enabling highly dispersed and porous structures: (a) carbon–sphere template, (reproduced from ref. 286 with permission. Copyright © 2020 Wiley-VCH) (b) ratio control of MPSA and ZIF precursor, (reproduced from ref. 288 with permission. Copyright © 2021 Zhengzhou University). (c) P123 and TPP soft-template. (Reproduced from ref. 289 with permission. Copyright © 2018 Wiley-VCH). (d) Electrospinning by PAN and MWCNTs, (reproduced from ref. 290 with permission. Copyright © 2022, American Chemical Society). (e) Self-growth of Co_3O_4 on carbon cloth. (Reproduced from ref. 291 with permission. Copyright © 2019, American Chemical Society).

zinc–air battery at 10 mA cm^{-2} (Fig. 18d).[290] Self-supported NiFe-LDH on Co_3O_4 can be loaded on carbon cloth for higher activity and flexibility (Fig. 18e).[291]

5. Reconstruction

Compared with zinc dendrite formation, electrolyte concentration loss, and failure of flexible cells, the air electrode performance may not be the main obstacle for sustainable use, but the ability to achieve low-mass loading and high current density at the air electrode still needs to be improved so that the cycle life can be lengthened before commercialization becomes feasible. RDE measurement removes the effects of diffusion and long-time corrosion in an air-abundant, stable electrolyte in the usually weakly alkaline environment.

Real-life working conditions in the electrolyte may differ, and therefore, to prevent the efficiency from decreasing, it is important to monitor the structural, crystal, and catalyst changes during and after the OER/ORR reactions and cycling in ZABs. Two key factors are worth pointing out: one is that the potential dynamics-driven methodology applied in ORR or OER measurements is different from the continuous galvanostatic technique for battery operation, and the other is that alkaline electrolytes used in Zn–air batteries are far more concentrated, so that a lower electrochemical barrier is required for valence variation of the main elements.

As mentioned before, PGM-based electrodes, which exhibit excellent stability in the OER and ORR compared with other materials, are made of expensive and scarce metals and, although ideal, are difficult to commercialize successfully in OER and ORR reactions. The high stability originates from the high active surface area and thermal stability during the reactions.[292,293] To replace the expensive metals with transition-metal-based materials while maintaining high stability and high efficiency, remains a great challenge, as the OER and ORR are three-phase reactions taking place on the catalyst surface. The catalyst is usually a nano- or micro-sized material with a complex reaction mechanism occurring in the conducting layer and diffusion layer, which determines the efficiency of the three-phase reactions. To obtain a high current density, which corresponds to a high reaction rate, a higher voltage should be applied on the electrode compared to measurement on RDE, when the reactant and catalyst interface are not abundant. Thus, the stability is highly dependent on the interactions in high current density locations, and changes during long-term cycling.

The OER process commonly proceeds at a high positive potential of more than 1.4 V. At such high potential, (sub) surface atoms on an electrocatalyst tend to be oxidized. The surface sites are therefore dynamic in nature, driving *in situ* changes and reconstruction.[294] The reconstruction involves changes in one or more forms of the composition, phase(s),
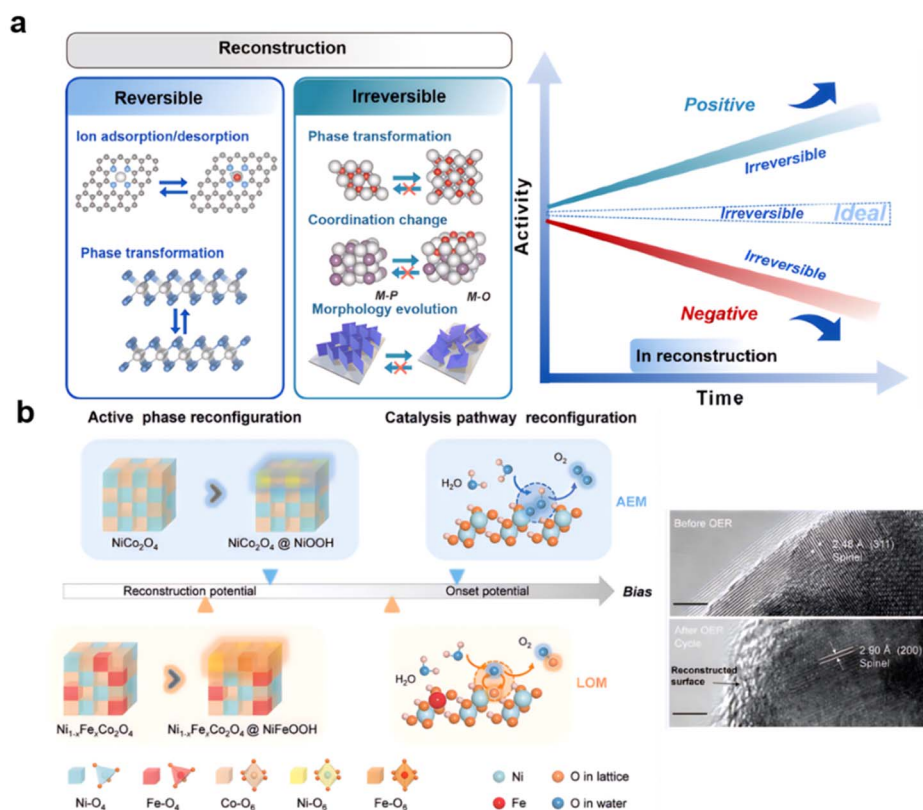

Fig. 19 (a) Diagram of different types of reconstruction and durability, (reproduced from ref. 294 with permission. Copyright © 2021 from John Wang *et al.*) (b) surface reconstruction of $NiCo_2O_4$ and Fe doped $NiCo_2O_4$. (Reproduced from ref. 299 with permission. Copyright © 2022 Wiley-VCH).

micro/nanostructures, and crystallinity, at the surface/subsurface of the pre-catalyst. These reconstruction features can be reversible or irreversible depending on the reaction and service conditions, as shown in Fig. 19a.[294]

Much research has concentrated on the reconstruction behavior during the OER process. For morphology, the self-reconstruction of Co into Co_3O_4 and CoOOH during the OER process exhibits higher adsorption energy for OH^- and presents an exothermic reaction in the OER process.[295] Testing 10 wt% to 60 wt% loading of FeCo in a ZAB at 100 mA cm^{-2} on the cathode area, cycling between 60 min of discharging and 60 min of charging, the optimal loading was found to be 40 wt%, with both $CoFe_2O_4$ and CoO nanocrystals detected. The OER catalytic activity was the limiting factor for the ZAB's cyclability.[296]

During the OER on NiCo-LDH, the low-crystallinity films were transformed from a local spinel structure to amorphous CoO at an anode potential of 0.2 V vs. Ag/AgCl and then to the active structure NiOOH-h-CoO$_2$ at 0.3 V vs. Ag/AgCl. The initial transformation from spinel to an a-CoO structure is irreversible; however, the subsequent conversion to NiOOH-h-CoO$_2$ is reversible. Incorporation of Ni into this active structure improved the OER activity of NiCoO$_x$H$_y$ catalysts, which was increased by 100% compared to when Ni was coordinated in a spinel structure.[297] At the same time, the double-exchange-induced conductivity was enhanced by another metal on the nickel-based oxyhydroxides, following a complicated dual-metal engaged mechanism during reconstruction.[298] The pathway evolution and structure evolution of the model catalyst spinel NiCo$_2$O$_4$ during water oxidation has been studied, and doping with, for instance, Fe enabled optimization of this reconfiguration, to finally establish a lifetime dynamic structure–performance correlation and obtain outstanding catalysis activity (Fig. 19b).[299]

5.1 Reconstruction of metal–N–C

Materials based on metal–N–C are considered to be good substitution materials with high ORR rates. The stability of metal–N–C is attracting attention, as the economic-efficiency can be increased when activity and reaction efficiency last longer. While non-precious metal-based catalysts (NPMCs) have emerged as highly promising alternatives, but they tend to degrade quickly under the harsh operating conditions of typical OER devices.[300] While the metal–N–C is not stable under working conditions, and operando XAFS analyses imply that initially formed Cu–N$_4$ could be transformed to Cu–N$_3$/Cu-NC under working conditions.[301] N-doping also influences stability. For example, N1-OMCHS shows remarkably high stability due to the modification of N-quaternary to N-pyridinic species, while the N-pyrrolic species are oxidized to N-quaternary species at N$_2$-OMCHS.[149] For a MOF like Prussian Blue Analog (PBA), it has been found that the partially amorphous nickel hydroxide after activation acts as an active species, and the wrapping of the shell facilitates the transformation of PBA and protects the integrity of the materials.[302]

Reports on reconstruction of metal–N–C in a ZABs level are rare. Deng et al. presents a deep understanding of cycling process. Deng et al. used a cation-carving process in which Fe^{2+} was added to attack a Co-based nano-cuboid precursor to obtain a hollow structure material denoted (Co,Fe)$_3$N_R, as shown in Fig. 20. EDS mapping then confirmed the composition as (Co$_{0.56}$Fe$_{0.44}$)$_3$N.[303] The author pointed out that the galvanostatic system for the battery is different from the potential-dynamic-driven method for OER and ORR, so that it was necessary to measure the charging and discharging processes in situ. When applied to a ZAB, the first and following cycles exhibited big differences with several cycles of "activation" as shown in Fig. 20, first discharging at 158 mW cm^{-2} and charging 225, and then discharging at 234 mW cm^{-2}. The following cycles were stable with a similar voltage gap between charge and discharge cycles. The WAXs (Fig. 20) and SXRD validate the new phase which was shown to be a hexagonal CoOOH or (Co,Fe)OOH mixture. EPR was used to determine the generated phase. During the charging phase of $g \approx 5$, Co^{2+} ions were generated, while for $g = 2$, which exhibited a maximum in (Co,Fe)$_3$N_1C, the fluctuation is considered to be due to formation of temporary Co^{4+} and oxygen vacancies. The maturation process was also recorded using XANES. In conflict with the XAS result, a higher state than CoOOH was observed, implying that the valence state of Co continues to increase after the maturation process and light reconstruction, even after only two cycles.

The shell and bulk Co do not show the same electrochemical accessibility between XAS and EPR. Another noticeable evolution is the gradual fading of the pre-edge peak at 7712 eV, implying a weakening nitride feature; the continuously increasing oxidation state of Co causes increased Co occupation of dipole-forbidden octahedral sites (described by Deng et al.) in the oxyhydroxide. Hence, Co^{II} is observed in the oxyhydroxide shell upon discharge, while Co^{IV} exists after the battery is charged. Also, a slight right shift and intensity increase of the Co–N peak is found in (Co,Fe)$_3$N_1D, while the intensity of the peak of the Co-metal shell is reduced. EXAFS was also used to identify the increased Co–O coordination number suggested by the increased Co–O/N. Starting with two major peaks at 1.4 and 2.1 Å, a slight right shift takes place with the first discharge of Co–N and shows an overlap of Co–N with the Co–O shell at 1.4 Å. A new peak at 2.5 Å corresponds to the formation of oxyhydroxides during discharge; when charging, the high valence of Co constrains the distance between neighbouring metal or oxygen in the corresponding peaks. A clear mid-layer can be seen on the XANES contour map due to reflecting O-rich and N-deficient boundaries, while more Fe occurs between the carbon coated layer and core Co–N–C material. The peak energy position and the intensity ratio of $L_3/(L_2 + L_3)$, commonly stated as the L_3 branch ratio are the main criteria of Co and Fe L-edge EELS. As a clear difference in shell and bulk regions, Fe shows higher intensity in the first discharge and similar intensity and similar ratio to Co in the second discharge corresponding to increasing Co concentration in the generated oxyhydroxide during maturation. The prediction on shell-bulk-type configuration and periodic valence swings of surficial Co between Co^{II} and Co^{IV} during cycling is confirmed. The author points out that, interestingly, the generated intermediate phase was a hexagonal crystal different from the amorphous feature
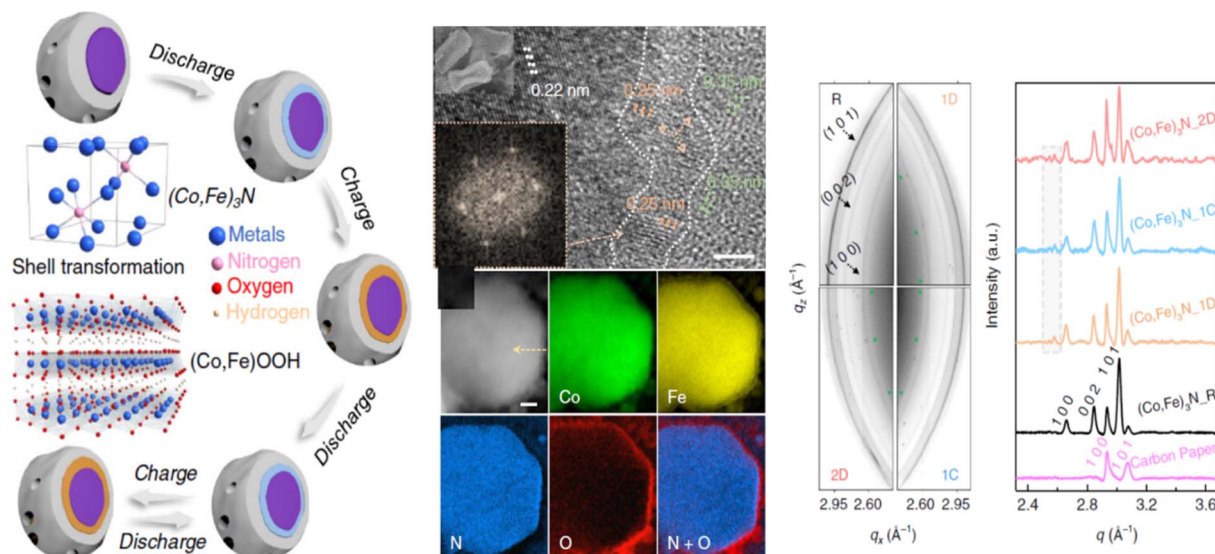
Fig. 20 Dynamic electrocatalyst with current-driven oxyhydroxide shell of $(Co,Fe)_3N$. (Reproduced from ref. 303 with permission. Copyright © from Y. Deng *et al.*).

from the previous report. Thus, Co plays an important role in the $(Co,Fe)OOH$ oxyhydroxide during battery cycling.[303]

Until recently, the main approach to improve the stability of metal–N–C and SACs has been to form strong bonds between the metal atoms and support stabilizing the single metal atoms. However, the appropriate electron transfer between isolated metal atoms and the coordination ligands could also suppress the adverse structural evolution of SACs, which leads to the

degradation of SACs. Recent advances in stable SACs have been in terms of metal and support materials, synthetic strategies, and catalytic stability in electrocatalysis.[304]

5.2 Reconstruction of transition metal-based oxides, and ramifications

As many transition-metal materials have shown, the OER process is involved in surface reconstruction and generates

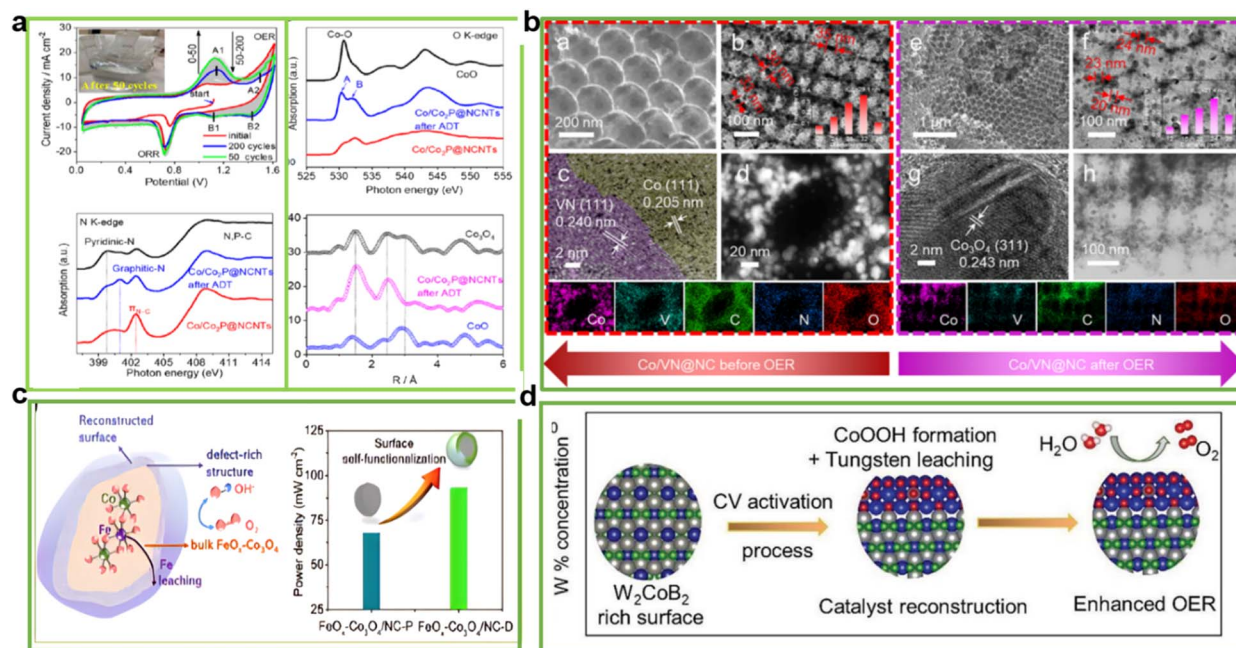**Fig. 21** Reconstruction process of (a) Co_2P, (reproduced from ref. 308 with permission. Copyright © 2021, American Chemical Society). (b) Co/VN, (reproduced from ref. 295 with permission. Copyright © 2021 published by Elsevier) (c) $FeO_x–Co_3O_4$ (reproduced from ref. 314 with permission. Copyright © 2022, American Chemical Society). and (d) W_2CoB_2 (reproduced from ref. 315 with permission. Copyright © 2022 Wiley-VCH).

oxyhydroxide. The surface layer introducing a new phase into the reaction usually exhibits a different performance from the original surface layer, especially under high current density, high voltage, long-term, and high-pH environments. The new interface with the amorphous layer and original chemicals could synergistically catalyse OER and ORR processes, based on metal valence and change of coordination state, influencing the adsorption and desorption energy needed of intermediates that determine reaction rate, and also change the structure and even compounds of origin. The non-metal elements are doped to increase the oxide's conductivity and also increase stability. But during the reaction, the crystal morphology also changes, such as Co_3O_4 spinel,[305] $NiMoO_4$,[306] and CoFe alloy doped with P on graphene.[307]

For the metal phosphides, dephosphorization during the OER process accompanying surface oxidation has been widely reported. As shown in Fig. 21a, Co/Co_2P heterojunctions on N-doped carbon nanotubes provide higher bifunctional activity with E_{gap} at 0.68 V. However, high-potential operation can result in irreversible structural damage to the amorphous carbon materials. After the OER process (1.1–2.1 V vs. RHE), Co/Co_2-P@NCNTs and Co@NCNTs electrodes demonstrated a greatly enhanced stability. The Co oxyhydroxides are formed during cycling from the Co^{2+}/Co^{3+} couple and Co^{3+}/Co^{4+} couple with mean state at 3+. Spectra of the N K-edge reveal the transformation from π_{N-C} to graphitic-N after the ADT test, which confirms the restructuring of N active sites, which may not decrease performance in ORR the reaction,[308] similarly on $MnCoP$,[309] $NiCoP$,[231] and NiS.[310]

Morphology also changed during the reaction of Co/VN with three-dimensionally ordered macroporous architecture. VN worked as a sacrificial promoter to accelerate the conversion of Co into CoOOH and Co_3O_4, which are the true active components during the OER process (Fig. 21b).[295] Further analysis of the size-dependent structural transformation during the OER of CoOOH, showed that electron redistribution and oxyl radical (M–O$^\cdot$) formation within the surface $Co^{3+}-O_6$ units is triggered as a predominant surface-terminating motif, contrasting the long-standing view of high-valence metal ions driving the OER, and leading to a fundamental understanding of the oxygen-evolving near-surface chemistry. Also, S-doped CoS was transformed to CoS_x at 0.5 mA cm^{-2} after 12.5 min treatment, and CoS_x crystallization to CoOOH is initiated on the surface of the electrocatalysts with a morphology change via the $Co(OH)_2$ intermediate during the OER measurement, where CoOOH is confirmed as the actual active species.[311,312]

The reconstruction process enhances the faces and generates vacancies, thereby accelerating the reaction. Activation of the $MnCo_2O_4$ ($MnCo_2O_4$-A) surface structure with a high Mn/Co tetrahedron occupancy, displays excellent ORR performance via the four-electron pathway with an ultrahigh onset potential and half-wave potential of 0.78 and 0.92 V, respectively, ideal mass activity (MA), and turnover frequency (TOF) values.[313] Similarly, the Fe^{3+} leaching will increase the oxygen vacancies, at the same time increase performance, but if this continues, the danger of crystal destruction is real (Fig. 21c).[314]
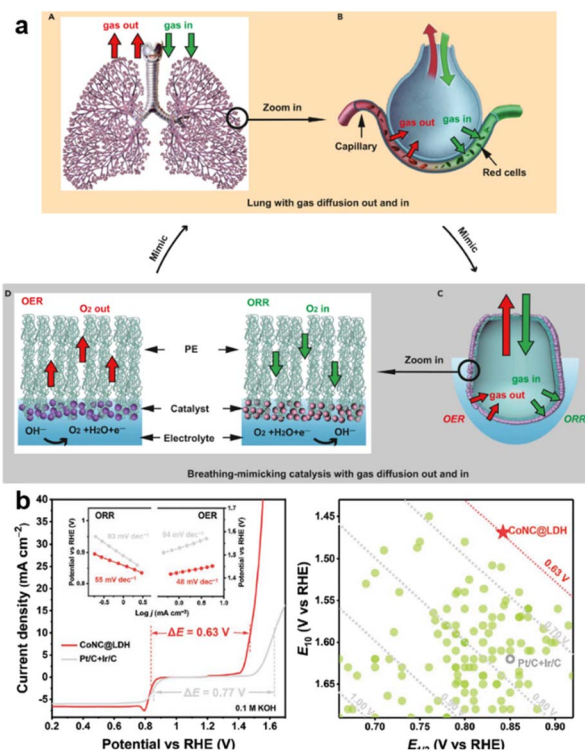

Fig. 22 (a)"Lung-inspired" air cathode (reproduced from ref. 320 with permission. Copyright © 2021 Wiley-VCH) (b) CoNC@LDH with extremely high performance. (reproduced from ref. 322 with permission. Copyright © 2021 Wiley-VCH).

Similarly, a newly formed layer was also detected during the OER reaction on W_xCoB_x. The bifunctional material for zinc–air or water oxidation underwent Co^{3+} formation during the CV test. The OER and ORR reactions were enhanced by the formation of an amorphous layer of (oxy)-hydroxide. Theoretical calculations provided an insight into the energy needed to form *OOH from *O due to its large energy barrier, which is therefore the rate-determining step (RDS) for the OER process. The new CoOOH–W_2CoB_2 interface provides a lower energy barrier than the original phase, and Co and B in W_2CoB_2 are easy to oxidize according to a Bader charge analysis. Pronounced electron redistribution is observed throughout the CoOOH–W_2CoB_2 system caused by the more conductive electronic structure of W_2CoB_2, which is beneficial for providing more electrons to the CoOOH layer (Fig. 21d).[315]

6. Conclusion and perspectives

6.1 Rational design of bifunctional materials

Based on the foregoing analysis of selected bifunctional materials, apart from considering performance, stability is also an important index for long-time usage. Flexible and rechargeable batteries are different from traditional batteries.[316] The procedure for rationally designing OER and ORR catalysts can be separated into four steps.

(1) Choosing a good support. The support should be highly conductive and porous, but at the same time the structure
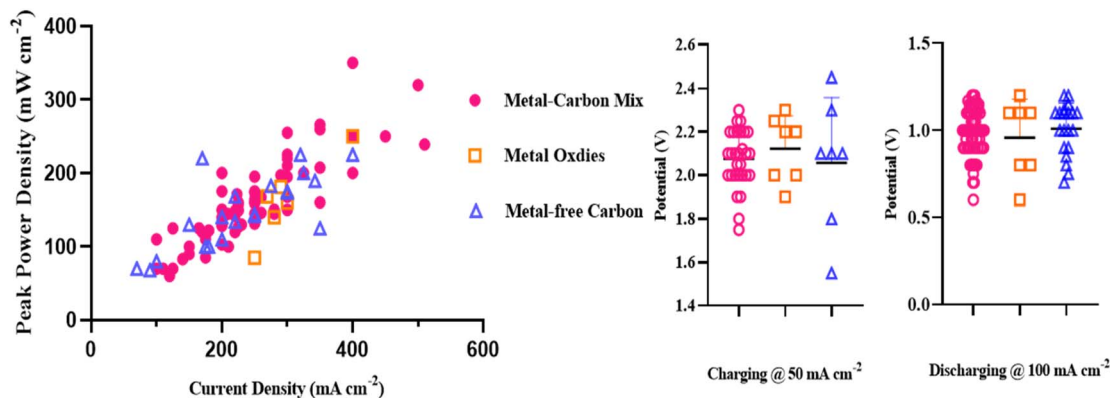
Fig. 23 Performance of different type of catalysts in the zinc–air battery according to reports.[91,100,105,106,128,130,131,133–135,141,144,148,187,189,192,194,198,212,214,216,225,226,240,242,246,248,253–255,257,258,263,267,287,289,290,295,308,314,322,329–385]

should be stable and withstand the alkaline conditions. Heterostructure support will help greatly.[317] Carbon materials like graphene, CNTs, and fibers[318] are widely used in this area. Active sites like those of metal–N–C can be embedded into a kind of layered structure and oxides can be attached to CNTs for increased conductivity.[120]

(2) Choosing a high activity ORR catalyst. ORR reactions determine the discharge power density in a low ambient electrolyte. The commercially popular MnO_2 and spinels like Co_3O_4 are also a good basis for ORR application. N-doped carbon materials can also support the ORR reaction. In recent years, metal–N and metal–C structures that significantly increase the electron transfer number (close to 4) and separate the active metal sites with C–N bonds, controlling the e_g orbital and enhancing the transformation of intermediates, have been widely studied by researchers. Specially formed SACs also provide an ideal basis for N–C coupling with metals. The stability of these metals in the alkaline environment is not so good compared to oxides, after completely cycling through both OER and ORR. So, two possible future directions for rational design could be for long-term use or for quick discharge.

(3) Choosing the OER catalysts. This is the next choice after selecting a good catalyst for the ORR. For transition metals, the perovskites and spinels are good catalysts exhibiting both high activity and high stability. However, their low conductivity and small surfaces with fewer edges and site exposure limit the use of these kinds of particles. Although metal–N–C also shows great potential, the stability in alkaline medium, especially during the OER process with additional potential, which can change the crystal structure if the voltage is high enough, will limit the application of N–C materials for long-term use. An OER reaction that generates high-rate bubbles also demands good adherence to the current collector layer and air diffusion layer for mechanical stability.[300]

(4) Modulation of synthesis techniques. To further improve the performance and stability of the material, further modifications of the chosen materials are also needed. For example, increasing oxygen vacancies will increase the performance of oxides like spinels, and optimum loading of S and P will change the conductivity and also the e_g orbital control for a more

efficient reaction. For carbon-based materials, N doping could greatly enhance their activity in the ORR by increasing the number of edges and defects inside. Doping of the carbon and nitrogen sources could further affect the C–N bonds, where the electrons are important in the OER and ORR processes. Size control[311] and porosity are also important influences on oxygen transfer.

Highly porous materials are also desirable for highly conductive materials with multi-channels to transport air and reactants. Carbon-based materials combined with transition metal compounds, like MOF with porous structure,[319] modulated to form porous and multi-channel structures, are very important in the highly alkaline environments with low oxygen levels needed for longtime cycling in the electrolyte in both solid and aqueous zinc–air batteries. The "lung model" helps build air channels for high gas mass transfer rates (Fig. 22a).[320] The porous structure of carbon-based materials can be derived from polymers or MOF materials, while some hard-templated models, commonly with high N contents, are also useful. Electro-spun or self-supported[321] materials are also widely used to control the morphology. Finally, the ideal product is recommended to be a functional material combining OER and ORR catalysts with highly porous structure and highly uniform dispersion. As shown in Fig. 22b, simply combining Co/NC and LDH could reach extremely high performance, pointing to the possibility of such design routes.[322]

More and more techniques will help us understand the reconstruction process during the OER and ORR processes. Operando techniques have provided insightful information on the underlying mechanism of a metal-based catalyst. It is expected that if the same information is attainable for MFC systems, great advances in MFC technology can be achieved.[323]

Also, besides synthesizing catalysts from synthetic chemical products, the source of the catalyst could be environmentally friendly and easily-sourced. Biomass[324] or recycled carbon-based materials can be combined with C_3N_4 (ref. 325) as carbon-based precursor to synthesize bifunctional materials.

6.2 Stability considerations

As mentioned before, the stability of carbon in the alkaline electrolyte during the OER process is still a big problem for metal-based materials. However, these are not the main limitations of the zinc–air batteries, based on the complicated structure for assembly. The zinc are also unstable in some aqueous electrolyte.

For an aqueous battery at ambient temperature, the electrolyte[326] and zinc dendrites[27] often cause a loss of efficiency, so the design of the cell is very important, while MnO_2 is a good material for low-current density use.[28] Moreover, the mechanical stability of an air electrode that generates high-volume bubbles will cause the catalyst layer to fail. Selection of the right binder materials and changes in the assembly process may ultimately help solve this problem in aqueous or flexible batteries.

The reconstruction process for both oxides and metal–N–C is determined by the reaction rate of the OER reaction while the combined interface will accelerate the ORR reaction during the charging and discharging processes. That means, for example, if LDHs are used in the charging and discharging processes, the stability of the materials may not be good. However, the good news is that when applying the same current density for the OER reaction, a high-performance catalyst will normally need a lower potential, which is low enough that it will not affect the crystal's stability. So when choosing bifunctional materials, the intended use and desired stability strongly affect the catalyst choice for either quick discharge or long-term stability (*i.e.*, better, longer).

An ideal bifunctional battery catalyst for air electrodes should include: a thin and highly active oxyhydroxide shell that serves as the primary activity contributor responsible for catalyzing the oxygen reaction in battery cycling; and a highly conductive bulk material to maintain the electrochemical kinetics.[303] Therefore, compared to direct loading of a highly active oxyhydroxide on carbon materials, rational design with highly-dispersed oxides or metal–N–C on carbon materials with strong bonds will allow the generated reaction sites to benefit from the carbon supports and have no limitation on the ORR. (Also, the stability of the carbon will be enhanced).

6.3 Outlook

Based on the increasing volume of articles and increasing research on zinc–air battery air-cathode catalysts, the use of carbon-based materials and N doping allows the performance of catalysts to reach higher efficiencies than traditional MnO_2. However, the processes and techniques for newly made materials have not yet reached maturity with lower costs and higher stability.

Notably, the traditional electrochemical test results suggest that electrochemical tests conducted at low current densities may be inadequate in predicting practical battery cycling performance[296] or performance at low temperature.[327] More advanced monitoring of the efficiency loss during cycling in the real high-alkalinity electrolyte will help estimate the relationship between the crystal structure of functional material and

conditions like mass, potential, and current density.[22] By defect engineering, heteroatom doping, and vacancy construction, more efficient catalysts may be produced for different electrocatalytic reactions. More and more new, high-potential materials like MOFs are being designed that can be used in many energy-conversion materials,[328] and carbon-free functional catalysts like graphene and CNTs are finding wide application in different areas.

We have categorized 100 reports on zinc–air batteries with performance of different bifunctional materials. Fig. 23 portrays the peak power density and potential for charging @ 50 mA cm^{-2} and discharging @ 100 mA cm^{-2}. Although most reported peak power densities of zinc–air batteries are between 50 and 200 mW cm^{-2}, and only a few excellent results have reached levels higher than 250 mW cm^{-2}, by rational design and advanced energy storage research, it should be possible to achieve better and more active electrocatalysts with high stability and longer battery cycle time.

No rational relationship between performance and the type of catalyst could be observed, pointing to more important requirements in upgrading equipment for higher ability (Fig. 23).[91,100,105,106,128,130,131,133–135,141,144,148,187,189,192,194,198,212,214,216,225, 226,240,242,246,248,253–255,257,258,263,267,287,289,290,295,308,314,322,329–385]

As a backup battery, higher actual specific energy is expected to meet the needs of wearable devices; zinc–air batteries need a flexible substrate and high-power output.

Therefore, follow-up ZAB research directions should look into compounding with other materials with the objective to increase the number of active sites, and especially to prepare atom-dispersed electrocatalysts.

Author contributions

Wanqi Tang: writing, review, and editing; Jiarong Mai: writing and review; Lili Liu: review and editing; Nengfei Yu: review and editing; Lijun Fu: review and editing; Yuhui Chen: review and editing; Yankai Liu: review; Yuping Wu: supervision, writing-review and editing, funding acquisition; and Teunis van Ree: writing, review, and editing.

Conflicts of interest

There are no conflicts to declare.

Acknowledgements

Notes and references

1 M. Xu, J. Qu and M. Li, *Sustainability*, 2022, **14**, 10014.
2 R. Schlogl, *ChemSusChem*, 2010, **3**, 209–222.
3 Y. Li and J. Lu, *ACS Energy Lett.*, 2017, **2**, 1370–1377.

4 Q. Xia, Y. Zhai, L. Zhao, J. Wang, D. Li, L. Zhang and J. Zhang, *Energy Mater.*, 2022, **2**, 200015.

5 M. Balaish, A. Kraytsberg and Y. Ein-Eli, *Phys. Chem. Chem. Phys.*, 2014, **16**, 2801–2822.

6 P. Gu, M. Zheng, Q. Zhao, X. Xiao, H. Xue and H. Pang, *J. Mater. Chem. A*, 2017, **5**, 7651–7666.

7 Y. Dai, J. Yu, C. Cheng, P. Tan and M. Ni, *Chem. Eng. J.*, 2020, **397**, 125516.

8 Y. Li, M. Gong, Y. Liang, J. Feng, J. E. Kim, H. Wang, G. Hong, B. Zhang and H. Dai, *Nat. Commun.*, 2013, **4**, 1805.

9 K. Tang, H. Hu, Y. Xiong, L. Chen, J. Zhang, C. Yuan and M. Wu, *Angew. Chem., Int. Ed. Engl.*, 2022, **61**, e202202671.

10 X. Chen, Z. Zhou, H. E. Karahan, Q. Shao, L. Wei and Y. Chen, *Small*, 2018, **14**, e1801929.

11 D. Yang, L. Zhang, X. Yan and X. Yao, *Small Methods*, 2017, **1**, 1700209.

12 J. Sun, C. Liu, X. Song, J. Zhang, Y. Liu, L. Liang, R. Jiang and C. Yuan, *Appl. Phys. Rev.*, 2022, **9**, 031301.

13 J. Chang, G. Wang and Y. Yang, *Small Sci.*, 2021, **1**, 2100044.

14 J. Wu, B. Liu, X. Fan, J. Ding, X. Han, Y. Deng, W. Hu and C. Zhong, *Carbon Energy*, 2020, **2**, 370–386.

15 Z. Huang, J. Wang, Y. Peng, C. Jung, A. Fisher and X. Wang, *Adv. Energy Mater.*, 2017, **7**, 1700544.

16 M. Tang, S. Zhang and S. Chen, *Chem. Soc. Rev.*, 2022, **51**, 1529–1546.

17 R. Yoo, E. Pranada, D. Johnson, Z. Qiao and A. Djire, *J. Electrochem. Soc.*, 2022, **169**, 063513.

18 B. Yao, Y. He, S. Wang, H. Sun and X. Liu, *Int. J. Mol. Sci.*, 2022, **23**, 6036.

19 L. Tang, Q. Xu, Y. Zhang, W. Chen and M. Wu, *Electrochem. Energy Rev.*, 2022, **5**, 32–81.

20 Z. Ye, L. Zhao, A. Nikiforov, J. M. Giraudon, Y. Chen, J. Wang and X. Tu, *Adv. Colloid Interface Sci.*, 2022, **308**, 102755.

21 X. Liu, G. Zhang, L. Wang and H. Fu, *Small*, 2021, **17**, e2006766.

22 S. Lee, J. Choi, M. Kim, J. Park, M. Park and J. Cho, *Chem. Sci.*, 2022, **13**, 6159–6180.

23 M. Luo, W. Sun, B. B. Xu, H. Pan and Y. Jiang, *Adv. Energy Mater.*, 2020, **11**, 2002762.

24 J. Pan, Y. Y. Xu, H. Yang, Z. Dong, H. Liu and B. Y. Xia, *Adv. Sci.*, 2018, **5**, 1700691.

25 J. Liu, C. Zhao, J. Wang, D. Ren, B. Li and Q. Zhang, *Energy Environ. Sci.*, 2022, **15**, 4542–4553.

26 Y. Deng, R. Liang, G. Jiang, Y. Jiang, A. Yu and Z. Chen, *ACS Energy Lett.*, 2020, **5**, 1665–1675.

27 M. Wu, G. Zhang, H. Yang, X. Liu, M. Dubois, M. A. Gauthier and S. Sun, *InfoMat*, 2021, **4**, 12265.

28 Y. Zhang, Z. Chen, H. Qiu, W. Yang, Z. Zhao, J. Zhao and G. Cui, *NPG Asia Mater.*, 2020, **12**, 4.

29 Z. Zhao, X. Fan, J. Ding, W. Hu, C. Zhong and J. Lu, *ACS Energy Lett.*, 2019, **4**, 2259–2270.

30 Q. Li, R. Cao, J. Cho and G. Wu, *Adv. Energy Mater.*, 2014, **4**, 1301415.

31 L. Yang, J. Shui, L. Du, Y. Shao, J. Liu, L. Dai and Z. Hu, *Adv. Mater.*, 2019, **31**, e1804799.

32 C. X. Zhao, J. N. Liu, J. Wang, D. Ren, B. Q. Li and Q. Zhang, *Chem. Soc. Rev.*, 2021, **50**, 7745–7778.

33 Y. Nie, L. Li and Z. Wei, *Chem. Soc. Rev.*, 2015, **44**, 2168–2201.

34 S. Cherevko, S. Geiger, O. Kasian, N. Kulyk, J. Grote, A. Savan, B. R. Shrestha, S. Merzlikin, B. Breitbach, A. Ludwig and K. J. J. Mayrhofer, *Catal. Today*, 2016, **262**, 170–180.

35 M. E. Lyons and S. Floquet, *Phys. Chem. Chem. Phys.*, 2011, **13**, 5314–5335.

36 J. Cheng, H. Zhang, G. Chen and Y. Zhang, *Electrochim. Acta*, 2009, **54**, 6250–6256.

37 E. Antolini, *ACS Catal.*, 2014, **4**, 1426–1440.

38 Y. E. Roginskaya, T. V. Varlamova, M. D. Goldstein, I. D. Belova, B. S. Galyamov, R. R. Shifrina, V. A. Shepelin and V. N. Fateev, *Mater. Chem. Phys.*, 1991, **30**, 101–113.

39 J. Zhao, C. Fu, K. Ye, Z. Liang, F. Jiang, S. Shen, X. Zhao, L. Ma, Z. Shadike, X. Wang, J. Zhang and K. Jiang, *Nat. Commun.*, 2022, **13**, 685.

40 J. Scholz, M. Risch, K. A. Stoerzinger, G. Wartner, Y. Shao-Horn and C. Jooss, *J. Phys. Chem. C*, 2016, **120**, 27746–27756.

41 J. Wang, C. Zhao, J. Liu, D. Ren, B. Li, J. Huang and Q. Zhang, *Nano Mater. Sci.*, 2021, **3**, 313–318.

42 X. Ge, A. Sumboja, D. Wuu, T. An, B. Li, F. W. T. Goh, T. S. A. Hor, Y. Zong and Z. Liu, *ACS Catal.*, 2015, **5**, 4643–4667.

43 J. Zhang, Y. Yuan, L. Gao, G. Zeng, M. Li and H. Huang, *Adv. Mater.*, 2021, **33**, e2006494.

44 V. Tripković, E. Skúlason, S. Siahrostami, J. K. Nørskov and J. Rossmeisl, *Electrochim. Acta*, 2010, **55**, 7975–7981.

45 V. Stamenkovic, B. S. Mun, K. J. Mayrhofer, P. N. Ross, N. M. Markovic, J. Rossmeisl, J. Greeley and J. K. Norskov, *Angew. Chem., Int. Ed.*, 2006, **45**, 2897–2901.

46 Y. Bing, H. Liu, L. Zhang, D. Ghosh and J. Zhang, *Chem. Soc. Rev.*, 2010, **39**, 2184–2202.

47 V. R. Stamenkovic, B. S. Mun, M. Arenz, K. J. Mayrhofer, C. A. Lucas, G. Wang, P. N. Ross and N. M. Markovic, *Nat. Mater.*, 2007, **6**, 241–247.

48 L. Chen, X. Xu, W. Yang and J. Jia, *Chin. Chem. Lett.*, 2020, **31**, 626–634.

49 S. Wu, X. Xu, Y. Ren, X. Guo, H. Sun and G. Zhou, *Ionics*, 2021, **28**, 1017–1036.

50 R. Paul, L. Zhu, H. Chen, J. Qu and L. Dai, *Adv. Mater.*, 2019, **31**, e1806403.

51 D. Wang and D. Su, *Energy Environ. Sci.*, 2014, **7**, 576–591.

52 L. Wang, Z. Liu and J. Zhang, *Nanoscale*, 2022, **14**, 13473–13489.

53 D. Yan, Y. Li, J. Huo, R. Chen, L. Dai and S. Wang, *Adv. Mater.*, 2017, **29**, 1606459.

54 R. Paul, Q. Dai, C. Hu and L. Dai, *Carbon Energy*, 2019, **1**, 19–31.

55 A. Parkash, N. Solangi, T. H. Seehar, G. Zhang, M. Akram and S. Ali, *ECS J Solid State Sci. Technol.*, 2022, 11.

56 J. Ortiz-Medina, Z. Wang, R. Cruz-Silva, A. Morelos-Gomez, F. Wang, X. Yao, M. Terrones and M. Endo, *Adv. Mater.*, 2019, **31**, e1805717.

57 M. Steenackers, A. M. Gigler, N. Zhang, F. Deubel, M. Seifert, L. H. Hess, C. H. Lim, K. P. Loh, J. A. Garrido, R. Jordan, M. Stutzmann and I. D. Sharp, *J. Am. Chem. Soc.*, 2011, **133**, 10490–10498.

58 S. Kang, S. Park, D. Kim, S. Y. Park, R. S. Ruoff and H. Lee, *Adv. Funct. Mater.*, 2011, **21**, 108–112.

59 T. Ma, S. Dai, M. Jaroniec and S. Z. Qiao, *Angew. Chem., Int. Ed. Engl.*, 2014, **53**, 7281–7285.

60 L. Jiao, X. Wang, G. Diankov, H. Wang and H. Dai, *Nat. Nanotechnol.*, 2010, **5**, 321–325.

61 D. Yu, K. Goh, H. Wang, L. Wei, W. Jiang, Q. Zhang, L. Dai and Y. Chen, *Nat. Nanotechnol.*, 2014, **9**, 555–562.

62 L. Ci, L. Song, D. Jariwala, A. L. ElÃ-as, W. Gao, M. Terrones and P. M. Ajayan, *Adv. Mater.*, 2009, **21**, 4487–4491.

63 X. H. Li and M. Antonietti, *Angew. Chem., Int. Ed.*, 2013, **52**, 4572–4576.

64 J. Duan, S. Chen, M. Jaroniec and S. Z. Qiao, *ACS Catal.*, 2015, **5**, 5207–5234.

65 J. Liang, Y. Jiao, M. Jaroniec and S. Z. Qiao, *Angew. Chem., Int. Ed. Engl.*, 2012, **51**, 11496–11500.

66 Y. Arafat, M. R. Azhar, Y. Zhong, M. O. Tadé and Z. Shao, *Mater. Res. Bull.*, 2021, **140**.

67 B. Wu, H. Meng, D. M. Morales, F. Zeng, J. Zhu, B. Wang, M. Risch, Z. J. Xu and T. Petit, *Adv. Funct. Mater.*, 2022, **32**, 2204137.

68 H. Wang, C. Tang, C. X. Zhao, J. Q. Huang and Q. Zhang, *Adv. Funct. Mater.*, 2022, **32**, 1803329.

69 H. Yang, J. Miao, S. Hung, J. Chen, H. Tao, X. Wang, L. Zhang, R. Chen, J. Gao, H. M. Chen, L. Dai and B. Liu, *Sci. Adv.*, 2016, **2**, e1501122.

70 Z. Luo, S. Lim, Z. Tian, J. Shang, L. Lai, B. MacDonald, C. Fu, Z. Shen, T. Yu and J. Lin, *J. Mater. Chem.*, 2011, **21**, 8038–8044.

71 Y. Okamoto, *Appl. Surf. Sci.*, 2009, **256**, 335–341.

72 T. Xiang, Z. Wu, Z. Sun, C. Cheng, W. Wang, Z. Liu, J. Yang and B. Li, *J. Colloid Interface Sci.*, 2022, **610**, 486–494.

73 Q. Lai, K. Wei, Z. Tang, X. Liu, J. Zheng and Y. Liang, *J. Mater. Sci.*, 2021, **56**, 19577–19588.

74 L. Tao, Q. Wang, S. Dou, Z. Ma, J. Huo, S. Wang and L. Dai, *Chem. Commun.*, 2016, **52**, 2764–2767.

75 J. Barrio, M. Volokh and M. Shalom, *J. Mater. Chem. A*, 2020, **8**, 11075–11116.

76 D. Sharma and B. K. Satapathy, *Polym. Rev.*, 2021, **62**, 439–484.

77 W. Li, C. Wang and X. Lu, *Coord. Chem. Rev.*, 2022, **464**.

78 J. Zhang, Z. Zhao, Z. Xia and L. Dai, *Nat. Nanotechnol.*, 2015, **10**, 444–452.

79 J. He, Y. He, Y. Fan, B. Zhang, Y. Du, J. Wang and P. Xu, *Carbon*, 2017, **124**, 630–636.

80 G. Wu, N. H. Mack, W. Gao, S. Ma, R. Zhong, J. Han, J. K. Baldwin and P. Zelenay, *ACS Nano*, 2012, **6**, 9764–9776.

81 H. Sun, P. Zhou, X. Ye, J. Wang, Z. Tian, Z. Zhu, C. Ma, W. Liang and A. Li, *J. Colloid Interface Sci.*, 2022, **617**, 11–19.

82 H. Li, M. R. Gadinski, Y. Huang, L. Ren, Y. Zhou, D. Ai, Z. Han, B. Yao and Q. Wang, *Energy Environ. Sci.*, 2020, **13**, 1279–1286.

83 D. Li, B. Wang, X. Long, W. Xu, Y. Xia, D. Yang and X. Yao, *Angew. Chem., Int. Ed. Engl.*, 2021, **60**, 26483–26488.

84 Y. Chang, G. Zhang, B. Han, H. Li, C. Hu, Y. Pang, Z. Chang and X. Sun, *ACS Appl. Mater. Interfaces*, 2017, **9**, 29753–29759.

85 E. Gottlieb, K. Matyjaszewski and T. Kowalewski, *Adv. Mater.*, 2019, **31**, e1804626.

86 J. Sheng and Y. Li, *ACS Appl. Mater. Interfaces*, 2022, **14**, 20455–20462.

87 R. Ma, G. Lin, Y. Zhou, Q. Liu, T. Zhang, G. Shan, M. Yang and J. Wang, *npj Comput. Mater.*, 2019, **5**, 78.

88 H. Yao, Y. Zhao, N. Yang, W. Hao, H. Zhao, S. Li, J. Zhu, L. Shen and W. Fang, *J. Energy Chem.*, 2022, **65**, 141–148.

89 F. Zhang, P. C. Sherrell, W. Luo, J. Chen, W. Li, J. Yang and M. Zhu, *Adv. Sci.*, 2021, **8**, e2102859.

90 J. Jiang, J. Turnbull, W. Lu, P. Boguslawski and J. Bernholc, *J. Chem. Phys.*, 2012, **136**, 014702.

91 F. Qiang, J. Feng, H. Wang, J. Yu, J. Shi, M. Huang, Z. Shi, S. Liu, P. Li and L. Dong, *ACS Catal.*, 2022, **12**, 4002–4015.

92 S. A. Shaik, S. Sengupta, R. S. Varma, M. B. Gawande and A. Goswami, *ACS Sustainable Chem. Eng.*, 2020, **9**, 3–49.

93 R. Rabeya, S. Mahalingam, A. Manap, M. Satgunam, M. Akhtaruzzaman and C. H. Chia, *Int. J. Quantum Chem.*, 2022, 122.

94 Y. Han, D. Tang, Y. Yang, C. Li, W. Kong, H. Huang, Y. Liu and Z. Kang, *Nanoscale*, 2015, **7**, 5955–5962.

95 Y. Huang and W. Liao, *Appl. Surf. Sci.*, 2019, 495.

96 Q. Pang, L. Yang and Q. Li, *Small Struct.*, 2022, **3**, 202100203.

97 D. Liu, L. Dai, X. Lin, J. F. Chen, J. Zhang, X. Feng, K. Mullen, X. Zhu and S. Dai, *Adv. Mater.*, 2019, **31**, e1804863.

98 J. P. Paraknowitsch and A. Thomas, *Energy Environ. Sci.*, 2013, **6**, 2839–2855.

99 F. Yang, X. Liu, H. Zhang, J. Zhou, J. Jiang and X. Lu, *Energy Stor. Mater.*, 2020, **30**, 138–145.

100 P. Wei, X. Li, Z. He, X. Sun, Q. Liang, Z. Wang, C. Fang, Q. Li, H. Yang, J. Han and Y. Huang, *Chem. Eng. J.*, 2021, **422**, 130134.

101 G. Kang, S. Lee, D. C. Lee, C. W. Yoon and H. Joh, *Curr. Appl. Phys.*, 2020, **20**, 456–461.

102 X. Chen, Y. Xie, Y. Shao, K. Shen and Y. Li, *ACS Appl. Mater. Interfaces*, 2021, **13**, 42598–42604.

103 Y. Zheng, Y. Jiao, L. Ge, M. Jaroniec and S. Z. Qiao, *Angew. Chem., Int. Ed. Engl.*, 2013, **52**, 3110–3116.

104 L. Yang, S. Jiang, Y. Zhao, L. Zhu, S. Chen, X. Wang, Q. Wu, J. Ma, Y. Ma and Z. Hu, *Angew. Chem., Int. Ed. Engl.*, 2011, **50**, 7132–7135.

105 H. Li, T. A. Ha, S. Jiang, C. Pozo-Gonzalo, X. Wang, J. Fang, P. C. Howlett and X. Wang, *Electrochim. Acta*, 2021, **377**, 138089.

106 Y. Wang, R. Gan, S. Zhao, W. Ma, X. Zhang, Y. Song, C. Ma and J. Shi, *Appl. Surf. Sci.*, 2022, **598**, 153891.

107 W. Lei, Y. Deng, G. Li, Z. P. Cano, X. Wang, D. Luo, Y. Liu, D. Wang and Z. Chen, *ACS Catal.*, 2018, **8**, 2464–2472.

108 T. Liu, S. Feng, J. Huo, Q. Li, C. Xie and S. Wang, *ChemCatChem*, 2018, **10**, 4562–4568.

109 H. Jiang, J. Gu, X. Zheng, M. Liu, X. Qiu, L. Wang, W. Li, Z. Chen, X. Ji and J. Li, *Energy Environ. Sci.*, 2019, **12**, 322–333.

110 Z. Pei, H. Li, Y. Huang, Q. Xue, Y. Huang, M. Zhu, Z. Wang and C. Zhi, *Energy Environ. Sci.*, 2017, **10**, 742–749.

111 Z. Xu, Z. Ma, K. Dong, J. Liang, L. Zhang, Y. Luo, Q. Liu, J. You, Z. Feng, D. Ma, Y. Wang and X. Sun, *Chem. Commun.*, 2022, **58**, 5025–5028.

112 N. Jia, Q. Weng, Y. Shi, X. Shi, X. Chen, P. Chen, Z. An and Y. Chen, *Nano Res.*, 2018, **11**, 1905–1916.

113 P. Zhang, K. Wang, P. Pei, Y. Zuo, M. Wei, X. Liu, Y. Xiao and J. Xiong, *Mater. Today Chem.*, 2021, **21**, 100538.

114 Z. Xu, H. Zhao, J. Liang, Y. Wang, T. Li, Y. Luo, X. Shi, S. Lu, Z. Feng, Q. Wu and X. Sun, *Mater. Today Phys.*, 2020, **15**, 100280.

115 C. Ding and Z. Qiao, *CrystEngComm*, 2022, **24**, 6289–6296.

116 G. Nie, Z. Zhang, T. Wang, C. Wang and Z. Kou, *ACS Appl. Mater. Interfaces*, 2021, **13**, 37961–37978.

117 L. Ma, S. Chen, D. Wang, Q. Yang, F. Mo, G. Liang, N. Li, H. Zhang, J. A. Zapien and C. Zhi, *Adv. Energy Mater.*, 2019, **9**, 1803046.

118 K. Lu, T. Jiang, H. Hu and M. Wu, *Front. Chem.*, 2020, **8**, 546728.

119 G. Ren, Q. Chen, J. Zheng, B. Huang and Y. Qian, *J. Electroanal. Chem.*, 2018, **829**, 177–183.

120 Z. Zhao, W. Yu, W. Shang, Y. He, Y. Ma, Z. Zhang and P. Tan, *Int. J. Energy Res.*, 2022, **46**, 7694–7703.

121 M. Chatenet, B. G. Pollet, D. R. Dekel, F. Dionigi, J. Deseure, P. Millet, R. D. Braatz, M. Z. Bazant, M. Eikerling, I. Staffell, P. Balcombe, Y. Shao-Horn and H. Schafer, *Chem. Soc. Rev.*, 2022, **51**, 4583–4762.

122 J. Zhao, Z. Tu and S. H. Chan, *J. Power Sources*, 2021, **488**, 229434.

123 S. Maass, F. Finsterwalder, G. Frank, R. Hartmann and C. Merten, *J. Power Sources*, 2008, **176**, 444–451.

124 S. Moller, S. Barwe, J. Masa, D. Wintrich, S. Seisel, H. Baltruschat and W. Schuhmann, *Angew. Chem., Int. Ed. Engl.*, 2020, **59**, 1585–1589.

125 S. G. Ji, H. Kim, W. H. Lee, H. Oh and C. H. Choi, *J. Mater. Chem. A*, 2021, **9**, 19834–19839.

126 H. Singh, S. Zhuang, B. Ingis, B. B. Nunna and E. S. Lee, *Carbon*, 2019, **151**, 160–174.

127 I. S. Filimonenkov, C. Bouillet, G. Kéranguéven, P. A. Simonov, G. A. Tsirlina and E. R. Savinova, *Electrochim. Acta*, 2019, 321.

128 T. Liu, X. J. Du, S. Li, Q. L. Wu, Q. Guo, Z. Z. Liu, J. P. Zhao and F. C. Liu, *Nanoscale*, 2022, **14**, 14248–14254.

129 Y. Gao, Z. Xiao, D. Kong, R. Iqbal, Q. Yang and L. Zhi, *Nano Energy*, 2019, **64**, 103879.

130 F. Gui, Q. Jin, D. Xiao, X. Xu, Q. Tan, D. Yang, B. Li, P. Ming, C. Zhang, Z. Chen, S. Siahrostami and Q. Xiao, *Small*, 2022, **18**, e2105928.

131 P. Jia, J. Zhang, G. Xia, Z. Yu, J. Sun and X. Ji, *Polymers*, 2022, **14**, 2581.

132 H. W. Liang, X. Zhuang, S. Bruller, X. Feng and K. Mullen, *Nat. Commun.*, 2014, **5**, 4973.

133 Q. Xie, W. Si, Y. Shen, Z. Wang and H. Uyama, *Nanoscale*, 2021, **13**, 16296–16306.

134 T. Lu, X. Hu, J. He, R. Li, J. Gao, Q. Lv, Z. Yang, S. Cui and C. Huang, *Nano Energy*, 2021, 85.

135 G. Yasin, S. Ibrahim, S. Ibraheem, S. Ali, R. Iqbal, A. Kumar, M. Tabish, Y. Slimani, T. A. Nguyen, H. Xu and W. Zhao, *J. Mater. Chem. A*, 2021, **9**, 18222–18230.

136 Y. Zhang, X. Fan, J. Jian, D. Yu, Z. Zhang and L. Dai, *Energy Environ. Sci.*, 2017, **10**, 2312–2317.

137 F. Liu and B. He, *Electrochim. Acta*, 2020, **362**, 137225.

138 Q. Yu, J. Wang, H. Li, R. Li, S. Zeng, R. Li, Q. Yao, H. Chen, K. Qu and Y. Zheng, *Chem. Eng. J.*, 2022, **429**, 132102.

139 X. Ding, F. Li, Q. Cao, H. Wu, Y. Qin, L. Yang, T. Wang, X. Zheng and C. Wang, *Chem. Eng. J.*, 2022, **429**, 132469.

140 B. J. Ferraz, B. Li, Z. Guo, C. Blackman and Z. Liu, *ChemElectroChem*, 2021, **8**, 3954–3961.

141 X. Wang, G. Li, Z. Lu, S. Cao, C. Hao, S. Wang and G. Sun, *Catal. Sci. Technol.*, 2022, **12**, 181–191.

142 J. Liu, P. Song and W. Xu, *Carbon*, 2017, **115**, 763–772.

143 X. Li, X. Duan, C. Han, X. Fan, Y. Li, F. Zhang, G. Zhang, W. Peng and S. Wang, *Carbon*, 2019, **148**, 540–549.

144 S. Cao, W. Shang, G. Li, Z. Lu, X. Wang, Y. Yan, C. Hao, S. Wang and G. Sun, *Carbon*, 2021, **184**, 127–135.

145 Z. Liu, M. Wang, X. Luo, S. Li, S. Li, Q. Zhou, W. Xu and R. Wu, *Appl. Surf. Sci.*, 2021, **544**, 148912.

146 T. Ma, J. Ran, S. Dai, M. Jaroniec and S. Z. Qiao, *Angew. Chem., Int. Ed. Engl.*, 2015, **54**, 4646–4650.

147 C. Tang, H. Wang, X. Chen, B. Q. Li, T. Z. Hou, B. S. Zhang, Q. Zhang, M. M. Titirici and F. Wei, *Adv. Mater.*, 2016, **28**, 6845.

148 L. Zhang, T. Gu, K. Lu, L. Zhou, D. S. Li and R. Wang, *Adv. Funct. Mater.*, 2021, **31**, 2103187.

149 J. C. Carrillo-Rodríguez, A. M. Garay-Tapia, B. Escobar-Morales, J. Escorcia-García, M. T. Ochoa-Lara, F. J. Rodríguez-Varela and I. L. Alonso-Lemus, *Int. J. Hydrogen Energy*, 2021, **46**, 26087–26100.

150 Y. Sato, N. Yamada, S. Kitano, D. Kowalski, Y. Aoki and H. Habazaki, *J. Mater. Chem. A*, 2022, **10**, 8208–8217.

151 C. Madan, L. Sharma, S. Mukerjee and A. Halder, *Int. J. Hydrogen Energy*, 2022, **47**, 22738–22751.

152 S. Möller, S. Barwe, S. Dieckhöfer, J. Masa, C. Andronescu and W. Schuhmann, *ChemElectroChem*, 2020, 7, 2680–2686.

153 Y. Sun, G. Chen, S. Xi and Z. J. Xu, *ACS Catal.*, 2021, **11**, 13947–13954.

154 J. O. Olowoyo and R. J. Kriek, *Small*, 2022, **18**, e2203125.

155 E. Yeager, *J. Mol. Catal.*, 1986, **38**, 5–25.

156 J. Suntivich, H. A. Gasteiger, N. Yabuuchi, H. Nakanishi, J. B. Goodenough and Y. Shao-Horn, *Nat. Chem.*, 2011, **3**, 546–550.

157 D. N. Mueller, M. L. Machala, H. Bluhm and W. C. Chueh, *Nat. Commun.*, 2015, **6**, 6097.

158 D. U. Lee, P. Xu, Z. P. Cano, A. G. Kashkooli, M. G. Park and Z. Chen, *J. Mater. Chem. A*, 2016, **4**, 7107–7134.

159 K. Zhang, X. Han, Z. Hu, X. Zhang, Z. Tao and J. Chen, *Chem. Soc. Rev.*, 2015, **44**, 699–728.

160 F. Cheng, T. Zhang, Y. Zhang, J. Du, X. Han and J. Chen, *Angew. Chem., Int. Ed. Engl.*, 2013, **52**, 2474–2477.

161 Z. Chen, A. Yu, R. Ahmed, H. Wang, H. Li and Z. Chen, *Electrochim. Acta*, 2012, **69**, 295–300.

162 K. Mette, A. Bergmann, J.-P. Tessonnier, M. Hävecker, L. Yao, T. Ressler, R. Schlögl, P. Strasser and M. Behrens, *ChemCatChem*, 2012, **4**, 851–862.

163 F. Cheng, Y. Su, J. Liang, Z. Tao and J. Chen, *Chem. Mater.*, 2009, **22**, 898–905.

164 J. Wu, J. Xue, F. Huang, N. Zhang, C. Tao and X. Fan, *J. Alloys Compd.*, 2022, **907**, 164520.

165 S. Ding, Z. Lyu, E. Sarnello, M. Xu, L. Fang, H. Tian, S. E. Karcher, T. Li, X. Pan, J. McCloy, G. Ding, Q. Zhang, Q. Shi, D. Du, J. Li, X. Zhang and Y. Lin, *J. Mater. Chem. A*, 2022, **10**, 5981–5989.

166 B. Chutia, N. Hussain, P. Puzari, D. Jampaiah, S. K. Bhargava, E. V. Matus, I. Z. Ismagilov, M. Kerzhentsev and P. Bharali, *Energy Fuels*, 2021, **35**, 10756–10769.

167 M. Sridharan and T. Maiyalagan, *J. Mater. Sci.: Mater. Electron.*, 2022, **33**, 9538–9548.

168 J. Shin, J. K. Seo, R. Yaylian, A. Huang and Y. S. Meng, *Int. Mater. Rev.*, 2019, **65**, 356–387.

169 N. Jia, T. Yang, S. Shi, X. Chen, Z. An, Y. Chen, S. Yin and P. Chen, *ACS Sustainable Chem. Eng.*, 2020, **8**, 2883–2891.

170 T. N. Lambert, D. J. Davis, W. Lu, S. J. Limmer, P. G. Kotula, A. Thuli, M. Hungate, G. Ruan, Z. Jin and J. M. Tour, *Chem. Commun.*, 2012, **48**, 7931–7933.

171 D. W. Wang, F. Li, L. C. Yin, X. Lu, Z. G. Chen, I. R. Gentle, G. Q. Lu and H. M. Cheng, *Chemistry*, 2012, **18**, 5345–5351.

172 X. Liu, X. Cui, K. Dastafkan, H. Wang, C. Tang, C. Zhao, A. Chen, C. He, M. Han and Q. Zhang, *J. Energy Chem.*, 2021, **53**, 290–302.

173 Y. Zhou, S. Xi, J. Wang, S. Sun, C. Wei, Z. Feng, Y. Du and Z. J. Xu, *ACS Catal.*, 2017, **8**, 673–677.

174 S. Sun, Y. Sun, Y. Zhou, S. Xi, X. Ren, B. Huang, H. Liao, L. P. Wang, Y. Du and Z. J. Xu, *Angew. Chem., Int. Ed. Engl.*, 2019, **58**, 6042–6047.

175 C. Wei, Z. Feng, G. G. Scherer, J. Barber, Y. Shao-Horn and Z. J. Xu, *Adv. Mater.*, 2017, **29**, 1606800.

176 Y. Zhou, S. Sun, S. Xi, Y. Duan, T. Sritharan, Y. Du and Z. J. Xu, *Adv. Mater.*, 2018, **30**, 1705407.

177 Y. Zhou, Y. Du, S. Xi and Z. J. Xu, *Electrocatalysis*, 2017, **9**, 287–292.

178 Y. Sun, X. Ren, S. Sun, Z. Liu, S. Xi and Z. J. Xu, *Angew. Chem., Int. Ed. Engl.*, 2021, **60**, 14536–14544.

179 Y. Chen, J. K. Seo, Y. Sun, T. A. Wynn, M. Olguin, M. Zhang, J. Wang, S. Xi, Y. Du, K. Yuan, W. Chen, A. C. Fisher, M. Wang, Z. Feng, J. Gracia, L. Huang, S. Du, H. J. Gao, Y. S. Meng and Z. J. Xu, *Nat. Commun.*, 2022, **13**, 5510.

180 Q. Zhao, Z. Yan, C. Chen and J. Chen, *Chem. Rev.*, 2017, **117**, 10121–10211.

181 J. Béjar, L. Álvarez-Contreras, J. Ledesma-García, N. Arjona and L. G. Arriaga, *J. Electroanal. Chem.*, 2019, **847**, 113190.

182 M. Prabu, K. Ketpang and S. Shanmugam, *Nanoscale*, 2014, **6**, 3173–3181.

183 V. Rajic, I. Stojkovic Simatovic, L. Veselinovic, J. B. Cavor, M. Novakovic, M. Popovic, S. D. Skapin, M. Mojovic, S. Stojadinovic, V. Rac, I. J. Castvan and S. Markovic, *Phys. Chem. Chem. Phys.*, 2020, **22**, 22078–22095.

184 J. Bao, Z. Wang, W. Liu, L. Xu, F. Lei, J. Xie, Y. Zhao, Y. Huang, M. Guan and H. Li, *J. Alloys Compd.*, 2018, **764**, 565–573.

185 M. Prabu, P. Ramakrishnan and S. Shanmugam, *Electrochem. Commun.*, 2014, **41**, 59–63.

186 G. Wu, J. Wang, W. Ding, Y. Nie, L. Li, X. Qi, S. Chen and Z. Wei, *Angew. Chem., Int. Ed. Engl.*, 2016, **55**, 1340–1344.

187 Y. Zhang, Z. Zhang, G. Jiang, A. H. Mamaghani, S. Sy, R. Gao, Y. Jiang, Y. Deng, Z. Bai, L. Yang, A. Yu and Z. Chen, *Nano Energy*, 2022, **100**.

188 S. Kosasang, H. Gatemala, N. Ma, P. Chomkhuntod and M. Sawangphruk, *Batteries Supercaps*, 2020, **3**, 631–637.

189 Z. Zhang, J. Li, J. Qian, Z. Li, L. Jia, D. Gao and D. Xue, *Small*, 2022, **18**, e2104248.

190 Z. Qian, Y. Chen, Z. Tang, Z. Liu, X. Wang, Y. Tian and W. Gao, *Nano-Micro Lett.*, 2019, **11**, 28.

191 Y. Zhu, X. Liu, S. Jin, H. Chen, W. Lee, M. Liu and Y. Chen, *J. Mater. Chem. A*, 2019, **7**, 5875–5897.

192 K. Min, S. Kim, E. Lee, G. Yoo, H. C. Ham, S. E. Shim, D. Lim and S.-H. Baeck, *J. Mater. Chem. A*, 2021, **9**, 17344–17352.

193 X. Zhou, X. Liao, X. Pan, M. Yan, L. He, P. Wu, Y. Zhao, W. Luo and L. Mai, *Nano Energy*, 2021, **83**.

194 K. Wang, Z. Wang, Y. Liu, J. Liu, Z. Cui, X. Zhang, F. Ciucci and Z. Tang, *Chem. Eng. J.*, 2022, **427**.

195 B. Mu, X. Zhang, Y. Zhang, P. Lu, J. Hao and J. Zhang, *RSC Adv.*, 2022, **12**, 9821–9827.

196 K. Xiang, Z. Xu, T. Qu, Z. Tian, Y. Zhang, Y. Wang, M. Xie, X. Guo, W. Ding and X. Guo, *Chem. Commun.*, 2017, **53**, 12410–12413.

197 J. Tang, C. Su and Z. Shao, *Energy Technol.*, 2022, **10**, 2200235.

198 Y. Tian, X. Liu, L. Xu, D. Yuan, Y. Dou, J. Qiu, H. Li, J. Ma, Y. Wang, D. Su and S. Zhang, *Adv. Funct. Mater.*, 2021, **31**, 2101239.

199 Z. Xiao, Y. C. Huang, C. L. Dong, C. Xie, Z. Liu, S. Du, W. Chen, D. Yan, L. Tao, Z. Shu, G. Zhang, H. Duan, Y. Wang, Y. Zou, R. Chen and S. Wang, *J. Am. Chem. Soc.*, 2020, **142**, 12087–12095.

200 Z. Xiao, Y. Wang, Y.-C. Huang, Z. Wei, C.-L. Dong, J. Ma, S. Shen, Y. Li and S. Wang, *Energy Environ. Sci.*, 2017, **10**, 2563–2569.

201 S. V. Devaguptapu, S. Hwang, S. Karakalos, S. Zhao, S. Gupta, D. Su, H. Xu and G. Wu, *ACS Appl. Mater. Interfaces*, 2017, **9**, 44567–44578.

202 H. Yu, H. Fan, B. Yadian, H. Tan, W. Liu, H. H. Hng, Y. Huang and Q. Yan, *ACS Appl. Mater. Interfaces*, 2015, **7**, 26751–26757.

203 S. L. Zhang, B. Y. Guan, X. F. Lu, S. Xi, Y. Du and X. W. D. Lou, *Adv. Mater.*, 2020, **32**, e2002235.

204 Y. Huang, S. L. Zhang, X. F. Lu, Z. P. Wu, D. Luan and X. W. D. Lou, *Angew. Chem., Int. Ed. Engl.*, 2021, **60**, 11841–11846.

205 X. Wang, Z. Liao, Y. Fu, C. Neumann, A. Turchanin, G. Nam, E. Zschech, J. Cho, J. Zhang and X. Feng, *Energy Stor. Mater.*, 2020, **26**, 157–164.

206 J. Lee, G. Nam, J. Sun, S. Higashi, H.-W. Lee, S. Lee, W. Chen, Y. Cui and J. Cho, *Adv. Energy Mater.*, 2016, **6**, 1601052.

207 R. E. Davis, G. L. Horvath and C. W. Tobias, *Electrochim. Acta*, 1967, **12**, 287–297.

208 Y. Matsumoto, H. Yoneyama and H. Tamura, *J. Electroanal. Chem. Interfacial Electrochem.*, 1977, **79**, 319–326.

209 B. Li, C. Tang, H. F. Wang, X. L. Zhu and Q. Zhang, *Sci. Adv.*, 2016, **2**, e1600495.

210 J. I. Jung, H. Y. Jeong, M. G. Kim, G. Nam, J. Park and J. Cho, *Adv. Mater.*, 2015, **27**, 266–271.

211 G. Ou, C. Yang, Y. Liang, N. Hussain, B. Ge, K. Huang, Y. Xu, H. Wei, R. Zhang and H. Wu, *Small Methods*, 2019, **3**, 1800279.

212 V. Kotha, I. Karajagi, P. C. Ghosh and L. S. Panchakarla, *ACS Appl. Energy Mater.*, 2022, **5**, 7297–7307.

213 B. Bao, Y. Liu, M. Sun, B. Huang, Y. Hu, P. Da, P. Ji, P. Xi and C. H. Yan, *Small*, 2022, **18**, e2201131.

214 B. He, Y. Deng, H. Wang, R. Wang, J. Jin, Y. Gong and L. Zhao, *J. Colloid Interface Sci.*, 2022, **625**, 502–511.

215 X. Wang, Z. Pan, X. Chu, K. Huang, Y. Cong, R. Cao, R. Sarangi, L. Li, G. Li and S. Feng, *Angew. Chem., Int. Ed. Engl.*, 2019, **58**, 11720–11725.

216 J. Ran, J.-F. Wu, Y. Hu, M. Shakouri, B. Xia and D. Gao, *J. Mater. Chem. A*, 2022, **10**, 1506–1513.

217 J. Ran, T. Wang, J. Zhang, Y. Liu, C. Xu, S. Xi and D. Gao, *Chem. Mater.*, 2020, **32**, 3439–3446.

218 S. Sun, X. Jin, B. Cong, X. Zhou, W. Hong and G. Chen, *J. Catal.*, 2019, **379**, 1–9.

219 J. Zhang, X. Bai, T. Wang, W. Xiao, P. Xi, J. Wang, D. Gao and J. Wang, *Nano-Micro Lett.*, 2019, **11**, 2.

220 X. Gong, H. Zhong, L. A. Estudillo-Wong, N. Alonso-Vante, Y. Feng and D. Li, *J. Energy Chem.*, 2022, **74**, 376–386.

221 C.-X. Zhao, B.-Q. Li, M. Zhao, J.-N. Liu, L.-D. Zhao, X. Chen and Q. Zhang, *Energy Environ. Sci.*, 2020, **13**, 1711–1716.

222 H. Wang, C. Tang, B. Wang, B. Q. Li and Q. Zhang, *Adv. Mater.*, 2017, **29**, 1702327.

223 B. Wang, C. Tang, H. F. Wang, B. Q. Li, X. Cui and Q. Zhang, *Small Methods*, 2018, **2**, 1800055.

224 J. Masa, P. Weide, D. Peeters, I. Sinev, W. Xia, Z. Sun, C. Somsen, M. Muhler and W. Schuhmann, *Adv. Energy Mater.*, 2016, **6**, 1502313.

225 Z. Shao, Q. Zhu, Y. Sun, Y. Zhang, Y. Jiang, S. Deng, W. Zhang, K. Huang and S. Feng, *Adv. Mater.*, 2022, **34**, e2110172.

226 Y. Wang, X. Wu, X. Jiang, X. Wu, Y. Tang, D. Sun and G. Fu, *Chem. Eng. J.*, 2022, 434.

227 B. Chen, R. Li, G. Ma, X. Gou, Y. Zhu and Y. Xia, *Nanoscale*, 2015, **7**, 20674–20684.

228 C. Hu, J. Liu, J. Wang, W. She, J. Xiao, J. Xi, Z. Bai and S. Wang, *ACS Appl. Mater. Interfaces*, 2018, **10**, 33124–33134.

229 H. Liu, J. Guan, S. Yang, Y. Yu, R. Shao, Z. Zhang, M. Dou, F. Wang and Q. Xu, *Adv. Mater.*, 2020, **32**, e2003649.

230 Z. Wang, K. Shen, L. Chen and Y. Li, *Sci. China: Chem.*, 2021, **65**, 619–629.

231 H. Wang, C. Li, J. An, Y. Zhuang and S. Tao, *J. Mater. Chem. A*, 2021, **9**, 18421–18430.

232 W. Jin, J. Chen, B. Liu, J. Hu, Z. Wu, W. Cai and G. Fu, *Small*, 2019, **15**, e1904210.

233 X. Li, H. Rong, J. Zhang, D. Wang and Y. Li, *Nano Res.*, 2020, **13**, 1842–1855.

234 Y. Wen, J. Qi, P. Wei, X. Kang and X. Li, *J. Mater. Chem. A*, 2021, **9**, 10260–10269.

235 X. Guo, S. Lin, J. Gu, S. Zhang, Z. Chen and S. Huang, *ACS Catal.*, 2019, **9**, 11042–11054.

236 K. Dong, J. Liang, Y. Ren, Y. Wang, Z. Xu, L. Yue, T. Li, Q. Liu, Y. Luo, Y. Liu, S. Gao, M. S. Hamdy, Q. Li, D. Ma and X. Sun, *J. Mater. Chem. A*, 2021, **9**, 26019–26027.

237 R. Jasinski, *Nature*, 1964, **201**, 1212–1213.

238 L. Lin, Q. Zhu and A. W. Xu, *J. Am. Chem. Soc.*, 2014, **136**, 11027–11033.

239 C. W. B. Bezerra, L. Zhang, K. Lee, H. Liu, A. L. B. Marques, E. P. Marques, H. Wang and J. Zhang, *Electrochim. Acta*, 2008, **53**, 4937–4951.

240 Y. Zhu, Z. Zhang, Z. Lei, Y. Tan, W. Wu, S. Mu and N. Cheng, *Carbon*, 2020, **167**, 188–195.

241 S. Chen, T. Luo, X. Li, K. Chen, J. Fu, K. Liu, C. Cai, Q. Wang, H. Li, Y. Chen, C. Ma, L. Zhu, Y. R. Lu, T. S. Chan, M. Zhu, E. Cortes and M. Liu, *J. Am. Chem. Soc.*, 2022, **144**, 14505–14516.

242 P. Li, H. Wang, X. Tan, W. Hu, M. Huang, J. Shi, J. Chen, S. Liu, Z. Shi and Z. Li, *Appl. Catal., B*, 2022, 316.

243 D. Lyu, Y. Du, S. Huang, B. Y. Mollamahale, X. Zhang, S. W. Hasan, F. Yu, S. Wang, Z. Q. Tian and P. K. Shen, *ACS Appl. Mater. Interfaces*, 2019, **11**, 39809–39819.

244 J. Zhang, T. Zhang, J. Ma, Z. Wang, J. Liu and X. Gong, *Carbon*, 2021, **172**, 556–568.

245 P. Yu, L. Wang, F. Sun, Y. Xie, X. Liu, J. Ma, X. Wang, C. Tian, J. Li and H. Fu, *Adv. Mater.*, 2019, **31**, e1901666.

246 K. Gao, M. Shen, C. Duan, C. Xiong, L. Dai, W. Zhao, W. Lu, S. Ding and Y. Ni, *ACS Sustainable Chem. Eng.*, 2021, **9**, 17068–17077.

247 Y. He, S. Hwang, D. A. Cullen, M. A. Uddin, L. Langhorst, B. Li, S. Karakalos, A. J. Kropf, E. C. Wegener, J. Sokolowski, M. Chen, D. Myers, D. Su, K. L. More, G. Wang, S. Litster and G. Wu, *Energy Environ. Sci.*, 2019, **12**, 250–260.

248 L. Xu, D. Deng, Y. Tian, H. Li, J. Qian, J. Wu and H. Li, *Chem. Eng. J.*, 2021, **408**, 127321.

249 J. Li, Z. Yang, D. Tang, L. Zhang, P.-X. Hou, S. Zhao, C. Liu, M. Cheng, G. Li, F. Zhang and H. Cheng, *NPG Asia Mater.*, 2018, **10**, e461.

250 Y. Wang, L. Wang and H. Fu, *Sci. China Mater.*, 2022, **65**, 1701–1722.

251 C. Shao, L. Wu, Y. Wang, K. Qu, H. Chu, L. Sun, J. Ye, B. Li and X. Wang, *Appl. Catal., B*, 2022, **316**, 121607.

252 R. Ma, J. Wang, Y. Tang and J. Wang, *J. Phys. Chem. Lett.*, 2022, **13**, 168–174.

253 Z. Mei, S. Cai, G. Zhao, Q. Jing, X. Sheng, J. Jiang and H. Guo, *Energy Stor. Mater.*, 2022, **50**, 12–20.

254 L. Yang, X. Zhang, L. Yu, J. Hou, Z. Zhou and R. Lv, *Adv. Mater.*, 2022, **34**, e2105410.

255 F. Liu, L. Shi, S. Song, K. Ge, X. Zhang, Y. Guo and D. Liu, *Small*, 2021, **17**, e2102425.

256 W. Zhai, S. Huang, C. Lu, X. Tang, L. Li, B. Huang, T. Hu, K. Yuan, X. Zhuang and Y. Chen, *Small*, 2022, 18.

257 C. Yang, S. Shang, Q. Gu, J. Shang and X.-y. Li, *J. Energy Chem.*, 2022, **66**, 306–313.

258 G. Yang, J. Zhu, P. Yuan, Y. Hu, G. Qu, B. A. Lu, X. Xue, H. Yin, W. Cheng, J. Cheng, W. Xu, J. Li, J. Hu, S. Mu and J. N. Zhang, *Nat. Commun.*, 2021, **12**, 1734.

259 Z. Wang, H. Jin, T. Meng, K. Liao, W. Meng, J. Yang, D. He, Y. Xiong and S. Mu, *Adv. Funct. Mater.*, 2018, **28**, 1802596.

260 Y. Mu, T. Wang, J. Zhang, C. Meng, Y. Zhang and Z. Kou, *Electrochem. Energy Rev.*, 2021, **5**, 145–186.

261 Z. Zhang, S. Yang, R. Jiang, T. Sheng, C. Shi, Y. Chen and L. Wang, *Nano Res.*, 2022, **15**, 8928–8935.

262 J. Liu, J. Xiao, B. Luo, E. Tian and G. I. N. Waterhouse, *Chem. Eng. J.*, 2022, **427**, 132038.

263 F. Lu, K. Fan, L. Cui, B. Li, Y. Yang, L. Zong and L. Wang, *Appl. Catal., B*, 2022, **313**, 121464.

264 D. Chen, Z. Chen, Z. Lu, X. Zhang, J. Tang and C. V. Singh, *Nanoscale*, 2020, **12**, 18721–18732.

265 Y. Guo, P. Yuan, J. Zhang, Y. Hu, I. S. Amiinu, X. Wang, J. Zhou, H. Xia, Z. Song, Q. Xu and S. Mu, *ACS Nano*, 2018, **12**, 1894–1901.

266 H. Xu, Y. Zhao, Q. Wang, G. He and H. Chen, *Coord. Chem. Rev.*, 2022, **451**, 214261.

267 J. Li, X. Qin, F. Xiao, C. Liang, M. Xu, Y. Meng, E. Sarnello, L. Fang, T. Li, S. Ding, Z. Lyu, S. Zhu, X. Pan, P. X. Hou, C. Liu, Y. Lin and M. Shao, *Nano Lett.*, 2021, **21**, 4508–4515.

268 J. Tang, Z. Zeng, H. Liang, Z. Wang, W. Nong, Z. Yang, C. Qi, Z. Qiao, Y. Li and C. Wang, *ACS Omega*, 2022, **7**, 19794–19803.

269 J. Li, S. Chen, N. Yang, M. Deng, S. Ibraheem, J. Deng, J. Li, L. Li and Z. Wei, *Angew. Chem., Int. Ed. Engl.*, 2019, **58**, 7035–7039.

270 G. W. Sievers, A. W. Jensen, J. Quinson, A. Zana, F. Bizzotto, M. Oezaslan, A. Dworzak, J. J. K. Kirkensgaard, T. E. L. Smitshuysen, S. Kadkhodazadeh, M. Juelsholt, K. M. O. Jensen, K. Anklam, H. Wan, J. Schafer, K. Cepe, M. Escudero-Escribano, J. Rossmeisl, A. Quade, V. Bruser and M. Arenz, *Nat. Mater.*, 2021, **20**, 208–213.

271 J. Chen, H. Li, C. Fan, Q. Meng, Y. Tang, X. Qiu, G. Fu and T. Ma, *Adv. Mater.*, 2020, **32**, e2003134.

272 F. Zheng, Y. Ji, H. Dong, C. Liu, S. Chen and Y. Li, *J. Phys. Chem. C*, 2021, **126**, 30–39.

273 H. Liu, X. H. Zhang, Y. X. Li, X. Li, C. K. Dong, D. Y. Wu, C. C. Tang, S. L. Chou, F. Fang and X. W. Du, *Adv. Energy Mater.*, 2020, **10**, 1902521.

274 X. Xie, Y. Xue, L. Li, S. Chen, Y. Nie, W. Ding and Z. Wei, *Nanoscale*, 2014, **6**, 11035–11040.

275 X. Han, N. Li, P. Xiong, M. G. Jung, Y. Kang, Q. Dou, Q. Liu, J. Y. Lee and H. S. Park, *InfoMat*, 2021, **3**, 1134–1144.

276 S. G. Chandrappa, P. Moni, G. Karkera and A. S. Prakash, *Nanoscale Adv.*, 2019, **1**, 2392–2399.

277 Z. Pu, Q. Liu, C. Tang, A. M. Asiri, A. H. Qusti, A. O. Al-Youbi and X. Sun, *J. Power Sources*, 2014, **257**, 170–173.

278 H. Cheng, M.-L. Li, C.-Y. Su, N. Li and Z.-Q. Liu, *Adv. Funct. Mater.*, 2017, **27**, 1701833.

279 P. K. Gangadharan, S. N. Bhange, N. Kabeer, R. Illathvalappil and S. Kurungot, *Nanoscale Adv.*, 2019, **1**, 3243–3251.

280 M. Wu, G. Zhang, J. Qiao, N. Chen, W. Chen and S. Sun, *Nano Energy*, 2019, **61**, 86–95.

281 A. Zhao, J. Masa, W. Xia, A. Maljusch, M. G. Willinger, G. Clavel, K. Xie, R. Schlogl, W. Schuhmann and M. Muhler, *J. Am. Chem. Soc.*, 2014, **136**, 7551–7554.

282 Z. Sun, Y. Wang, L. Zhang, H. Wu, Y. Jin, Y. Li, Y. Shi, T. Zhu, H. Mao, J. Liu, C. Xiao and S. Ding, *Adv. Funct. Mater.*, 2020, 30.

283 P. Ganesan, M. Prabu, J. Sanetuntikul and S. Shanmugam, *ACS Catal.*, 2015, **5**, 3625–3637.

284 G. Fu, J. Wang, Y. Chen, Y. Liu, Y. Tang, J. B. Goodenough and J.-M. Lee, *Adv. Energy Mater.*, 2018, **8**.

285 G. Nam, Y. Son, S. O. Park, W. C. Jeon, H. Jang, J. Park, S. Chae, Y. Yoo, J. Ryu, M. G. Kim, S. K. Kwak and J. Cho, *Adv. Mater.*, 2018, **30**, e1803372.

286 V. Jose, H. Hu, E. Edison, W. Manalastas Jr, H. Ren, P. Kidkhunthod, S. Sreejith, A. Jayakumar, J. M. V. Nsanzimana, M. Srinivasan, J. Choi and J.-M. Lee, *Small Methods*, 2021, **5**, 2000751.

287 Z. Lei, Y. Tan, Z. Zhang, W. Wu, N. Cheng, R. Chen, S. Mu and X. Sun, *Nano Res.*, 2020, **14**, 868–878.

288 Y. Guo, P. Yuan, J. Zhang, H. Xia, F. Cheng, M. Zhou, J. Li, Y. Qiao, S. Mu and Q. Xu, *Adv. Funct. Mater.*, 2018, **28**, 1805641.

289 Q. Shi, Q. Liu, Y. Zheng, Y. Dong, L. Wang, H. Liu and W. Yang, *Energy Environ. Mater.*, 2021, **5**, 515–523.

290 Y. Han, H. Duan, C. Zhou, H. Meng, Q. Jiang, B. Wang, W. Yan and R. Zhang, *Nano Lett.*, 2022, **22**, 2497–2505.

291 X. Guo, X. Hu, D. Wu, C. Jing, W. Liu, Z. Ren, Q. Zhao, X. Jiang, C. Xu, Y. Zhang and N. Hu, *ACS Appl. Mater. Interfaces*, 2019, **11**, 21506–21514.

292 B. Geboes, J. Ustarroz, K. Sentosun, H. Vanrompay, A. Hubin, S. Bals and T. Breugelmans, *ACS Catal.*, 2016, **6**, 5856–5864.

293 Y. Chung, D. Y. Chung, N. Jung, H. Y. Park, S. J. Yoo, J. H. Jang and Y.-E. Sung, *J. Phys. Chem. C*, 2014, **118**, 9939–9945.

294 Z. Kou, X. Li, L. Zhang, W. Zang, X. Gao and J. Wang, *Small Sci.*, 2021, **1**, 2100011.

295 X. Zhao, Q. Han, J. Li, X. Du, G. Liu, Y. Wang, L. Wu and Z. Chen, *Chem. Eng. J.*, 2022, **433**, 133509.

296 W. J. Sim, M. T. Nguyen, Z. Huang, S. Kheawhom, C. Wattanakit and T. Yonezawa, *Nanoscale*, 2022, **14**, 8012–8022.

297 Z. Chen, L. Cai, X. Yang, C. Kronawitter, L. Guo, S. Shen and B. E. Koel, *ACS Catal.*, 2018, **8**, 1238–1247.

298 B. Tian, H. Shin, S. Liu, M. Fei, Z. Mu, C. Liu, Y. Pan, Y. Sun, W. A. Goddard 3rd and M. Ding, *Angew. Chem., Int. Ed. Engl.*, 2021, **60**, 16448–16456.

299 Y. Sun, J. Wu, Y. Xie, X. Wang, K. Ma, Z. Tian, Z. Zhang, Q. Liao, W. Zheng, Z. Kang and Y. Zhang, *Adv. Funct. Mater.*, 2022, **32**, 2207116.

300 X. Xie, L. Du, L. Yan, S. Park, Y. Qiu, J. Sokolowski, W. Wang and Y. Shao, *Adv. Funct. Mater.*, 2022, **32**, 2110036.

301 G. Xing, M. Tong, P. Yu, L. Wang, G. Zhang, C. Tian and H. Fu, *Angew. Chem., Int. Ed. Engl.*, 2022, **61**, e202211098.

302 H. Zhang, P. Li, S. Chen, F. Xie and D. J. Riley, *Adv. Funct. Mater.*, 2021, **31**, 2106835.

303 Y. P. Deng, Y. Jiang, R. Liang, S. J. Zhang, D. Luo, Y. Hu, X. Wang, J. T. Li, A. Yu and Z. Chen, *Nat. Commun.*, 2020, **11**, 1952.

304 H. Hu, J. Wang, P. Tao, C. Song, W. Shang, T. Deng and J. Wu, *J. Mater. Chem. A*, 2022, **10**, 5835–5849.

305 Z. Hu, L. Hao, F. Quan and R. Guo, *Catal. Sci. Technol.*, 2022, **12**, 436–461.

306 R. N. Durr, P. Maltoni, H. Tian, B. Jousselme, L. Hammarstrom and T. Edvinsson, *ACS Nano*, 2021, **15**, 13504–13515.

307 J.-T. Ren, Y.-D. Ying, Y.-P. Liu, W. Li and Z.-Y. Yuan, *J. Energy Chem.*, 2022, **71**, 619–630.

308 M. Wu, G. Zhang, N. Chen, Y. Hu, T. Regier, D. Rawach and S. Sun, *ACS Energy Lett.*, 2021, **6**, 1153–1161.

309 L. An, Y. Hu, J. Y. Li, J. M. Zhu, M. Z. Sun, B. L. Huang, P. X. Xi and C. H. Yan, *Adv. Mater.*, 2022, **34**, e2202874.

310 B. Yan, D. Krishnamurthy, C. H. Hendon, S. Deshpande, Y. Surendranath and V. Viswanathan, *Joule*, 2017, **1**, 600–612.

311 F. T. Haase, A. Bergmann, T. E. Jones, J. Timoshenko, A. Herzog, H. S. Jeon, C. Rettenmaier and B. R. Cuenya, *Nat. Energy*, 2022, **7**, 765–773.

312 H. Wang, S. Hung, H. Chen, T. Chan, H. Chen and B. Liu, *J. Am. Chem. Soc.*, 2016, **138**, 36–39.

313 L. An, Y. Hu, J. Li, J. Zhu, M. Sun, B. Huang, P. Xi and C. H. Yan, *Adv. Mater.*, 2022, **34**, e2202874.

314 C. Weng, X. Lv, J. Ren, Y. Wang, W. Tian, L. Gao, H. Wang and Z. Yuan, *ACS Sustainable Chem. Eng.*, 2022, **10**, 6456–6465.

315 A. Saad, Y. Gao, A. Ramiere, T. Chu, G. Yasin, Y. Wu, S. Ibraheem, M. Wang, H. Guo, P. Tsiakaras and X. Cai, *Small*, 2022, **18**, e2201067.

316 X. Wang, X. Yang, H. Liu, T. Han, J. Hu, H. Li and G. Wu, *Small Struct.*, 2021, **3**, 2100103.

317 M. Fan, L. Cui, X. He and X. Zou, *Small Methods*, 2022, **6**, e2200855.

318 C. Liu, Q. Li, W. Kang, W. Lei, X. Wang, C. Lu and M. Naebe, *J. Mater. Chem. A*, 2022, **10**, 10–49.

319 Y. Zhong, X. Xu, W. Wang and Z. Shao, *Batteries Supercaps*, 2018, **2**, 272–289.

320 J. Li, Y. Zhu, W. Chen, Z. Lu, J. Xu, A. Pei, Y. Peng, X. Zheng, Z. Zhang, S. Chu and Y. Cui, *Joule*, 2019, **3**, 557–569.

321 P. Wang, T. Jia and B. Wang, *J. Electrochem. Soc.*, 2020, 167.

322 C. X. Zhao, J. N. Liu, J. Wang, D. Ren, J. Yu, X. Chen, B. Q. Li and Q. Zhang, *Adv. Mater.*, 2021, **33**, e2008606.

323 Y. Yuan, M. Li, Z. Bai, G. Jiang, B. Liu, T. Wu, Z. Chen, K. Amine and J. Lu, *Adv. Mater.*, 2019, **31**, e1805609.

324 S. S. Sekhon, J. Lee and J.-S. Park, *J. Energy Chem.*, 2022, **65**, 149–172.

325 A. Hayat, M. Sohail, J. Ali Shah Syed, A. G. Al-Sehemi, M. H. Mohammed, A. A. Al-Ghamdi, T. A. Taha, H. Salem AlSalem, A. M. Alenad, M. A. Amin, A. Palamanit, C. Liu, W. I. Nawawi, M. Tariq Saeed Chani and M. Muzibur Rahman, *Chem. Rec.*, 2022, **22**, e202100310.

326 Z. Pei, L. Ding, C. Wang, Q. Meng, Z. Yuan, Z. Zhou, S. Zhao and Y. Chen, *Energy Environ. Sci.*, 2021, **14**, 4926–4935.

327 C. Zhao, J. Liu, N. Yao, J. Wang, D. Ren, X. Chen, B. Q. Li and Q. Zhang, *Angew. Chem., Int. Ed. Engl.*, 2021, **60**, 15281–15285.

328 X. Lu, Y. Fang, D. Luan and X. W. D. Lou, *Nano Lett.*, 2021, **21**, 1555–1565.

329 G. Zhou, G. Liu, X. Liu, Q. Yu, H. Mao, Z. Xiao and L. Wang, *Adv. Funct. Mater.*, 2021, **32**, 2107608.

330 L. Zhong, Q. Huang, J. Ding, Y. Guo, X. Wang, L. Chai, T.-T. Li, Y. Hu, J. Qian and S. Huang, *J. Power Sources*, 2021, **492**, 229632.

331 N. Manna, S. K. Singh, M. Kurian, A. Torris and S. Kurungot, *ACS Appl. Energy Mater.*, 2022, **5**, 8756–8768.

332 X. Liu, Q. Yin, C. Dai, G. Li, J. Lian, Y. Zhao, S. Yang and H. Li, *ACS Sustainable Chem. Eng.*, 2021, **9**, 5345–5355.

333 D. Wang, B. Li, X. Tao, S. Rao, J. Li, W. Wang, J. Yang and Y. Zhou, *J. Electroanal. Chem.*, 2021, **898**, 115627.

334 S. Das, S. Bhattacharjee, S. Mondal, S. Dutta, N. Bothra, S. K. Pati and S. Bhattacharyya, *ACS Sustainable Chem. Eng.*, 2021, **9**, 14868–14880.

335 H. Sun, M. Wang, S. Zhang, S. Liu, X. Shen, T. Qian, X. Niu, J. Xiong and C. Yan, *Adv. Funct. Mater.*, 2020, 31.

336 Y. Niu, X. Teng, S. Gong, X. Liu, M. Xu and Z. Chen, *Energy Stor. Mater.*, 2021, **43**, 42–52.

337 Y. Dai, J. Yu, J. Wang, Z. Shao, D. Guan, Y. C. Huang and M. Ni, *Adv. Funct. Mater.*, 2022, **32**, 2111989.

338 B. Wang, P. Zhao, J. Feng, D. Chen, Y. Huang, L. Sui, H. Dong, S. Ma, L. Dong and L. Yu, *J. Colloid Interface Sci.*, 2021, **588**, 184–195.

339 Q. Lu, X. Zou, Y. Bu, K. Liao, W. Zhou and Z. Shao, *Small*, 2022, **18**, e2105604.

340 J. Zhang, J. Chen, Y. Luo, Y. Chen, Y. Luo, C. Zhang, Y. Xue, H. Liu, G. Wang and R. Wang, *J. Mater. Chem. A*, 2021, **9**, 5556–5565.

341 H. Pan, X. Huang, Z. Lu, Z. Zhang, B. An, D. Wu, T. Wang, X. Chen and F. Cheng, *Chem. Eng. J.*, 2021, 419.

342 N. Yu, H. Chen, J. Kuang, K. Bao, W. Yan, J. Ye, Z. Yang, Q. Huang, Y. Wu and S. Sun, *Nano Res.*, 2022, **15**, 7209–7219.

343 X. Liu, S. Peng, X. Li, C. Liu, J. Zeng, X. Qi and T. Liang, *J. Electrochem. Soc.*, 2021, **168**, 090514.

344 F. Zhang, L. Chen, Y. Zhang, Y. Peng, X. Luo, Y. Xu and Y. Shi, *Chem. Eng. J.*, 2022, **447**, 137490.

345 C. Shao, S. Zhuang, H. Zhang, Q. Jiang, X. Xu, J. Ye, B. Li and X. Wang, *Small*, 2021, **17**, e2006178.

346 L. Xie, X. P. Zhang, B. Zhao, P. Li, J. Qi, X. Guo, B. Wang, H. Lei, W. Zhang, U. P. Apfel and R. Cao, *Angew. Chem., Int. Ed. Engl.*, 2021, **60**, 7576–7581.
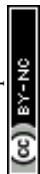
347 Y. Zhang, W. Xiao, Y. Yin, D. Z. Peng, H. Wang, M. Zhou, Z. Hou, Y. Liu and B. He, *New J. Chem.*, 2022, **46**, 17032–17039.

348 L. Song, H. Fan, T. Wang, T. Xiang, M. Zhang, C. Hu, W. Zhou and J. He, *Energy Stor. Mater.*, 2021, **43**, 365–374.

349 S. Chang, H. Zhang and Z. Zhang, *J. Energy Chem.*, 2021, **56**, 64–71.

350 N. Li, L. Liu, K. Wang, J. Niu, Z. Zhang, M. Dou and F. Wang, *Chemistry*, 2021, **27**, 10987–10997.

351 Z. Meng, G. Zhu, J. Wu, R. Wang, T. Tian, H. Tang, R. Luo, D. Ye, R. Zhang, F. Kwofie, Y. Cheng and H. Tang, *Mater. Today Energy*, 2022, **24**, 100935.

352 H. Xu, D. Wang, P. Yang, L. Du, X. Lu, R. Li, L. Liu, J. Zhang and M. An, *Appl. Catal., B*, 2022, **305**, 121040.

353 R. Zhao, H. Wang, X. Zhang, J. Liu, G. Du and T. Chen, *Langmuir*, 2022, **38**, 11372–11381.

354 M. Wang, L. Cao, X. Du, Y. Zhang, F. Jin, M. Zhang, Z. Li and K. Su, *ACS Appl. Mater. Interfaces*, 2022, **14**, 25427–25438.

355 K. Li, R. Cheng, Q. Xue, P. Meng, T. Zhao, M. Jiang, M. Guo, H. Li and C. Fu, *Chem. Eng. J.*, 2022, **450**, 137991.

356 X. Wang, R. K. M. Raghupathy, C. J. Querebillo, Z. Liao, D. Li, K. Lin, M. Hantusch, Z. Sofer, B. Li, E. Zschech, I. M. Weidinger, T. D. Kuhne, H. Mirhosseini, M. Yu and X. Feng, *Adv. Mater.*, 2021, **33**, e2008752.

357 C. Chen, H. Su, L.-N. Lu, Y.-S. Hong, Y. Chen, K. Xiao, T. Ouyang, Y. Qin and Z.-Q. Liu, *Chem. Eng. J.*, 2021, **408**, 127814.

358 X. Qiao, Y. Deng, X. Cao, J. Wu, H. Guo, W. Xiao and S. Liao, *Catalysts*, 2022, **12**, 1023.

359 C. Jin, H. Deng, J. Zhang, Y. Hao and J. Liu, *Chem. Eng. J.*, 2022, **434**, 134617.

360 X. Chen, J. Pu, X. Hu, Y. Yao, Y. Dou, J. Jiang and W. Zhang, *Small*, 2022, **18**, e2200578.

361 Y. Wang, N. Xu, R. He, L. Peng, D. Cai and J. Qiao, *Appl. Catal., B*, 2021, **285**, 119811.

362 Y. Jiang, Y. P. Deng, R. Liang, N. Chen, G. King, A. Yu and Z. Chen, *J. Am. Chem. Soc.*, 2022, **144**, 4783–4791.

363 H. Lei, Q. Zhang, Z. Liang, H. Guo, Y. Wang, H. Lv, X. Li, W. Zhang, U. P. Apfel and R. Cao, *Angew. Chem., Int. Ed. Engl.*, 2022, **61**, e202201104.

364 Z. Liang, H. Guo, G. Zhou, K. Guo, B. Wang, H. Lei, W. Zhang, H. Zheng, U. P. Apfel and R. Cao, *Angew. Chem., Int. Ed. Engl.*, 2021, **60**, 8472–8476.

365 S. Liang, Z.-D. Wang, Z.-F. Guo, X.-Y. Chen, S.-Q. Li, B.-D. Wang, G.-L. Lu, H. Sun, Z.-N. Liu and H.-Y. Zang, *New J. Chem.*, 2021, **45**, 3947–3953.

366 Y. Liao, H. Chen, C. Ou, L. Bao, R. Li and H. Liu, *J. Electroanal. Chem.*, 2022, **921**, 116560.

367 Y. Peng, F. Zhang, Y. Zhang, X. Luo, L. Chen and Y. Shi, *Dalton Trans.*, 2022, **51**, 12630–12640.

368 J. Yin, J. Jin, H. Liu, B. Huang, M. Lu, J. Li, H. Liu, H. Zhang, Y. Peng, P. Xi and C. H. Yan, *Adv. Mater.*, 2020, **32**, e2001651.

369 T. Hu, Z. Jiang, Z. Fu and Z.-J. Jiang, *J. Mater. Chem. A*, 2022, **10**, 8739–8750.

370 H. Zheng, Y. Zhang, J. Long, R. Li and X. Gou, *J. Electrochem. Soc.*, 2020, **167**, 084516.

371 X. Yang, X. Zheng, H. Li, B. Luo, Y. He, Y. Yao, H. Zhou, Z. Yan, Y. Kuang and Z. Huang, *Adv. Funct. Mater.*, 2022, **32**, 202200397.

372 Z. Zhang, H. Zhang, Y. Hou, P. Liu, X. Hao, Y. Liu, B. Xu and J. Guo, *J. Mater. Chem. A*, 2022, **10**, 13013–13020.

373 C. Li, Y. Wu, M. Fu, X. Zhao, S. Zhai, Y. Yan, L. Zhang and X. Zhang, *ACS Appl. Energy Mater.*, 2022, **5**, 4340–4350.

374 W. Zhai, S. Huang, C. Lu, X. Tang, L. Li, B. Huang, T. Hu, K. Yuan, X. Zhuang and Y. Chen, *Small*, 2022, **18**, e2107225.

375 C. Lai, X. Liu, C. Cao, Y. Wang, Y. Yin, T. Liang and D. D. Dionysiou, *Carbon*, 2021, **173**, 715–723.

376 C. Zhou, X. Chen, S. Liu, Y. Han, H. Meng, Q. Jiang, S. Zhao, F. Wei, J. Sun, T. Tan and R. Zhang, *J. Am. Chem. Soc.*, 2022, **144**, 2694–2704.

377 M. Christy, H. Rajan, H. Lee, I. Rabani, S. M. Koo and S. C. Yi, *ACS Appl. Energy Mater.*, 2021, **4**, 1876–1886.

378 Y. Zhao, X. Wang, X. Guo, D. Cheng, H. Zhou, N. Saito and T. Fan, *Carbon*, 2021, **184**, 609–617.

379 Y. Gao, D. Kong, F. Cao, S. Teng, T. Liang, B. Luo, B. Wang, Q.-H. Yang and L. Zhi, *Nano Res.*, 2022, **15**, 7959–7967.

380 Y. Ma, W. Shang, W. Yu, X. Chen, W. Xia, C. Wang and P. Tan, *Energy Fuels*, 2021, **35**, 14188–14196.

381 H. Begum, M. S. Ahmed and S. Jung, *J. Mater. Chem. A*, 2021, **9**, 9644–9654.

382 J. Ding, D. Wu, S. Huang, C. Lu, Y. Chen, J. Zhang, L. Zhang, J. Li, C. Ke, D. Tranca, E. Kymakis and X. Zhuang, *Nanoscale*, 2021, **13**, 13249–13255.

383 A. Wang, C. Zhao, M. Yu and W. Wang, *Appl. Catal., B*, 2021, **281**, 119514.

384 C. Shao, L. Wu, H. Zhang, Q. Jiang, X. Xu, Y. Wang, S. Zhuang, H. Chu, L. Sun, J. Ye, B. Li and X. Wang, *Adv. Funct. Mater.*, 2021, **31**, 2100833.

385 W. Zhang, X. Zhao, W. Niu, H. Yu, T. Wan, G. Liu, D. Zhang and Y. Wang, *Nanotechnology*, 2021, **33**, 065409.